

DESIGN OF A NOVEL ELECTROSTATIC MICRO ENERGY HARVESTER

by

MADHUMITA AMBOKAR

Presented to the Faculty of the Graduate School of  
The University of Texas at Arlington in Partial Fulfillment  
of the Requirements  
for the Degree of

MASTER OF SCIENCE IN ELECTRICAL ENGINEERING

THE UNIVERSITY OF TEXAS AT ARLINGTON

May 2011

Copyright © by Madhumita Ambekar 2011

All rights reserved

## ACKNOWLEDGEMENTS

I would like to take this opportunity to thank my advisor Professor Zeynep Celik-Butler for all her guidance. With her inspiration, enthusiasm and efforts to explain things, she made my research an interesting experience. She has helped me develop a systematic approach towards every situation. I would be grateful to her for all her support.

I want to thank Dr. Donald Butler and Dr. Dan Popa for gracing my thesis committee with their valued presence. I would like to convey special thanks to my professor Dr. Donald Butler for all his timely guidance and encouragement. His prompt suggestions helped me find the solutions for the problems I faced in my course of research.

I am thankful to all my friends in Nanofab, especially Erkin, Rohit, Gaviraj, Bhargav, Iqbal and Moinuddin for providing a fun environment along with their fruitful suggestions in my work. I am especially grateful to Erkin for allowing me to work on the accelerometers he designed.

I would not have enough words to express my gratitude towards my parents, my father Surendra Ambokar and my mother Suchita Ambokar. They are my source of motivation for what I have been able to achieve. I owe my life to them.

A 'thank you' would not be enough to express my gratefulness and love towards my grandfather, my Papaji, who has taught me the most important and wonderful lessons of my life.

Thank you all for all your support.

April 13, 2011

## ABSTRACT

### DESIGN OF A NOVEL ELECTROSTATIC MICRO ENERGY HARVESTER

Madhumita Ambokar, M.S

The University of Texas at Arlington, 2011

Supervising Professor: Dr. Zeynep Celik-Butler

The batteries have been a major source of energy for the electronic devices. However, the exhaustible nature of the batteries has encouraged the researchers to exploit the renewable energy sources for powering the electronics. Over the years, the researchers have tried to tap the stray energy provided by the ambient sources such as sun, wind, RF energy, vibration energy, etc. In the work presented here, an effort has been made to design a micro energy harvester, which would harness electric energy from the vibrations provided by the machine such as aircrafts, cars, engines, etc.

A variable capacitive device was designed such that the capacitance of the device changes with the change in the overlap area between the electrodes. The electrodes of the device were modified such that one of the electrodes was designed as a hollow cubic structure while the other electrode was inserted in it in the form of a stationary cantilever beam. A train of such modules was designed to obtain high capacitance values. Three device models were proposed where the number and the dimensions of cantilever beams were varied along with the dimensions of the cubic electrodes.

The devices were designed for the source acceleration of the range of 1.3 – 1.5g and the source frequency of 100 Hz. The displacement and the capacitance of the devices were determined by performing Finite Element Analysis (FEA) using the CoventorWare™ software. The capacitance values obtained from the simulations were then used to estimate the electrostatic energy that would be generated from the devices. The electrostatic energy was estimated for both charge-constrained and voltage-constrained conversion cycles. In the case of charge-constrained conversion cycle, the input voltage for the devices was assumed to be 10 V. On the other hand, in case of the voltage-constrained conversion cycle, a continuous input voltage of the 100 V was assumed to be supplied by an electrets material. The power generated was estimated by multiplying the energy with the frequency of vibrations (100 Hz). The device model number three named Model3\_200CL203, was observed to be the best in terms of the amount of energy that would be generated. A volumetric power maximum of 1810  $\mu\text{W}/\text{cm}^3$  was estimated for a voltage-constrained conversion cycle, while the volumetric power of 21.64  $\mu\text{W}/\text{cm}^3$  was estimated for the charge-constrained conversion cycle.

A fabrication process flow was also proposed. The metal electrodes were proposed to be fabricated using the electroplating process. A eutectic bonding process was proposed for realizing the hollow cubic structure. However, a few fabrication issues, such as realization of high aspect ratios and unreliable bonding of narrow bonding sites of the width of 5  $\mu\text{m}$ , were predicted. Hence, a few design modifications were suggested for all the devices so that the fabrication of the devices can be made less challenging. The effects of design modifications, on the displacement and capacitance of the devices, were also studied by simulating the modified devices in CoventorWare™

## TABLE OF CONTENTS

ACKNOWLEDEgements .....	iii
ABSTRACT.....	iv
LIST OF ILLUSTRATIONS.....	ix
LIST OF TABLES .....	xiv
LIST OF SYMBOLS.....	xvi
Chapter	Page
1. INTRODUCTION.....	1
1.1. Need of MEMS power harvesting devices.....	1
1.2. Various regenerative resources of power .....	2
1.2.1. Electromagnetic micro generators.....	9
1.2.2. Piezoelectric micro generators .....	11
1.2.3. Electrostatic micro generators .....	14
1.3. Challenges in designing of micro generators.....	15
1.4. Summary.....	17
2. CONVERSION MECHANISM AND DESIGN TOPOLOGIES FOR ELECTROSTATIC MICROGENERATORS.....	18
2.1. Introduction .....	18
2.2. Charge-constrained conversion cycle.....	19
2.3. Voltage-constrained conversion cycle .....	22
2.4. Design topologies for electrostatic energy harvesters.....	24
2.4.1. Out-of-plane gap closing converter .....	25

2.4.2. In-plane gap closing converter .....	26
2.4.3. In-plane overlap converter .....	27
2.5. Summary .....	28
3. DESIGN OF NOVEL ELECTROSTATIC MEMS ENERGY HARVESTER .....	29
3.1. Introduction .....	29
3.2. Accelerometer devices (designed and fabricated in NanoFab, UT Arlington) as energy harvesters .....	29
3.2.1. X-Y sensing accelerometers .....	30
3.2.2. Z-sensing accelerometers .....	32
3.3. Design of novel energy harvesters .....	35
3.3.1. Concept of 3D capacitive device .....	35
3.3.2. Design parameters for given operating conditions .....	37
3.3.2.1. Device Dimensions .....	37
3.3.2.2. Spring Design .....	39
3.3.3. Energy harvester device models .....	44
3.3.3.1. Model1_500CL35 .....	44
3.3.3.2. Model2_24CL287 .....	45
3.3.3.3. Model3_200CL203 .....	46
3.3.4. Fabrication challenges .....	49
3.3.5. Modifications to device models as per fabrication constraints .....	50
3.3.6. Proposed process flow .....	53
3.4. Summary .....	61
4. SIMULATION RESULTS AND DISCUSSION .....	62
4.1. Introduction .....	62
4.2. Mechanical analysis .....	62
4.2.1. Accelerometer device simulations .....	63
4.2.1.1. Material properties .....	63

4.2.1.2. Boundary conditions .....	63
4.2.1.3. Meshing .....	64
4.2.1.4. Displacement analysis .....	65
4.2.1.5. Capacitance analysis .....	66
4.2.2. Energy harvesters .....	69
4.2.1.1. Material properties .....	69
4.2.1.2. SpringMM.....	69
4.2.1.3. Boundary conditions for device simulations.....	70
4.2.1.4. Meshing.....	71
4.2.1.5. Displacement analysis .....	72
4.2.1.6. Capacitance analysis .....	76
4.2.1.7. Modal analysis .....	78
4.3. Energy and power estimates .....	79
4.3.1. Calculations for the electrostatic energy .....	79
4.3.1.1. Charge constrained conversion cycle.....	80
4.3.1.2. Voltage constrained conversion cycle .....	81
4.3.2. Calculations for the estimated power output.....	82
4.3.3. Comparisons .....	83
4.4. Summary .....	86
5. CONCLUSION.....	83
APPENDIX	
A. ENERGY HARVESTER DESIGNS AND SIMULATIONS.....	89
REFERENCES .....	100
BIOGRAPHICAL INFORMATION .....	107



## LIST OF ILLUSTRATIONS

1.1.	Relative improvements in laptop computing technology from 1990-2003. (Reprinted with permission) .....	2
1.2.	Diagram of a thermocouple used for thermoelectric generation. (Reprinted with permission).....	4
1.3.	Micro-graph of through-plane thermoelectric module. (Reprinted with permission).....	5
1.4.	Diagram of in-plane thermoelectric module. (Reprinted with permission).....	5
1.5.	Array of spiral antennas which include broad band elements with orthogonal circular polarization. (Reprinted with permission).....	7
1.6.	Spring-mass system with electrostatic and fluid damping forces. (Reproduced with permission). .....	8
1.7.	Electromagnetic microgenerators (a)Diagram of cantilever-based micro generator [1] and (b) Micromachined version of four-magnet design [2]. (Reprinted with permission).....	11
1.8.	Flow chart for piezoelectric activity.....	11
1.9.	The two modes of piezoelectric conversion from mechanical stress (a)31-mode, (b)33-mode [3] (c)Schematic representation of 31 mode and (d) Schematic representation of 33 mode [3]. (Reprinted with permission).....	12
1.10.	SEM images of stress controlled cantilevers consisting of a)PZT/ZrO <sub>2</sub> /SiO <sub>2</sub> (thermal), (b) PZT/ZrO <sub>2</sub> /SiO <sub>2</sub> (PECVD) and (c) PZT/ZrO <sub>2</sub> /SiO <sub>2</sub> (PECVD)/SiN <sub>x</sub> . (Reprinted with permission) .....	14
2.1.	Circuit representation of electrostatic converter [25]. (Reprinted with permission).....	19
2.2.	Spring-mass system with electrostatic and fluid damping forces.	

	(Reprinted with permission).....	20
2.3.	Out-of-plane gap closing electrostatic converter [25]. (Reprinted with permission).....	25
2.4.	In-plane gap closing electrostatic converter [25]. (Reprinted with permission).....	26
2.5.	(a) The schematic of an in-plane gap closing type accelerometer, redrawn as per the designed by I.Gonenli et al. [4] (Redrawn with permission) and (b) the two capacitances $C_1$ and $C_2$ between the combs of the structure.....	27
2.6.	In-plane overlap electrostatic converter. (Reprinted with permission).....	28
3.1.	Similarity between x-y sensing and in-plane gap closing converter schematic (a) 3D model of x-y_accelerometer_1605 device [4] (Reprinted with permission) (b) Redrawn schematic of the accelerometer x-y_accelerometer_1605 device [4]. .....	30
3.2.	Similarity between z- sensing and out-of-plane gap closing converter schematic (a) 3D model of z_accelerometer_650 device [4] (b) Out-of-plane gap closing schematic [4]. (Reprinted with permission). .....	30
3.3.	3D model for z_accelerometer_650 device with cantilevers (a) Top view of device1 with top electrode with 75% transparency showing tips of cantilever beams inserted between the top and bottom electrodes (b) Side view of z_accelerometer_650, showing electrical isolation of cantilever beams.....	34
3.4.	Illustration of the inter-digitated capacitance contributed by two side faces of a finger (a) A schematic of an in-plane gap closing type of electrostatic device (b) Inset showing the individual capacitance contributed by a set of fingers of a stationary and a moving electrode.....	36
3.5.	Conceptual model of cubic capacitance (a) Schematic showing an electrode inserted inside a hollow cubic enclosure (b) side view of the schematic showing capacitance contributed by all four faces of the electrode that is inserted in the hollow cubic enclosure.....	37
3.6.	A basic structure of novel energy harvester (not to the scale) showing stationary cantilever beams inserted in the hollow cubic proof mass (contact pads are not shown). .....	38
3.7.	The spring combinations (a) parallel spring combination (b) series spring combination.....	40

3.8.	Spring design	
	(a) A unit-cell of a U-shaped spring	
	(b) A series connection of 7 U-shaped springs, forming one serpentine spring. ....	41
3.9.	A layout of an energy harvester device, showing the dimensions of the proofmass and the serpentine springs. ....	42
3.10.	Model1_500CL35 (a) 3D view of the model in CoventorWare™, (b) A 3D view of the model showing the cantilever beams. The top plate of the cubic enclosure is not shown. (c) Another view of the 3D model showing the cantilever beams and the mechanical stop. ....	43
3.11.	Another view of the 3D model showing the cantilever beams and the mechanical stop for Model1_500CL35. ....	43
3.12.	Model2_24CL287 (a) 3D view of the model in CoventorWare™, (b) A 3D view of the model showing the cantilever beams. The top plate of the cubic enclosure is not shown. (c) and (d) Another view of the 3D model showing the cantilever beams and the mechanical stop. ....	46
3.13.	Model3_200CL203 (a) 3D view of the model in CoventorWare™ (b) A 3D view of the model showing the cantilever beams. The top plate of the cubic enclosure is not shown. ....	47
3.14.	Another view of the 3D model of Model3_200CL203 showing the cantilever beams and the mechanical stop. ....	48
3.15.	Illustration of various rest capacitances in case of Model3_200CL203. The double-sided arrows indicate the sites of the capacitance (the mechanical stop is not shown in the figure). ....	48
3.16.	Model2_24CL287.a: The modifications made to the Model2_24CL287, where the cantilever beam width is 50 $\mu\text{m}$ and the width of the side-walls is 10 $\mu\text{m}$ . ....	51
3.17.	Model3_200CL203.a: The modifications made to the Model3_200CL203, where the cantilever beam width is maintained at 5 $\mu\text{m}$ . ....	52
3.18.	Model3_200CL203.b: The modifications made to Model3_200CL203, where cantilever beam width is changed to 10 $\mu\text{m}$ . ....	52

3.19.	The modified Model3_200CL203.a, with sidewall width 10 $\mu\text{m}$ and cantilever beams width 5 $\mu\text{m}$ . (The top layer of the cubic enclosure is not seen in the figure).....	54
4.1.	An illustration of the boundary conditions applied to the accelerometer z_accelerometer650 [4]. .....	64
4.2.	Meshed models of z_accelerometer650 [4] .....	65
4.3.	An illustration showing the boundary conditions applied to Model3_200CL203.....	71
4.4.	An illustration showing the meshed 3D model of Model3_200CL203.....	72
4.5.	Simulation results for Model3_200CL203 (a) the displacement of the proofmass at an acceleration of 1.5g (b) Cantilever beams inserted within the hollow cubes, before the displacement (c) Cantilever beams coming out of the hollow cubes, after displacement. ....	73
A.1.	Layout of Model3_200CL203 illustrating the different layers used to build the 3D model of the device. The sacrificial layers are not seen in the figure. ....	91
A.2.	The process file for the energy harvesters for building the solid 3D model from the layout file. ....	92
A.3.	The 3D model of Model3_200CL203, built by using the layout file shown in Fig. A.1 and the process file shown in Fig. A.2.....	93
A.4.	The Mesher settings for the energy harvesters.....	94
A.5.	MemMechMM settings .....	94
A.6.	SurfaceBCs of the MemMechMM module, used to define the fixed patches on the device model. ....	95
A.7.	VolumeBCs of the MemMechMM module for specifying the load on the device. ....	95
A.8.	The Settings for the MemElectroMM module. The deformed mesh, which is obtained from the MemMechMM, is specified in the Geometry tab, highlighted in the red rectangle.....	96
A.9.	The settings for defining the voltage on the device .....	96

A.10.	The Settings of the MemMechMM for the Modal analysis, highlighted with red rectangle.....	97
A.11.	SpringMM settings for the analysis of spring constant.....	98
A.12.	Setting for the SpringMM using MechSringBCs (a) the MechSringBCs tab used for defining the boundary conditions for SpringMM (b) fixed-patches tab for defining the fixed areas (c) displaced_patched tab for defining the the displaced end of the spring (d) trajectories tab for defining the amount of displacement and the number of steps. ....	99

## LIST OF TABLES

1.11.	Acceleration and frequency in the fundamental mode of vibration for various vibration sources .....	7
1.12.	Comparative account of different energy sources along with the type of generators and their challenges .....	17
2.1.	Comparison of the vibration to electrostatic energy conversion cycles .....	23
3.1.	x-y sensing accelerometer device models designed by I. Gonenli [4].....	31
3.2.	z- sensing accelerometer models designed by I. Gonenli [4] .....	32
3.3.	Estimated spring constants for different displacements and the relative change in capacitance of a device .....	39
3.4.	The estimated spring constants for different spring thickness, width and the spring lengths. ....	43
3.5.	The dimensions of all the energy harvester models along with the dimensions of their modified models .....	53
3.6.	Proposed fabrication process flow .....	54
4.1.	MEMMech simulation results for x-y sensing accelerometers.....	65
4.2.	MEMMech simulation results for z_accelerometer650 [4] device for varied initial gaps between the electrodes.....	66
4.3.	The capacitance values for x-y sensing accelerometers .....	67
4.4.	The capacitance values for z_accelerometer650 .....	68
4.5.	Pull-in voltages for z_accelerometer650.....	68
4.6.	The results for the spring simulations .....	72
4.7.	Simulation results for the sagging of the proofmass of the energy harvesters .....	69
4.8.	Simulation results for the lateral displacement of the proofmass for the energy harvesters .....	74

4.9.	Simulation results for the capacitance analysis using MemElectroMM .....	77
4.10.	Simulation results for modal analysis.....	79
4.11.	The calculated electrostatic energy for charge-constrained conversion cycle .....	80
4.12.	The calculated electrostatic energy for the voltage-constrained conversion cycle.....	81
4.13.	The estimated power output for the accelerometer and energy harvesters .....	82
4.14.	The volumetric power output for accelerometer and energy harvesters .....	83
4.15.	The comparison of normalized volumetric power .....	85

## LIST OF SYMBOLS

<u>SYMBOLS</u>	<u>EXPLANATION</u>	<u>UNITS</u>
$a$	Source acceleration	$m/s^2$
$A$	Area of capacitive plates	$m^2$
$\alpha$	Transduction factor	-
$B$	Magnetic field strength	<i>Tesla</i>
$b_m(z, \dot{z})$	Mechanical damping force in a spring-mass system.	$N$
$b_e(z)$	Induced electrostatic damping force in a spring-mass system.	$N$
$C$	Capacitance	$F$
$C_v$	Variable capacitance	$pF$
$C_{par}$	Parasitic capacitance	$pF$
$C_{store}$	Storage capacitor	$pF$
$C_{max}, C_{min}$	Maximum and minimum capacitances of a variable capacitor	$pF$
$C_1$	Capacitance between the fingers of the inner electrode and proofmass of an accelerometer designed by I.Gonenli et al.	$pF$
$C_2$	Capacitance between the fingers of the outer electrode and proofmass of an accelerometer designed by I.Gonenli et al.	$pF$
$\Delta C$	Change in capacitance of a variable capacitor	$pF$
$d$	Initial gap between the electrodes of a variable capacitor	$m$



$d_c$	Damping coefficient of a spring-mass system	$Ns/m$
$d_{3i}, g_{3i}$	Piezoelectric constants of a piezoelectric material, where subscript $i$ stands for 1 or 3 to denote the coefficients in the 31 or 33-mode	$V/m, Vm/N$
$E_i$	Electric field generated on the piezoelectric material, where subscript $i$ stands for 1 or 3 to denote the field generated under 31 or 33-mode.	$V/m$
$E$	Electrostatic energy generated by an energy harvester	$J$
$f$	Frequency of vibration	$Hz$
$\epsilon_0$	Permittivity of free space	$F/m$
$h_f$	Thickness of the fingers of an inter-digitated comb structure	$\mu m$
$h$	Spring thickness	$\mu m$
$k$	Spring constant	$N/m$
$k_l$	Lateral spring constant	$N/m$
$k_v$	Vertical spring constant	$N/m$
$l_c$	Length of one magnetic coil	$m$
$L_i$	Length between the electrodes attached to a piezoelectric material, where subscript $i$ is either 1 or 3 such that $L_1$ is the thickness of the piezoelectric element for 31-mode and $L_3$ is the length of the piezoelectric element for 33-mode.	$\mu m$
$L$	Length of electrodes of a parallel plate capacitor	$\mu m$
$L_f$	Effective length of fingers of an inter-digitated comb structure	$\mu m$
$l$	Length of the spring	$\mu m$
$l_1$	Length of one leg of a u-shaped spring	$\mu m$

$l_2$	Length of the beam connecting the two legs forming a u-shaped spring	$\mu m$
$m$	Mass of a proofmass	$kg$
$N$	Number of turns of a magnetic coil	N/A
$N_g$	Number of gaps formed due to inter-digitated fingers	N/A
$P$	Power generated from an energy harvester	$\mu W$
$P_c$	Volumetric power generated using charge-constrained conversion mechanism	$\mu W/cm^3$
$P_v$	Volumetric power generated using voltage-constrained conversion mechanism	$\mu W/cm^3$
$Q$	Charge on a variable capacitor	$C$
$\sigma_{xx}$	Stress in a piezoelectric element	$Pa$
$SW1,$ $SW2$	Control switches for charging of variable capacitor	N/A
$V_{3i}$	Open circuit voltage generated in a piezoelectric material, where subscript $i$ stands for 1 or 3 to denote the voltage generated under 31 or 33-mode.	$V$
$V_{max}, V_{min}$	Maximum and minimum voltages on a variable capacitor	$V$
$V_{pi}$	Pull-in voltage between two capacitive plates	$V$
$W$	Width of electrodes of a parallel plate capacitor	$\mu m$
$w$	Width of each leg of the spring	$\mu m$
$\omega_n$	Resonant frequency of a proofmass	$radians/s$
$\omega$	Source frequency	$radians/s$

$x_3$	Strain in a piezoelectric material	$N/m^2$
$x$	Displacement of a proofmass	$\mu m$
$y(t)$	Amplitude of source vibrations	$\mu m$
$y$	Distance of a coil within the magnetic field	$\mu m$
$Y$	Young's modulus of a material	$Pa$
$z$	Displacement of flexures in case of an in-plane gap closing electrostatic converter	$\mu m$
$z_0$	Initial overlap of the fingers in case of an in-plane overlap electrostatic converter	$\mu m$
$z(t)$	Displacement of a proofmass with respect to stationary frame of device	$\mu m$
$\zeta_T$	Total damping ratio for a spring-mass system	-
$\zeta_e$	Electrical damping ratio for a spring-mass system	-

## CHAPTER 1

### INTRODUCTION

By the virtue of Moore's law, the electronics is going beyond a sub-micron level. Even though the size of circuits and devices and also the power requirements of these devices have been reduced, the technology is still limited by the size of the accompanying 'power' electronics. Over the years, efforts have been made to reduce the size of power-electronics which has now enabled high-speed wireless and portable devices. Researchers are making an effort to reduce the size of powering devices to micron scale and below, without compromising efficiency and power level.

This work is done in an effort to explore the feasibility of a MEMS device as an electric energy harvester, which would harness energy from a vibration source. The work is concentrated towards discussing the design aspects and the Finite Element Analysis (FEA) of a novel capacitive energy harvesting device.

#### 1.1 Need for MEMS power harvesting devices

As per the survey carried for the period 1990-2002 [5], the improvement in the battery energy is observed to be the slowest trend in the technical advancement, as far as the mobile computing is concerned, as shown in Fig. 1.1 [5].

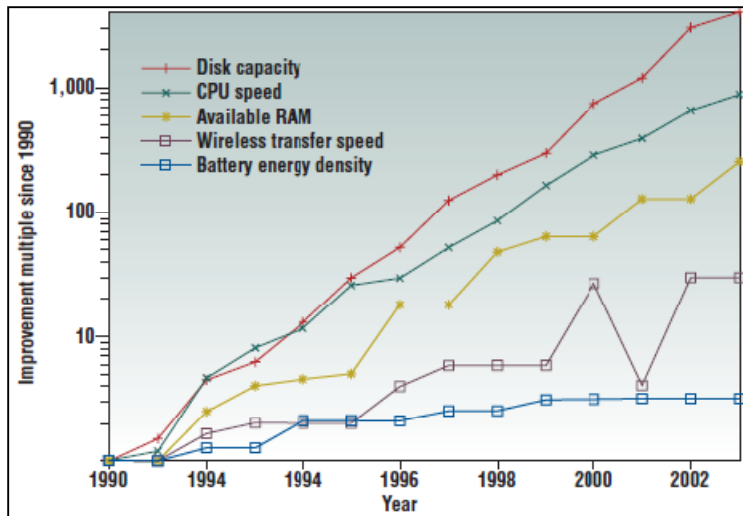


Fig. 1.1. Relative improvements in laptop computing technology from 1990-2003 [5]. (Reprinted with permission)

The various techniques of power management such as optimization of voltage, hybrid analog-digital designing, optimized duty-cycles of devices which keep the circuits inactive when not in use, etc., have managed to sustain longer life times for the battery operated electronics. Hence, as of now, batteries are the preferred energy sources for various wireless and mobile applications. However batteries are exhaustible and have a lifetime of few tens of years [6]. Hence it becomes mandatory to replace and dispose a battery, when it dies out. The replacement and disposal of the batteries can be a major task, given the wide spread sensor networks with the sensors as small as few microns in size.

MEMS, is a relatively new technology for integrating the mechanics and the electronics on a micron scale. Various MEMS sensors and actuators have become the basis of the pocket sized or even the wearable flexible electronics [7]. Thus, for exploiting the ambient energy, the MEMS technology becomes a promising option, in order to achieve a micro-power generator.

## 1.2 Various regenerative resources of power

The legacy of energy harvesting dates back to the centuries, when windmills and water-wheels were first used to harness the wind and the water energy. The emergence of solar panels,

thermoelectric generators and electromechanical devices, which enabled conversion of light, heat and vibration energy into electric energy elaborated the spectrum of power harvesting even further. However, as the miniaturization looms over the overall market, it becomes necessary to study how it affects the microelectronic power supplies.

Solar energy, the parental energy source for the life on the earth, has been one of the oldest and the most promising options for its conversion to electricity. The phenomenon of converting the solar energy to electrical energy is based on photovoltaic effect [8]. The silicon photovoltaic diodes have been used extensively for powering the telecommunication networks and satellites on a very wide scale [9].

A photovoltaic cell is nothing but a semiconductor diode, where semiconductor material absorbs the incident photons and as a result the atoms of the material are electronically excited, producing electron-hole pairs or excitons [8]. The electronic excitation in the semiconductor material creates a high-energy and a low-energy state. The electrons with an energy high enough ( $h\nu > E_{\text{gap}}$ ), cross the band-gap between the high-energy and the low-energy states and contribute to photoconduction. Direct-band gap semiconductors are preferred in order to use the light energy to its optimum value [9].

Apart from the light (photo) energy, the ambient heat is another inexhaustible source of energy which has been utilized over the decades for its conversion to the electric energy. The thermoelectric generators convert the waste heat into electrical energy. CMOS compatible micro-generators have been reported to generate a few micro-watts of power, which is sufficient enough for the micro-electronics [10].

The thermoelectric generators work on the principle of 'Seebeck effect', where the temperature difference is translated into potential difference (voltage) [10]. The sources of power for thermoelectric generators range from human-body heat to various automobile and the industrial mechanics, which offer a decent thermal-gradient with respect to the environment [11]. The Seebeck effect is prominently observed in the thermocouples [12].

The amount of open-circuit voltage generated due to a temperature gradient is measured in terms of the Seebeck coefficient. The charge carriers in the conductor flow in the same direction as that of the heat-flow [13], as shown in Fig. 1.2 [13]. In a typical thermocouple used for thermoelectric generation, p-type and n-type semiconductors are connected together by a metal plate as shown in the Fig. 1.2 [13]. The thermal gradient causes a flow of the charged carries thus generating a current.

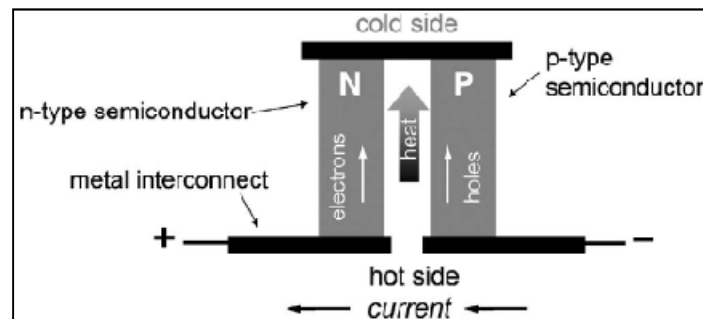


Fig. 1.2. Diagram of a thermocouple used for thermoelectric generation [13]. (Reprinted with permission).

A number of thermocouples are electrically connected in series and thermally connected in parallel, in order to generate enough thermoelectric power [14].

One of the first micromachined thermoelectric microgenerators was reported to provide 1 nW of power at the temperature gradient of  $\Delta T = 5$  K. The Seebeck coefficient of a single thermocouple made of p- and n-type of Silicon on sapphire, with leg dimensions of  $(4.5 \text{ mm} \times 20 \text{ } \mu\text{m} \times 0.4 \text{ } \mu\text{m})$ , was reported to be  $530 \text{ } \mu\text{V/K}$  [15]. Strasser et al. [10, 16], fabricated as many as 59400 thermocouples within an area of  $6 \text{ mm}^2$ , using the CMOS fabrication techniques. The open circuit potential and power density for thermal gradient of  $\Delta T = 5$  K were reported to be 0.8 V and  $1.5 \text{ } \mu\text{W/cm}^2$ , respectively.

Subsequently, a number of micro generator modules were developed. Various commercial setups started batch manufacturing of the thermocouples. Micropelt [17] has reported to produce a module consisting of 450 thermocouples, which are capable of producing 1200

$\mu\text{W}/\text{cm}^2$  and 0.5 V open circuit voltage at the thermal gradient of  $\Delta T = 5$  K. Each thermocouple was  $(20 \times 35 \times 35) \mu\text{m}^3$  in volume and  $\text{Bi}_2\text{Te}_3$  was the semiconductor material used for the fabrication, as shown in Fig. 1.3 [17].

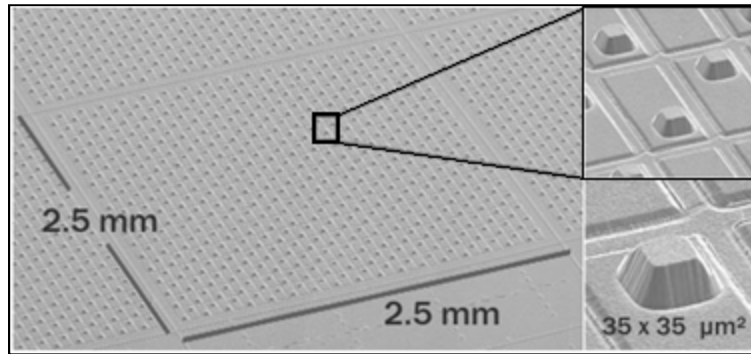


Fig. 1.3. Micro-graph of through-plane thermoelectric module [17]. (Reprinted with permission).

In the above mentioned examples, the flow of charge carriers is along the z-axis of the device i.e. the length of thermoelectric elements is determined by its thickness. Since the aspect ratios are limited by the fabrication constraints, it is not possible to increase the thickness of the elements beyond few tens of microns [16]. Rowe et.al [18] proposed another design schematic where meanders of p- and n-type of semiconductor materials were fabricated such that the thickness of each meander worked as the width of the leg of the thermocouple while the length of each element was along the span of the substrate, as shown in Fig. 1.4 [13].

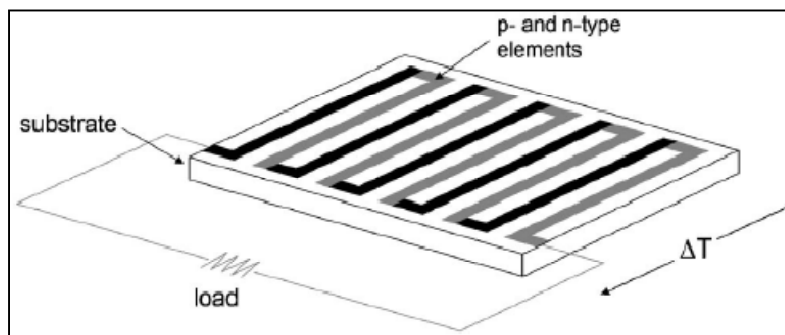


Fig. 1.4. Diagram of in-plane thermoelectric module [13]. (Reprinted with permission).

This design was reportedly cost effective and efficient since it supported techniques such as screen printing along with the microfabrication techniques. However, the major concern in this



design was the thermal conductivity of the substrate. Higher the thermal conductivity of the substrate higher the loss of thermal gradient and hence lower is the efficiency of the device [18]. Apart from heat and light energy, a lot of stray electromagnetic radiations are present in the environment. The RF signals present due to the telecommunication, television and radio transmitter antennas have an electric field strength with an incident power density of  $S$  ( $W/cm^2$ ) given by Eq. (1.1) [19]:

$$S = \frac{E^2}{R} \quad (1.1)$$

where,  $E$  is the electric field strength in  $(V/m)$  and  $R$  is the resistance of the free space ( $377 \Omega$ ) [19]. As per the survey carried out in 2006 in Denver [19], the power densities were measured on the interior and the exterior of the houses in the range of 3 Km from the TV and radio transmitting towers. The average power on the interior of the houses was measured to be around  $0.8 \mu W/cm^2$  while that on the exterior was measured to be  $2.6 \mu W/cm^2$  [19]. These potential electromagnetic waves can be converted into ac or dc electric power. The electric field strength of the waves determines the maximum electric power that can be harvested [19]. In recent years, stray electromagnetic radiations have also been tapped for extracting the electrical energy.

The first rectenna [19] array was proposed by Hagerty et al. [19, 20]. Waves of different frequencies and power levels present in the environment are received by dual-polarized array of antennas. Each antenna is integrated with rectifying circuit forming a rectenna [19, 20]. The rectified signals were then fed to power-management system. An output voltage of 3.5 V and a power density of  $7.8 mW/cm^2$  were reported. The same group proposed another schematic for the rectenna arrays with spiral antennas each of radius 15 mm, as shown in Fig. 1.5 [19, 20]. The antennas operated on the frequency range of 6 to 15 Hz and exhibited open circuit voltage of 4 V and a power density of  $1.6 mW/cm^2$  [20].

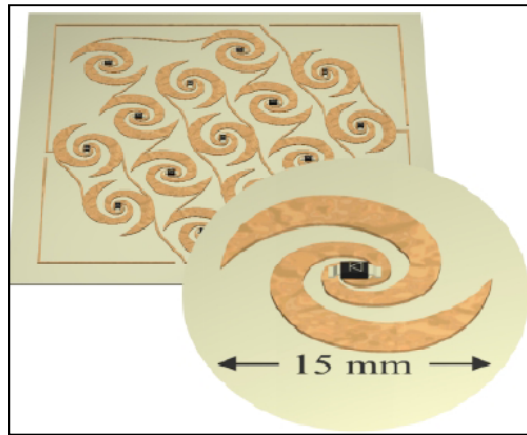


Fig. 1.5. Array of spiral antennas which include broad band elements with orthogonal circular polarization [20]. (Reprinted with permission).

Apart from the conventional energy sources such as solar, wind, light and RF power, stray vibrations are also another promising source of energy. The mechanical energy present in the vibrations can be converted to electricity [20]. There are enough sources, in the environment, which can work as potential sources of vibration energy. Table 1.1 [21] shows various vibration energy sources.

Table 1.1. Acceleration and frequency in the fundamental mode of vibration for various vibration sources [22].

Vibration source	Acceleration ( $m/s^2$ )	Frequency (Hz)
Car engine compartment	12	200
Base of 3-axis machine tool	10	70
Blender-casing	6.4	121
Clothes dryer	3.3	121
Person nervously tapping his feet	3	1
Door frame just after the door closes	3	125
Small micro-wave oven	2.25	121
HVAC vents in buildings	0.2-1.5	60
CD on note-book computer	0.6	75
Second story floor of busy office	0.2	100

The three basic techniques that have been extensively explored by researchers until now for the vibration-to-electricity conversion are:

- a. using piezoelectric material
- b. using electromagnetic principle of conversion

c. using electrostatic principles [22].

All the above techniques obey the basic mechanism, wherein the proof mass  $m$ , shown in Fig. 1.6 [22], is subjected to vibrations, which cause a change in the strain (as in case of piezoelectric material based micro-generators [22]), or a change in the magnetic field (as in case of electromagnetic micro-generators [23]) or a change in the capacitance of the device (as in case of electrostatic micro-generators [24]).

A mechanical model of a vibration based transducer is shown in the figure below.

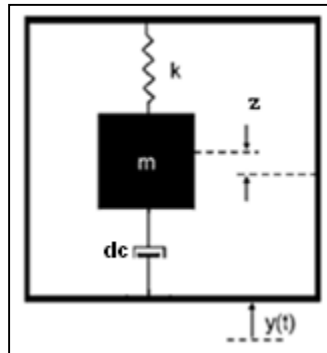


Fig. 1.6. Spring-mass system with electrostatic and fluid damping forces [25]. (Reproduced with permission)

It consists of a proof mass, which is attached to a spring of spring constant  $k$ , as shown in Fig. 1.6 [25]. On application of a vibration force, the proof mass moves relatively to the frame of the system [25]. For the vibrations of amplitude of  $y(t)$ , the resultant motion of the proof mass, with respect to the frame of the device is represented by  $z(t)$ . The movement of the proof mass is then given by second order equation of motion [25] as given below:

$$m\ddot{z}(t) + d_c\dot{z}(t) + kz(t) = -m\ddot{y}(t) \quad (1.2)$$

The right hand side of the equation represents the force exerted by the source on the proof mass while the left-hand side represents the dissipation of that force through the proof-mass, the damper elements and the spring attached [21]. While analyzing the dynamics of the mass-spring-damper system, a few assumptions are taken into consideration, (1) the mass of the

source is much greater than that of the proof mass, (2) the vibration source is an infinite source of power [21].

The spring mass system, in most cases, is subjected to the damping forces, represented by  $d_c$  in the Fig. 1.6 [25]. The damping forces are constituted mainly by the fluid and the electrical damping. The fluid damping is a parasitic resistance due to air. For a free movement of the proofmass, it is desirable to minimize the fluid damping of the system. The electrical damping is used to determine the amount of energy that is removed from the mechanical subsystem and stored in the electrical system [25]. Hence, the expression of the electrical damping term is of prime interest for the design of a vibration based energy generators. The numerical expressions of both the damping coefficients depend on the device design and the type of conversion mechanism being implemented [25].

Since the nature of source vibrations is oscillatory, the movement of proof mass is also oscillatory in nature. The resonant frequency of the proof-mass is given by

$$\omega_n = \sqrt{\frac{k}{m}} \quad (1.3)$$

where  $\omega_n$  is the resonant frequency of the proofmass and  $k$  is the spring constant of the spring attached to the proofmass  $m$  [25].

The damping factors are determined on the basis of the conversion mechanisms used. Hence, in the following section, piezoelectric and electromagnetic energy converters are discussed in brief, while electrostatic microgenerators are discussed in detail in Chapter 2.

### 1.2.1 Electromagnetic microgenerators

An electromagnetic transducer works on the principle of Faraday's law, which states that the change in magnetic flux generates a voltage [26], as given in Eq. (1.4)

$$V = NBl_c \frac{dy}{dt} \quad (1.4)$$

where,  $N$  is the number of turns in the coil,  $B$  is the magnetic field strength,  $l_c$  is the length of one coil, while  $y$  is the distance of coil within the magnetic field. The electromagnetic energy harvesters are realized by designing either a moving coil or a moving magnet, so that there is a change in the magnetic field [9]. S.Roundy et al. estimated that not more than 100 mV could be generated from a device of volume of  $1 \text{ cm}^3$  at an acceleration of  $2.25 \text{ m/s}^2$  [27].

One of the first electromagnetic generators was proposed by C.B. Williams and Yates et al [25]. The proposed design had dimensions of  $(5 \times 5 \times 1) \text{ mm}^3$  and was expected to generate  $1 \text{ }\mu\text{W}$  of power at an acceleration of  $9.7 \text{ m/s}^2$ . The estimated power output of  $1 \text{ }\mu\text{W}$  was calculated for a very large displacement of the order of  $30\text{-}50 \text{ }\mu\text{m}$  [28]. However, the actual fabricated device was nearly  $4\text{mm}^3$  with resonant frequency as high as  $4.4 \text{ KHz}$ , and the power generated was reported to be  $0.3 \text{ }\mu\text{W}$  at a very high acceleration of  $380 \text{ m/s}^2$  [27]. The major reason for the discrepancy in the estimated and the measured output power was reportedly attributed to the small displacement because of the stiffness of the springs, in addition to the few other factors such as aerodynamic and material damping and hysteresis losses [28]. Another device was proposed by R. Amirtharajah and Chandrakasan et al. [28]. The device dimensions were not specified, however, the resonant frequency was reported to be  $94\text{Hz}$  and the output voltage was reported to be  $180 \text{ mV}$ . The prototype consisted of a coil and a permanent magnet attached to the frame.

El-hami et al. [29] proposed a cantilever-based electromagnetic transducer, shown in Fig. 1.7.(a) [2]. The latest version of the optimized design was reported to have a volume of  $0.15 \text{ cm}^3$  and it was reported to generate the power of the order of  $46 \text{ }\mu\text{W}$ , at an acceleration of  $0.59 \text{ m/s}^2$ . S.P. Beeby et al. [2] proposed another novel design with a four-magnet configuration, as shown in Fig. 1.7. (b) [1]. The optimized prototype had predicted a power output of  $148 \text{ nW}$  with a device as big as  $106 \text{ mm}^3$  having a resonant frequency of  $8.08 \text{ KHz}$  [1].

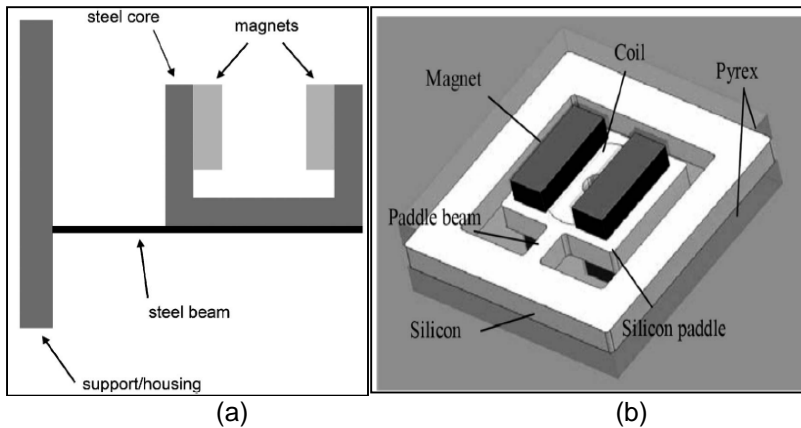


Fig. 1.7. Electromagnetic microgenerators (a)Diagram of cantilever-based micro generator [1] and (b) Micromachined version of four-magnet design [2]. (Reprinted with permission).

### 1.2.2 Piezoelectric microgenerators

In case of piezoelectric materials the change in the mechanical strain causes a change in the potential gradient. The converse is also true. Basic transduction mechanism is summarized in Fig. 1.8.

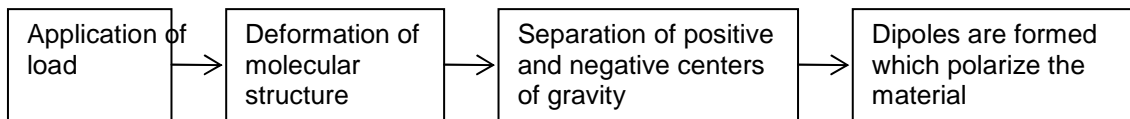


Fig. 1.8. Flow chart for piezoelectric activity.

The voltage is generated either laterally or perpendicularly to the direction of applied strain. When the voltage is generated along the axis same as that of the applied force the material is said to be working in mode-33. On the other hand, when the voltage generated is in the direction perpendicular to that of the applied strain, the material is said to be working in mode-31 [1]. The Fig. 1.9 illustrates the concept behind the nomenclature used for defining the modes of a piezoelectric material.

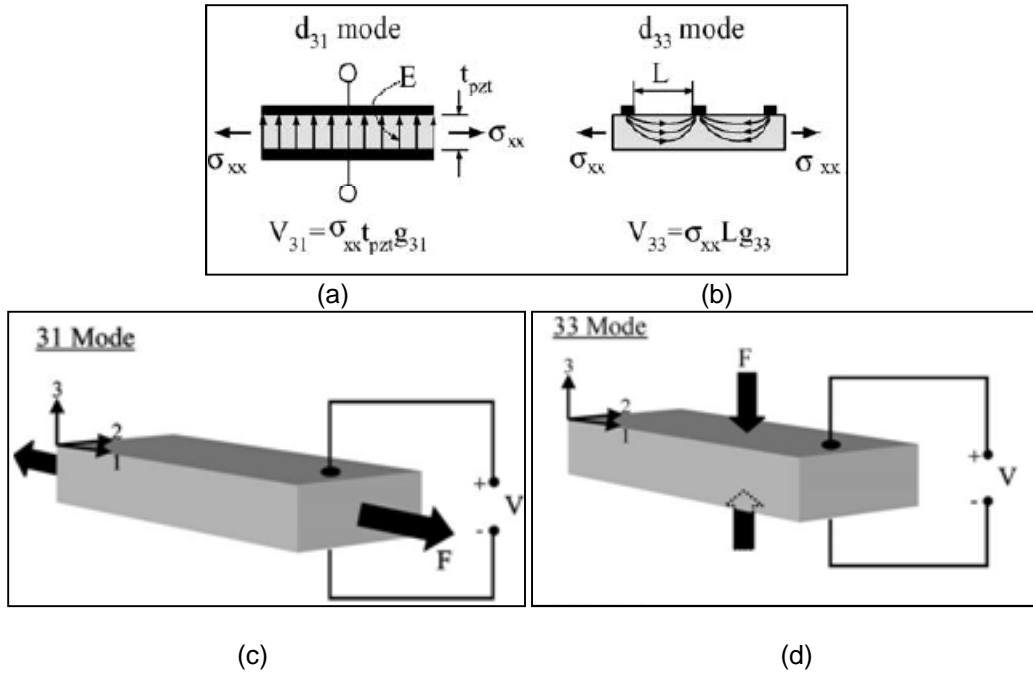


Fig. 1.9 The two modes of piezoelectric conversion from mechanical stress (a)31-mode, (b)33-mode [3] (c)Schematic representation of 31 mode and (d) Schematic representation of 33 mode [3]. (Reprinted with permission).

In Fig.1.9 (c) and 1.9 (d) [22],  $F$  is the direction of the force applied while  $V$  is the open circuit output voltage. The relation between the applied strain and the electric field is given by Eqs. (1.5) and (1.6) [22]:

$$x_3 = d_{3i} V_{3i} \quad (1.5)$$

$$V_{3i} = \sigma_{xx} g_{3i} L_i \quad (1.6)$$

where,  $x_3$  is the strain,  $V_{3i}$  is the generated open circuit voltage,  $d_{3i}$  (V/m) and  $g_{3i}$  (Vm/N) are the piezoelectric constants, while  $L_i$  is the distance between the electrodes. In the case of mode-33,  $L$  represents length of the piezoelectric element while in case of the mode-31, it represents the thickness of the element [3]. The piezoelectric coefficient in mode-33 is higher than that in the 31 mode. However, it is easier to implement a transducer in the mode-31 [29].

The most commonly used piezoelectric material is lead zirconate titanate (PZT) ceramic, while a cantilever beam design is the most commonly used schematic [3]. However, J. A.

Paradiso et al. [30] proposed a novel model of a piezoelectric transducer, which was used in the sole of a shoe and harvested energy, when a person is walking. The device was made of a flexible polyvinylidene fluoride (PVDF) bimorph stave, which was placed under the insole and worked in mode-31 [31]. The average power generated for a load of 250 k $\Omega$  was measured to be 1.3 mW at a frequency of 0.9 Hz. The same group had proposed another method where the PZT was used as a piezoelectric element and the energy was generated at the strike of the heel of a shoe. This device consisted of two bent, prestressed PZT strips, which compressed at each strike of the heel and generated a power of 8.4 mW at the walking frequency of 0.9Hz [31].

In the league of conventional cantilever based piezoelectric generators, S. Roundy et al. [31] reported one of the best PZT based devices. The total size was constrained to 1 cm<sup>3</sup>. The device was reported to have a resonant frequency of 100Hz and produced 210  $\mu$ W at an acceleration of 2.25 m/s<sup>2</sup> [22]. Prior to this device, S. P Beeby et al. [22] had proposed a microgenerator, which was made of steel beam and a paste of piezoelectric material like PZT was screen printed on it. On the application of strain, it produced 2.1  $\mu$ W at an acceleration of 230 m/s<sup>2</sup>. The total volume of the beam was reported to be 0.125 cm<sup>3</sup> [32].

Another device that worked on mode-33 of the piezoelectric material was reported by Y.B. Jeon et al. [32], as shown in Fig. 1.10 [3]. The device fabrication technique was modified in order to reduce the internal stress induced in the cantilever during the fabrication process. First, SiN<sub>x</sub>, ZrO<sub>2</sub> and PZT layers were spin coated on the silicon substrate and patterned with the Reactive Ion Etching (RIE). The integrated platinum electrodes were then reportedly formed by e-beam evaporation. The platinum electrodes were designed in order to exploit the 33-mode of the piezoelectric PZT. A power output of 1.0  $\mu$ W was reported at an acceleration of 110 m/s<sup>2</sup> and the resonant frequency was of 13.9 KHz. The volume of the cantilever beam was 0.2 mm<sup>3</sup> [3].



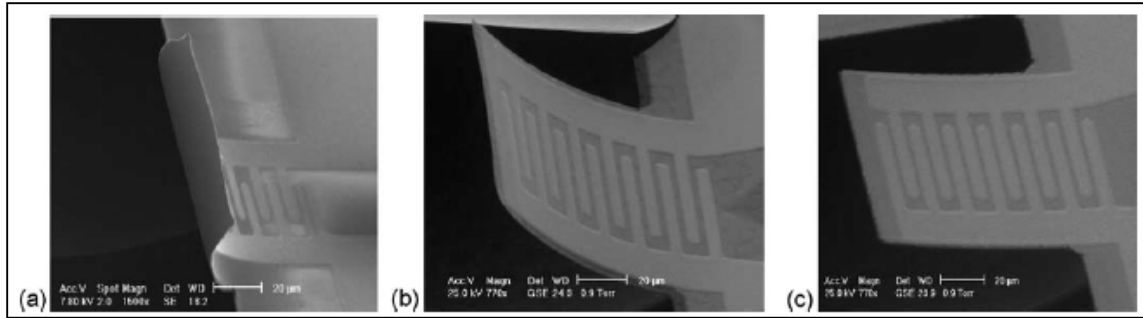


Fig. 1.10. SEM images of stress controlled cantilevers consisting of a)PZT/ZrO<sub>2</sub>/SiO<sub>2</sub>(thermal), (b) PZT/ZrO<sub>2</sub>/SiO<sub>2</sub>(PECVD) and (c) PZT/ZrO<sub>2</sub>/SiO<sub>2</sub>(PECVD)/SiN<sub>x</sub>. [3] (Reprinted with permission)

Another promising piezoelectric device was reported by Fang et al. [3] in which the cantilever beam was reported to have the dimensions of 1.2 mm<sup>3</sup> and produced 2.16 μW at an acceleration of 9.8 m/s<sup>2</sup>. A large proof mass was used to increase the mass of the device and bring down the resonant frequency to 609 Hz.

### 1.2.3. Electrostatic microgenerators

Another mechanism, which is used to convert the vibrations to electricity, is electrostatic transduction. In this case, the change in the capacitance of the device is translated into the electrical energy. The movement of the spring flexures is responsible for the movement of the proof mass, which causes the change in capacitance.

One of the major concerns associated with electrostatic transduction, is the need of initial voltage source for the charging of the electrodes of the capacitor. Once the capacitive device is charged, the transduction can be done either by (a) keeping the voltage on the capacitor constant and varying the charge, or by (b) keeping the charge on the capacitor constant and varying the voltage [33]. One more method which is preferable is use of electrets where in the charge density of a polarized electret is changed due to the motion of the electrodes and hence, causes the flow of current through the load [34].

The three basic topologies that are generally used for designing an electrostatic microgenerator are as follows [35]:

1. In-plane gap closing topology, where the gap between the inter-digited capacitor electrodes is varied.
2. In-plane overlap topology, in which the overlap area of the fingers of the inter-digited capacitor is changed
3. Out-of-plane topology, where one of the capacitor electrodes is fixed, while the other electrode moves in the z-direction, thus changing the distance between the two parallel plates.

The conversion cycles and the design topologies for the electrostatic micro-generators are elaborated in Chapter 2.

### 1.3 Challenges in designing of microgenerators

Even though the thermal and light energy are evidently promising inexhaustible sources, the power-generation using these sources comes with its own set of challenges. In the case of thermoelectric generators, the voltage output is directly proportional to the temperature gradient. Hence, with a low ambient temperature, the voltage output will also be low [10]. In addition, the output voltages are also susceptible to the temperature fluctuations. Similarly, for the photovoltaic generators, the power output depends upon the intensity of the incident light. Hence, the power outputs are low for the environments with a poor light quality. In such cases, the generators need the booster circuits and the conditioning circuits which would increase the low-scale voltages to an effective range, which is suitable for a given load [16].

While designing a RF micro-power harvester, a major challenge is to constrain the size of the antenna. The antenna size is related to its operating frequency. Smaller the antenna size greater is the operating frequency [13]. For example, a millimeter sized antenna would work at the frequency which is of the range greater than 100 GHz [13]. However, the RF radiations work on a much smaller scale of frequencies, which are of the range of  $10^{11}$  Hz. Hence, for the smaller antennas, it is difficult to achieve a good efficiency and a high band width, both at the same time. Another problem associated with RF generators, is dealing with the unknown power spectral densities and the polarization signals. This requires the harvester to work on a wide range of

frequencies [13]. An efficient micro-generator would require an improvement in the operating frequency band-width, along with the integration with MEMS or IC fabrication processes.

On the other hand, in case of a vibration based generator, the major challenge is to design a small size proofmass with low resonant frequency, which is comparable to the ambient source frequency. The resonant frequency is inversely proportion to the  $\sqrt{m}$  (where  $m$  is the mass). Hence, any change in the mass changes the resonant frequency as well. Hence, it is difficult to design a system with a small size, low resonant frequency and an adequate power output. In most cases, resonant frequency is compromised for the size that causes a loss in the generated power, because of disproportionate resonance [29].

In case of electromagnetic microgenerators, in addition to the basic challenge of designing a proof mass, another major challenge is to incorporate the magnetic elements into the batch fabrication process. The flexures and the proofmass can be fabricated with microfabrication processes. However, the magnetic coil needs to be manually assembled [36]. On the other hand, if the generators are integrated with the microchips, an arrangement needs to be done, to avoid the interference of magnetic-field with the rest of the electronics.

The problem of batch fabrication is taken care of, in case of electrostatic microgenerators [13]. In fact electrostatic microgenerators are very well compatible with the MEMS fabrication processes. However, the prime concern is the requirement of an initial voltage source to charge the capacitor plates, for which, the electrets are most commonly used polarizing materials. The electrets are the polarized insulators, which can hold the charge for several decades [34].

Apart from the requirement of initial voltage source, another problem associated with electrostatic microgenerators is a possibility of an accidental short-circuiting of the electrode plates, which causes the loss of energy that is built up in the device. Hence, it is important to design a device with suitable mechanical stops. This can be difficult especially in case of out-of-plane type micro-generators [35].

#### 1.4 Summary

Various inexhaustible energy resources and their utilization for generating power for micro-electronics have been discussed. Even though every transduction methodology has its own set of challenges, the need of microgenerators is inevitable because of the short life time of batteries. Following table gives the concise account of all the energy resources discussed so far.

Table 1.2. Comparative account of different energy sources along with the type of generators and their challenges.

Source of Energy	Transduction principle	Type of micro-generators used	Challenges
Light	Generation of charged carries due to incident photon energy [9].	Photovoltaic cell	<ol style="list-style-type: none"> <li>1. Low intensity of light/ ambient temperature produces less energy.</li> <li>2. Susceptibility to the variation in intensity of incident energy [10, 12, 13].</li> </ol>
Heat	Seebeck effect: generation of potential gradient due to thermal gradient [11].	Thermocouple arrays	
RF power	Extraction of electric energy present in electromagnetic waves [20].	Antenna arrays	<ol style="list-style-type: none"> <li>1. Size constraint</li> <li>2. Achieving wide operating frequency range [13].</li> </ol>
Vibrations	Generation of energy due to change in <ol style="list-style-type: none"> <li>1. Magnetic field (electromagnetic transduction) [21, 22, 24].</li> <li>2. Strain in material (piezoelectric transduction) [3, 21, 22].</li> <li>3. Capacitance of structure (electrostatic transduction) [21, 22, 25].</li> </ol>	Vibrating devices with a proof mass attached to springs.	<ol style="list-style-type: none"> <li>1. Achieving low resonant frequency of small proof mass.</li> <li>2. Assembly of magnetic component in case of electromagnetic transducers.</li> <li>3. Need of initial voltage source and device stability in case of electrostatic transducers [13, 21, 22].</li> </ol>

CHAPTER 2  
CONVERSION MECHANISM AND DESIGN TOPOLOGIES  
FOR ELECTROSTATIC MICROGENERATORS

2.1 Introduction

As discussed in the previous chapter, the vibration-based energy harvesters are spring-mass systems. In case of the electrostatic energy harvesters, the generation of the electrical energy is based on the change in capacitance of a variable capacitor. The variable capacitor is realized by a moving electrode, which is represented by the proofmass, and a stationary electrode, which is generally attached to the substrate. During one cycle of the source vibrations, the proof mass of the device moves to and fro with respect to its rest position, and hence, distance between the electrodes of the capacitor changes. Due to the change in the distance between the electrodes, the capacitance of the structure changes from maximum to minimum or vice-a-versa. As the capacitance of the structure changes, either the charge or the voltage on the capacitor can be constrained while changing the other. Thus, there are two primary conversion cycles (1) charge constrained and (2) voltage constrained conversion cycles [37]. The parameter, which is changing, is utilized to evaluate the total amount of work done i.e. the total amount of the energy, generated in one vibration cycle. This mechanism is discussed in detail in this chapter.

The capacitance of a capacitive structure is given by the Eq. (2.1):

$$C = \frac{\epsilon_0 A}{d} \quad (2.1)$$

where,  $\epsilon_0$  is the permittivity of the free space,  $A$  is the overlapping or the effective area of the electrodes and  $d$  is the distance between the electrodes. In order to change the capacitance of the device, either the area  $A$  or the distance  $d$  can be changed. Hence, depending upon the design of the device, the capacitance and the change in the capacitance of the device can be

determined. Hence, the three major design topologies, namely 1) Out-of-plane gap closing, 2) In-plane gap closing and 3) In-plane overlap type, are also discussed in this chapter.

## 2.2 Charge-constrained conversion cycle

As the name suggests, in case of the charge-constrained conversion cycle, the charge on the variable capacitor is held constant while the voltage changes, with the change in capacitance. The charge-constrained conversion cycle can be explained with the help of the circuit diagram, as shown in Fig. 2.1 [25].

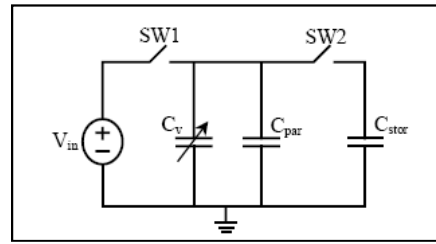


Fig. 2.1. Circuit representation of electrostatic converter [25]. (Reprinted with permission).

In the Fig. 2.1 [25],  $V_{in}$  is a input voltage source,  $C_v$  is the variable MEMS capacitor,  $C_{par}$  is the parasitic capacitance of the device, while,  $C_{stor}$  is the storage capacitor.  $SW_1$  and  $SW_2$  are the two switches which control the charging of the capacitors. The operation of the circuit, given in Fig. 2.1 [21], is explained in this section.

When  $C_v$  is at  $C_{max}$ , where  $C_{max}$  is the maximum capacitance of the device, the switch  $SW_1$  is closed while  $SW_2$  is open. The charge is transferred from input source to the variable capacitor. The capacitor is now said to be pre-charged. The charge on the capacitor is given by:

$$Q = C_{max} V_{in} \quad (2.2)$$

Once the variable capacitor is pre-charged, the switch  $SW_1$  is immediately opened to isolate the variable capacitor from the source and hence, forcing it to retain the charge. While  $SW_1$  and  $SW_2$  both are open, the distance between the electrodes changes from minimum to maximum due to the vibrations. Hence, the capacitance of the variable capacitor is changed from

maximum to minimum. Since, the charge  $Q$  is constrained, the voltage changes with the change in capacitance of the structure, as illustrated in Eqs. (2.3) and (2.4).

$$Q = C_{\max} V_{\min} \quad (2.3)$$

⇓ ⇓

$$Q = C_{\min} V_{\max} \quad (2.4)$$

Thus, as the work is done on the electrodes, the voltage over the capacitor increases. The increase in the voltage increases the electrostatic energy stored in the capacitor.

In order to transfer the charge from the variable capacitor  $C_v$  to the storage capacitor  $C_{store}$ , the switch  $SW_2$  is closed, while  $SW_1$  is still open and the charge stored on  $C_v$  is transferred to  $C_{store}$ .

The electrical damping coefficient is then used, to derive the expression for the electrostatic energy that is generated. To determine the electrical damping coefficient, the energy harvester is analyzed as a spring-mass system, as explained in Chapter 1. The expression for the electrical damping coefficient is derived in the following section.

Fig. 2.2 [25] shows a spring-mass system, where  $m$  is the proof mass, which is a moving electrode,  $b_m(z, \dot{z})$  represents the fluid damping term,  $b_e(z)$  represents the electrostatic damping term,  $z$  is the deflection and  $k$  is the spring constant of the springs attached to the proofmass or the moving electrode.

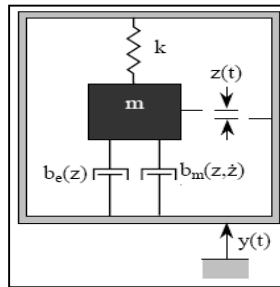


Fig. 2.2. Spring-mass system with electrostatic and fluid damping forces [25]. (Reprinted with permission).

The fluid damping can be reduced to a negligible value, if the device is vacuum packaged [25]. Assuming a vacuum packaged device, in this work, the fluid damping coefficient is assumed

to be too small to consider. Hence, only the electrostatic damping coefficient is derived. The electrostatic damping coefficient also represents the electrostatic force induced in the system when the energy is transformed from the mechanical system to the electrical system. The electrostatic damping coefficient is given by [25]:

$$b_e(z) = \frac{V_{in}^2}{2} \left[ \frac{d}{dz} (C_v) \right] = \frac{Q^2}{2} \left[ \frac{d}{dz} \left( \frac{1}{C_v} \right) \right] \quad (2.5)$$

where,  $Q$  is the charge stored on the variable capacitor and is given by  $C_v V_{in}$  [25].

The total energy stored in the system is calculated by integrating the total amount of the force induced in one complete cycle of vibration [25]:

$$E = \int_0^{2\pi/\omega} |b_e(z)| dz \quad (2.6)$$

where,  $E$  is the electrostatic energy induced in the system and  $(2\pi/\omega)$  is the period of one cycle of vibrations with  $\omega$  ( $\omega = 2\pi f$ ) as the frequency of the source vibrations.

The induced electrostatic force depends upon the change in the capacitance, which is a function of the deflection of flexures. Over one complete cycle of vibrations, the deflection of flexures is assumed to vary from minimum ( $z_{min}$ ) to maximum ( $z_{max}$ ). Hence, we can rewrite the equation for the electrostatic energy in terms of the deflection of flexures as given in Eq. (2.7):

$$E = \int_{z_{min}}^{z_{max}} |b_e(z)| dz \quad (2.7)$$

From Eq. 2.5, Eq. (2.7) becomes:

$$E = \frac{Q^2}{2} \int_{z_{min}}^{z_{max}} \left\{ \left[ \frac{d}{dz} \left( \frac{1}{C_v} \right) \right] \right\} dz \quad (2.8)$$

$$E = \frac{Q^2}{2} \left[ \frac{1}{C_v(z_{max})} - \frac{1}{C_v(z_{min})} \right] \quad (2.9)$$



$$E = \frac{Q^2}{2} \left[ \frac{1}{C_{v\min}} - \frac{1}{C_{v\max}} \right] \quad (2.10)$$

$$E = \frac{Q^2}{2} \left[ \frac{C_{v\max} - C_{v\min}}{C_{v\max} C_{v\min}} \right] \quad (2.11)$$

Using Eq. (2.2) and replacing  $Q^2$  by  $(C_{v\max} V_{in})^2$ , Eq. (2.11) becomes:

$$E = \frac{V_{in}^2}{2} [C_{v\max} - C_{v\min}] \left[ \frac{C_{v\max}}{C_{v\min}} \right] \quad (2.12)$$

$$E = \frac{V_{in}^2}{2} \Delta C_v \left[ \frac{C_{v\max}}{C_{v\min}} \right] (J) \quad (2.13)$$

From the above equation, it is observed that in case of a charge-constrained conversion cycle, the electrostatic energy is directly proportional to the change in capacitance, input voltage and to the tuning range of the capacitor i.e. the ratio of  $C_{\max}$  to  $C_{\min}$ .

### 2.3 Voltage-constrained conversion cycle

In case of a voltage-constrained conversion cycle, the voltage on the variable capacitor is held constant using a constant voltage source, while the charge on the capacitor varies as per the change in capacitance [38].

First, the variable capacitor is pre-charged when its capacitance is at maximum  $C_{v\max}$ . Thus, the charge on the capacitor is given by [25]:

$$Q_{\max} = C_{v\max} V_{in} \quad (2.14)$$

With the voltage source still connected to the capacitive plates, the capacitance of the device, changes from maximum to minimum as the distance between the capacitor plates is assumed to increase due to the vibrations. Hence, the capacitance changes from  $C_{v\max}$  to  $C_{v\min}$  and accordingly the charge on the capacitor changes from  $Q_{\max}$  to  $Q_{\min}$ . As the capacitive plates move with respect to each other, some energy is stored in the system due to the work done by the capacitor plates.

For a constant input voltage, the electrostatic energy  $E$  of a capacitor is given by [25]:

$$E = \frac{1}{2} QV_{in} \quad (2.14)$$

Hence, the electrostatic energy, which is generated due to the work done, is given by:

$$E_{harvested} = \frac{1}{2} (Q_{max} - Q_{min}) V_{in} \quad (2.15)$$

Eq. (2.15) can be written as:

$$E = \frac{1}{2} V_{in}^2 (C_{v,max} - C_{v,min}) \quad (2.16)$$

$$E = \frac{1}{2} V_{in}^2 \Delta C_v \quad (2.17)$$

Hence, in case of the voltage constrained conversion cycle, the energy generated is directly proportional to the change in capacitance and half the square of the input voltage. Table 2.1. compares the two conversion cycles in brief.

Table 2.1. Comparison of the vibration to electrostatic energy conversion cycles

Charge Constrained Conversion	Voltage Constrained Conversion
Charge on the variable capacitor is held constant	Voltage across the variable capacitor is held constant
Voltage on the capacitor increases to contribute to the energy	Charge on the capacitor changes and the change in the charge is transferred back to the source. Variable capacitor acts as a current source
The energy is stored in the storage capacitor	The energy generated is collected back into the source along with the variable capacitor discharging into the source
Advantage: Constant voltage source is not required.	Advantage: No need of switching mechanism
Disadvantage: Switching mechanism is required.	Disadvantage: Constant voltage source is required. It can be in the form of source capacitor or electrets [34].

For both conversion cycles, the change in capacitance and the amplitude of input charging voltage are the common factors, which are responsible for obtaining the electrostatic energy. A large change in capacitance is achieved by obtaining large displacements of the movable electrode i.e. the proofmass. At the ambient source vibrations, a large displacement is difficult to achieve with a small proofmass, since the ambient vibrations are of a very low magnitude. Hence, they do not provide enough force ( $\text{force} = \text{mass} \times \text{acceleration}$ ) to displace a small proofmass [35]. Therefore, it is not possible to obtain a large amount of energy, based only on the change in the capacitance. On the other hand, it is possible to increase the input voltage in order to increase the output energy. However, in case of an electrostatic microgenerator, the maximum input voltage is limited by the pull-in voltage of the capacitor. The pull-in voltage is defined as the voltage at which the two capacitive plates short-circuit each other, due to the induced electrostatic force and discharge the capacitor. In addition to the discharge of the capacitor, the generated power is lost due to the short circuit [25]. For this reason, it is important to avoid the pull-in between the two electrodes. One of the solutions to avoid pull-in, is to include the mechanical stops in the design of the variable capacitor.

This work is focused on the design of a MEMS capacitive-device which can achieve a significant change in the capacitance, with high pull-in sustenance of the device, so that high input voltages can be applied to get a significant output power.

For the devices designed here, the power output is evaluated for the charge-constrained as well as the voltage-constrained conversion cycles in Chapter 4.

#### 2.4 Design topologies for electrostatic energy harvesters

The three basic topologies for realizing an electrostatic energy harvester were discussed in detail by S. Roundy et al. [22, 25, 35]. Two of the three schematics are inter-digitated variable capacitors, where either the gap or the overlapping area between the adjacent fingers is changed with the motion of the proof mass. The third schematic is an out-of-plane parallel plate capacitive

module, where the bottom plate is stationary while the top electrode moves in the z-direction, changing the gap between the two plates.

#### 2.4.1. Out-of-plane gap closing converter [35]

The capacitance of a parallel plate capacitor is given by [25]:

$$C_v = \frac{\epsilon_0 A}{d} \quad (2.18)$$

where,  $C_v$  is a variable capacitance,  $A$  is the area of the electrodes,  $\epsilon_0$  is the permittivity of the free space and  $d$  is the gap between the two electrodes.

In case of a out-of-plane schematic, the capacitance, for the electrodes of area given by

$$A = W \times L \quad (2.19)$$

where,  $W$  is the width and  $L$  is the length of the electrodes, the Eq. 2.18 [25] can be rewritten as

$$C_v = \epsilon_0 WL \frac{1}{d} \quad (2.20)$$

Hence, as the plates move close to each other, i.e. when, the gap between the electrodes decreases the capacitance of the structure increases. On the other hand, when the gap between the electrodes increases, the capacitance of the structure decreases. To obtain a large change in capacitance, either the initial distance between the plates should be very small or the plates should move very close to each other. However, when the plates move very close to each other, the surface interaction and electrostatic attraction forces dominate the movement of the plates making them stick together i.e. pull-in takes place. Even though mechanical stops can be included to avoid pull-in, it is very difficult to design them without compromising the capacitance of the device [25].

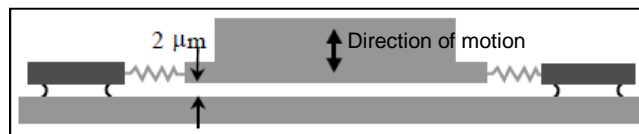


Fig. 2.3. Out-of-plane gap closing electrostatic converter [25]. (Reprinted with permission).

#### 2.4.2. In-plane gap closing converter [35]

As the name suggests, the motion of the proof mass, in the case of an in-plane gap closing converter, is on the plane of the wafer. An inter-digitated comb structure is typically used to achieve better capacitance values [34], as shown in Fig. 2.4 [35]. The gap between the two fingers is changed to achieve the change in capacitance.

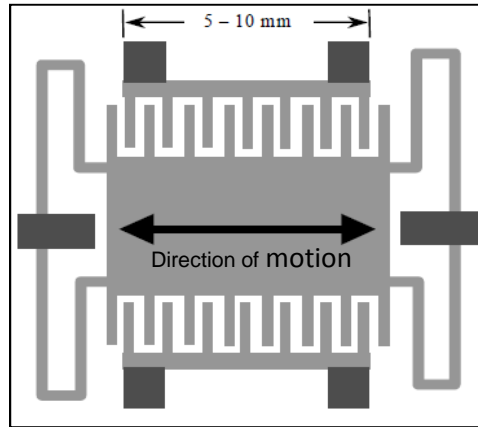


Fig. 2.4. In-plane gap closing electrostatic converter [35]. (Reprinted with permission).

For the schematic given in Fig. 2.4, the capacitance of the device can be represented as a parallel connection of several inter-digital capacitances, as given by [35]:

$$C_v = N_g \epsilon_0 L_f h_f \frac{2d}{(d^2 - z^2)} \quad (2.21)$$

where,  $C_v$  is the capacitance of the structure,  $N_g$  is the number of gaps formed due to the inter-digitated fingers,  $L_f$  is the effective length of the fingers,  $h_f$  is the thickness of the fingers,  $d$  is the initial gap between the fingers, while  $z$  is the deflection of flexures [35]. The capacitance is directly proportional to the effective length, the thickness of the fingers and to the number of gaps and the initial distance between the fingers. Hence, to achieve a large capacitance with inter-digitated combs, large structures with high aspect ratios of fingers are desirable [34].

Another representation of similar topology, where the gap between the electrodes is changed was given by I.Gonenli et al. [4], shown in the Fig. 2.5.

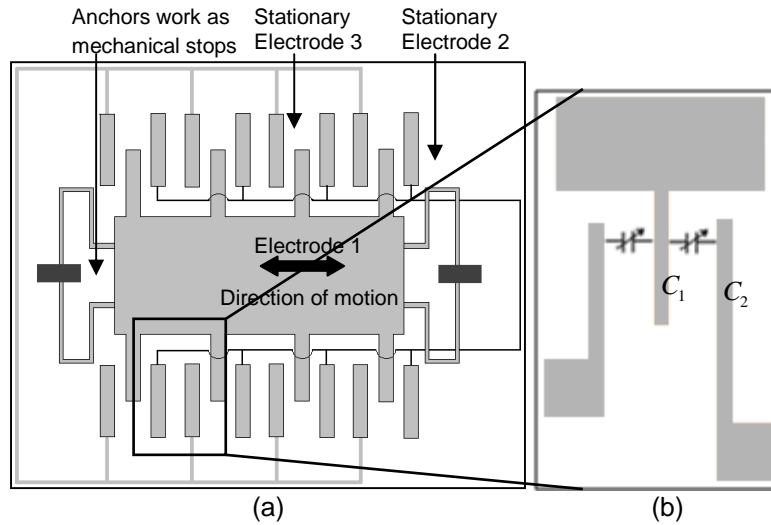


Fig. 2.5. (a) The schematic of an in-plane gap closing type accelerometer, redrawn as per the designed by I.Gonenli et al. [4] (Redrawn with permission) and (b) the two capacitances  $C_1$  and  $C_2$  between the combs of the structure.

The accelerometer devices were designed such that the stationary electrodes (electrode2 and electrode3 in Fig. 2.5), could be connected either in parallel, or in a differential form. The differential capacitance of the device is given by the difference between the capacitance of the adjacent inter-digitated fingers:

$$C_{vd} = N_g \epsilon_0 L_f h_f \frac{2z}{(d^2 - z^2)} \quad (2.22)$$

where,  $C_{vd}$  is the differential capacitance of the device. For the differential connection of the electrodes, the capacitance is directly proportional to the deflection of flexures along with the length and the thickness of the flexures.

#### 2.4.3. In-plane overlap converter [25]

For an in-plane overlap type of converter, the proof mass moves in the plane of the wafer and the overlap area between the inter-digitated fingers is changed, as shown in Fig. 2.6 [25].

The capacitance of the structure is then:

$$C_v = N_g \epsilon_0 L_f h_f \frac{(z + z_0)}{d} \quad (2.23)$$

where,  $z_0$  is the initial overlap distance of the inter-digitated fingers and  $z$  is the deflection of flexures, while  $d$  is the gap between the two fingers.

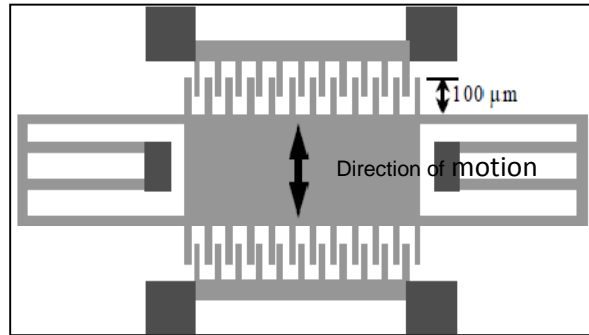


Fig. 2.6. In-plane overlap electrostatic converter [25]. (Reprinted with permission).

For an in-plane overlap and an in-plane gap closing topology, it is easier to provide mechanical stops to avoid pull-in between the two fingers [25].

## 2.5 Summary

The theory of the charge constrained and the voltage constrained conversion-cycles, which are implemented for the vibration-to-electricity conversion, were discussed along with the most commonly used device schematics.

Since, the change in the capacitance of the structure depends largely on the device structure; the basic three types of device topologies were studied. Two of the topologies were observed to implement the in-plane motion, while the third topology used out-of-plane motion, to obtain the change in capacitance. However, the in-plane topology was observed to be preferred most of the time [25, 35], because of the ease of implementation of the mechanical stops, which are inevitable to avoid the pull-in in case of an electrostatic energy harvester [22].

## CHAPTER 3

### DESIGN OF NOVEL ELECTROSTATIC MEMS ENERGY HARVESTER

#### 3.1 Introduction

The motivation behind working on the energy harvesters was to exploit the electrostatic-accelerometer devices designed by I.Gonenli et.al [4] as the electrostatic energy harvesters and to design and simulate additional structures. The schematics of the x-y sensing and the z-sensing accelerometers are similar to those of in-plane gap closing and out-of-plane gap closing type converters, respectively. Even though, the former accelerometers were designed as sensors, it was hypothesized that a few design modifications could transform the devices into the energy harvesters. The initial studies on the accelerometer devices and the subsequent designs of the new energy harvesters are discussed in this chapter.

#### 3.2 Accelerometer devices as energy harvesters

The accelerometer devices, designed by I.Gonenli et.al are shown in Figs. 3.1 and 3.2 [4]. While speculating the energy outputs for the accelerometer devices, no modifications were made to the device layouts and the device dimensions, except for the change in the gap between the electrodes, as in the case of the z-sensing devices.

An accelerometer device is also a damped mass-spring system, which was discussed in Chapter 1. The electrostatic accelerometers use the change in the capacitance as a measuring parameter to read the change in the displacement of the proof mass. As the proof mass moves, the distance between the electrodes changes and the work is done against the damping forces namely, the fluid and the electrostatic damping force. The work done can then be translated into the electrostatic energy, as discussed in Chapter 2.



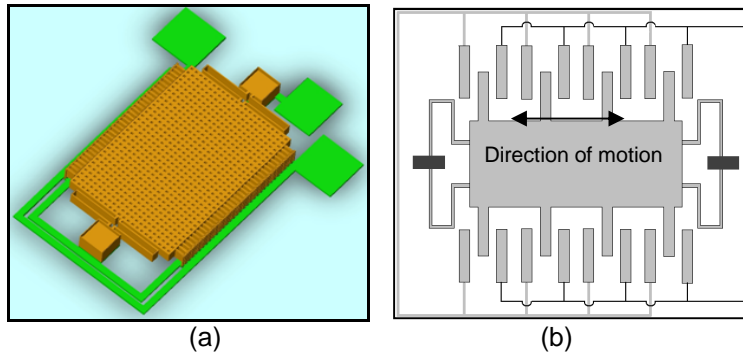


Fig. 3.1. Similarity between x-y sensing and in-plane gap closing converter schematic (a) 3D model of x-y\_accelerometer\_1605 device [4] (Reprinted with permission) (b) Redrawn schematic of the accelerometer device x-y\_accelerometer\_1605 device [4].

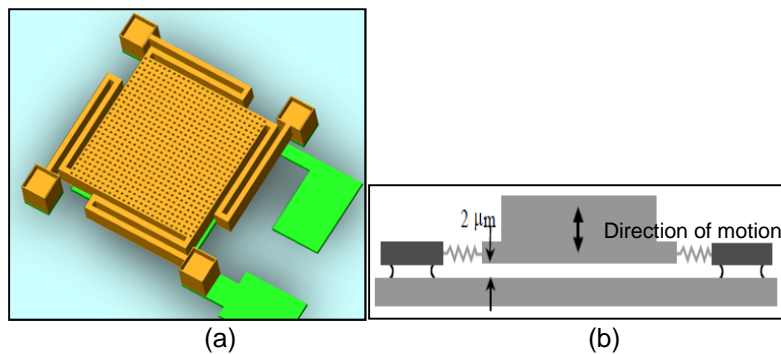
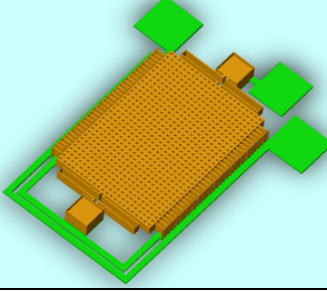
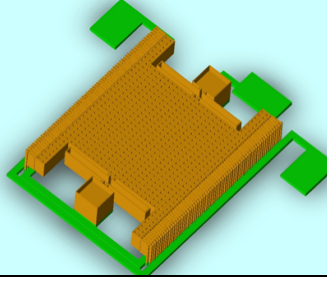
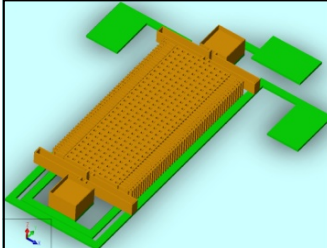


Fig. 3.2. Similarity between z- sensing and out-of-plane gap closing converter schematic (a) 3D model of z\_accelerometer\_650 device [4] (b) Out-of-plane gap closing schematic [25]. (Reprinted with permission).

### 3.2.1 X-Y sensing accelerometer devices

I.Gonenli et al. designed and fabricated three device models [4], (shown in Table 3.1) for the x-y sensing accelerometer. The proof mass was supported by two springs and had an interdigitated comb structure, which provided differential capacitance. The devices differed in the mass and the number of combs.

Table 3.1. x-y sensing accelerometer device models designed by I. Gonenli [4].

Device	Dimensions	3D models (Reprinted with permission)
x-y_accelerometer_1605	Proof mass:(1605 X 1281) $\mu\text{m}^2$ including the comb lengths Number of combs : 66 Effective comb length : 81 $\mu\text{m}$	
x-y_accelerometer_1900	Proof mass:(1900 X 1338) $\mu\text{m}^2$ including the comb lengths Number of combs : 128 Effective comb length : 64 $\mu\text{m}$	
x-y_accelerometer_1500	Proof mass:(1500 X 632) $\mu\text{m}^2$ including the comb lengths Number of combs : 100 Effective comb length : 61 $\mu\text{m}$	

The fluid damping was reported to be a major concern while designing the accelerometer devices [4]. Since the fluid damping affects the displacement of the proofmass, the damping ratios were reportedly optimized.

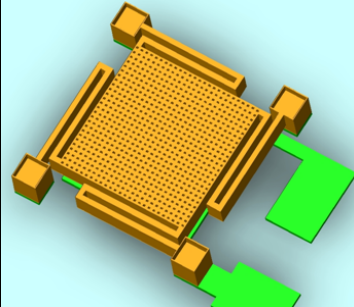
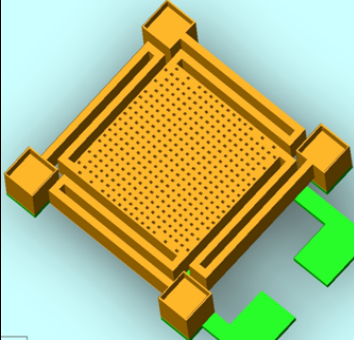
The sensitivity of the accelerometer is based on the displacement of the proof mass [4]. The displacements for the lateral sensing devices were obtained using MemMechMM module of the CoventorWare™. While simulating the devices for the displacement, an acceleration of 1g ( $g = 9.8 \text{ m/s}^2$ ) was applied in the direction of sensing. An acceleration of 1g was also applied in the negative z-direction, which represented the weight of the device acting downwards due to the earth's gravity.

To calculate the capacitance of the device, CoSolveMM module of CoventorWare™ was used. In this module, a potential difference of 1 V was applied across the device such that the proofmass was at the potential of 1 V, while the stationary electrodes were at 0 V. In addition, a virtual acceleration of 1g was applied in the lateral as well as the negative z-directions. The CoSolveMM couples the MEMMech and MEMElectro modules and calculates the effect of acceleration as well as voltage on the device. The simulated results are discussed in detail in Chapter 4.

### 3.2.2 Z-sensing accelerometers

Apart from x-y sensing accelerometers, I.Gonenli et al. had also designed two device models for z-sensing accelerometer, as shown in Table 3.2. The change in capacitance was achieved by moving the top electrode with respect to a stationary bottom electrode. Thus the z-sensing accelerometer devices resemble the out-of-plane converters.

Table 3.2. z- sensing accelerometer models designed by I. Gonenli [4].

Device	Dimensions	3D models (Reprinted with permission)
z_accelerometer_650	Proof mass : (650X 650) $\mu\text{m}^2$	
z_accelerometer_500	Proof mass: (500X 500) $\mu\text{m}^2$	

The proof mass was a plate supported by four springs on the four corners. In case of the z-sensing devices, only the squeeze film damping was reported to be a major concern. The squeeze film damping is predominantly observed in the structures where a plate, which is separated from the fixed surface by an air gap, moves towards the surface. This is because of a pressure that is developed in the air gap and it forces the air out of the gap. This air film poses a resistance to the motion of the plate and hence, acts as a damper [4]. The slide film damping was neglected because the device was designed to move predominantly in the out-of-plane with respect to the plane of the wafer. In addition, the aspect ratio of the devices was reportedly too high for the slide film damping to affect the motion of the device in the z-direction [4]. The damping, in case of z-sensing devices was optimized by changing the number and the size of perforation on the proof mass [4].

The displacement values were obtained for the z-sensing devices for the varied acceleration values applied in the negative z-direction. An acceleration of the range of 1g to 2g, gave the displacement of the order of  $10^{-2}$   $\mu\text{m/g}$ .

As per Eqs. (2.13) and (2.17), derived for electrostatic energy, the harvested energy is directly proportional to the change in the capacitance of the device. To get a significant change in the capacitance, the displacement of the proofmass with respect to its rest position should be high. However, the deflection of top electrode was observed to be very small as compared to the initial gap. Hence, the electrostatic energy generated was estimated to be less than the significant. In order to make the displacement comparable to the initial gap between the electrodes, the gap itself was reduced from 2.0  $\mu\text{m}$  to 1.2  $\mu\text{m}$ , and the effect on displacement as well as device capacitance was studied using CoSolveMM, while virtually applying 1 V between the top and the bottom electrodes.

Apart from the displacement and capacitance analysis, pull-in analysis was also performed on the z-sensing accelerometers. The pull-in voltage obtained for the devices with initial gap of 1.2  $\mu\text{m}$  was in the range of 1.24 V, which is very close to the applied voltage itself. Hence, it was important to increase the range of the pull-in voltage of the device. In order to

increase the pull-in tolerance of the device, mechanical stops were introduced in the design as shown in Fig. 3.3.

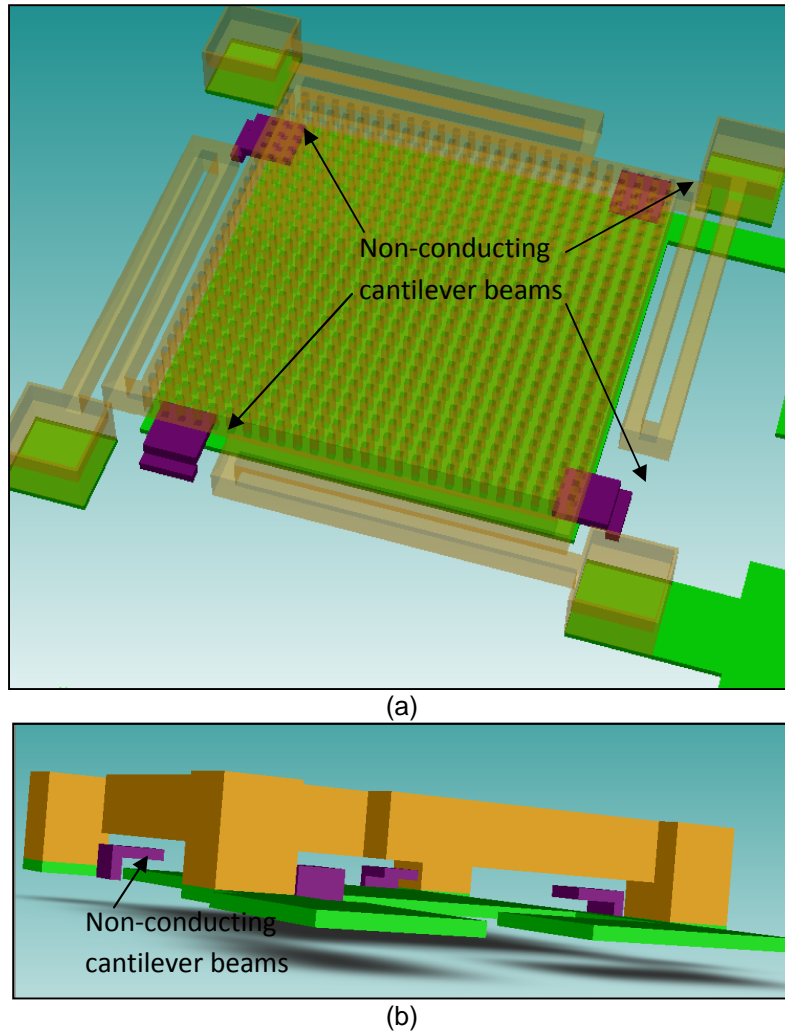


Fig. 3.3. 3D model for  $z\_accelerometer\_650$  device with cantilevers (a) Top view of device1 with top electrode with 75% transparency showing tips of cantilever beams inserted between the top and bottom electrodes (b) Side view of  $z\_accelerometer\_650$ , showing electrical isolation of cantilever beams.

The tips of the electrically isolated cantilever beams were inserted between the top and the bottom electrode [39]. When z-acceleration is applied to the device, the springs with a spring constant of  $k_1$ , attached to the top electrode move down taking the top electrode towards the bottom electrode. While the plate is moving down, it encounters the cantilever beams, with the

spring constant of  $k_2$ . Once the top plate touches the cantilever beams, the beams carry the top plate towards the bottom plate. However, they prevent the top plate from collapsing into the bottom plate. The spring constant of the cantilever beams and the springs attached to the proof mass come in parallel with each other, thus increasing the total spring constant to  $(k_1 + k_2)$  and reducing the movement of the top plate [39].

However, even if the cantilevers would help avoid the pull-in, the total capacitance of the device is reduced because the active area contributing towards the capacitance is reduced. This is mainly because the non-conducting cantilevers beams are inserted between the two electrodes. While designing an electrostatic energy harvester, it is not reasonable to insert the mechanical stops at an expense of the capacitance.

### 3.3 Design of novel energy harvesters

The data obtained for the accelerometer devices showed that the devices have prominent sensing abilities however, are not capable of producing adequate power outputs. Hence, an attempt was made to design a novel electrostatic energy harvester. An effort was made, to utilize all the three dimensions of device space, to achieve decent power outputs at realistic acceleration of the order of 1g.

#### 3.3.1 Concept of cubic capacitive device

In a typical variable capacitive device, either the area or the gap between the surfaces of the two electrodes is changed. In case of the out-of-plane type of schematic, only one capacitance changes at a time when the gap between the electrodes is changed. In order to get higher change in capacitance, an inter-digitated finger type of structure is used, where a number of fingers of a stationary electrode are placed between the fingers of moving electrode. Consider a finger of a stationary electrode is placed between the two fingers of a moving electrode, as shown in the Fig. 3.4 (b). In this case, only two capacitances namely,  $C_1$  and  $C_2$ , are changed simultaneously, when either the overlap area or the gap between the fingers is changed.

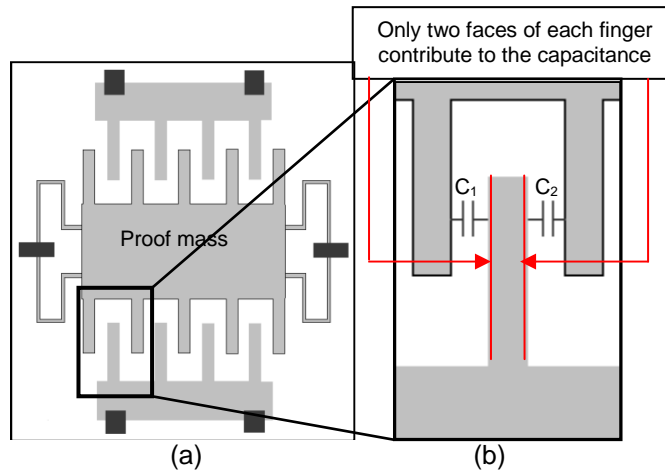


Fig. 3.4. Illustration of the inter-digited capacitance contributed by two side faces of a finger (a) A schematic of an in-plane gap closing type of electrostatic device (b) Inset showing the individual capacitance contributed by a set of fingers of a stationary and a moving electrode.

Thus, only the two side faces of each finger of stationary electrode, contribute to the capacitance. Hence, for  $n$  number of fingers, the rest capacitance of the inter-digitated capacitive structure is given by [4]:

$$C = 2n\epsilon_0 \frac{A}{d} \quad (3.1)$$

where,  $A$  is the overlap area of each finger and  $d$  is the gap between the two adjacent fingers. However, the top and the bottom surfaces can also be used to obtain the capacitance, if a counter electrode is present for the top as well as for the bottom surface. This idea was exploited while designing the energy harvester devices.

Fig. 3.5 shows a hollow cubic structure with a cubic block shaped electrode inserted in it. If potential difference is applied across these two structures, capacitance is generated between the inner surfaces of the hollow cube and the outer surfaces of the cubic electrode. If the inner electrode is displaced with respect to the hollow cubic electrode, the four overlapping areas are changed at the same time. Thus, a single rectangular electrode contributes four capacitances simultaneously.

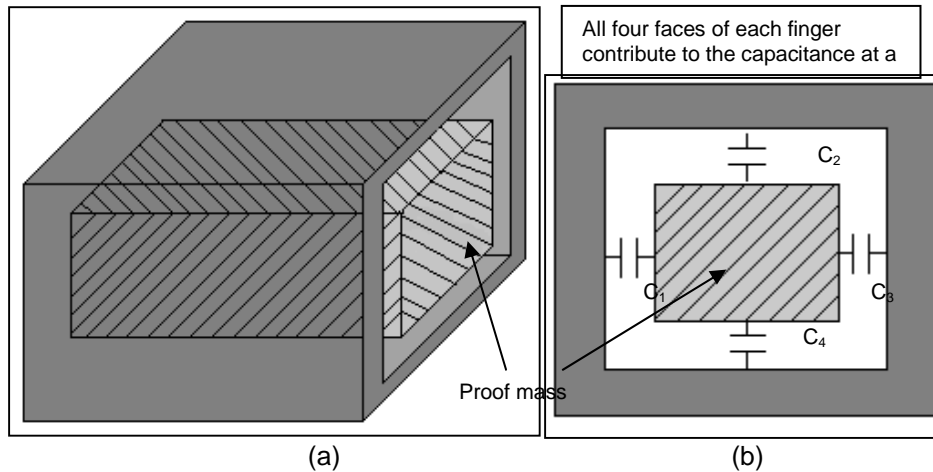


Fig. 3.5. Conceptual model of cubic capacitance (a) Schematic showing an electrode inserted inside a hollow cubic enclosure (b) side view of the schematic showing capacitance contributed by all four faces of the electrode that is inserted in the hollow cubic enclosure.

If an array of  $n$  such fingers inserted in the cubic structure is used, the capacitance of the structure is given as:

$$C = 4n\epsilon_0 \frac{A}{d} \quad (3.2)$$

Thus, with the same number of fingers, it is possible to acquire twice more the capacitance as compared to a simple inter-digitated capacitive structure.

### 3.3.2 Design parameters

#### 3.3.2.1 Device Dimensions

The energy harvester devices were designed taking into consideration the acceleration provided by an aircraft, which is in the range of  $9.8 \text{ m/s}^2$  at the frequency of 100 Hz [40, 41]. The designs were aimed at obtaining a high capacitance, large displacement and a large change in the capacitance.

The basic structure of the proposed devices is shown in Fig. 3.6 and had

- a. a proof mass supported by four springs
- b. an array of movable hollow cubic structures attached to the top-surface of the proof mass



- c. stationary cantilever beam electrodes and
- d. mechanical stops.

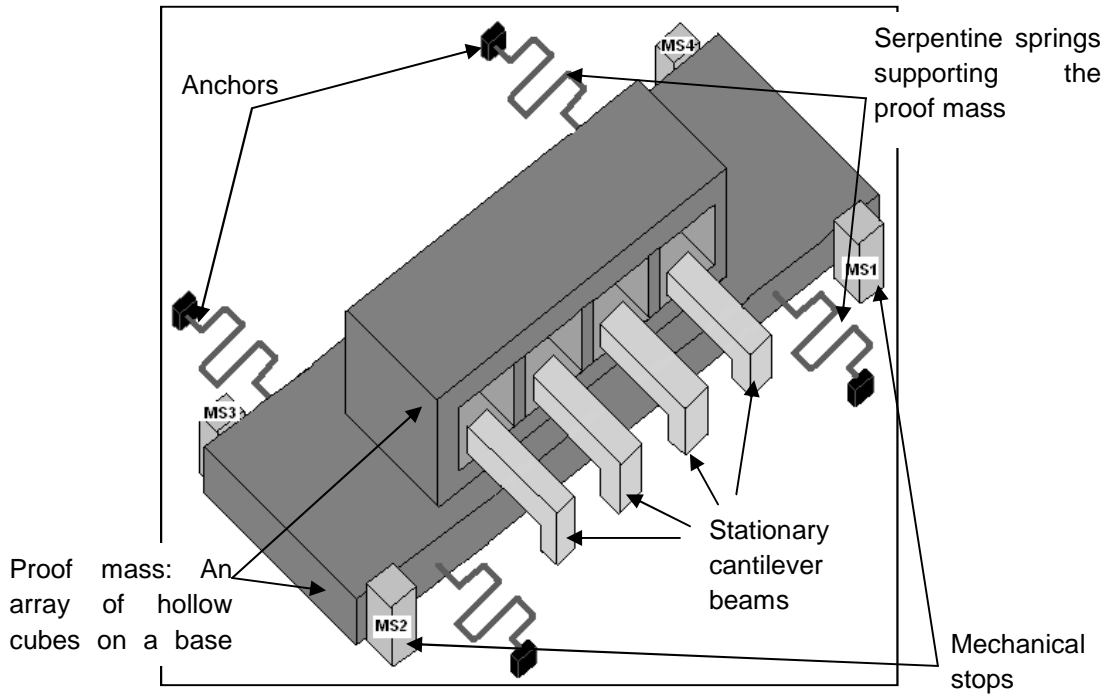


Fig. 3.6. A basic structure of novel energy harvester (not to the scale) showing stationary cantilever beams inserted in the hollow cubic proof mass (contact pads are not shown).

The dimensions of the proofmass and the springs were chosen such that the entire device is constrained within an area of  $(2000 \times 2000) \mu\text{m}^2$ .

The array of cubic enclosure and the base electrode together constituted the proofmass of the device. At the rest position, the cantilever beams were inserted in the cubic structure. Since the devices were designed for the displacement of  $15 \mu\text{m}$ , the overlap area of the cantilever beams and the cubic enclosure was set to  $17 \mu\text{m}$  for all the device models, so that there was an overlap of  $2 \mu\text{m}$  after the displacement of the proofmass, which would ensure the alignment of the cantilever beams with their respective hollow cubic enclosures. However, the overlap area of the cantilever beams and the base electrode was varied for each device model. The cubic structure was designed to move to and fro with respect to the cantilever beams. Thus relatively, the cantilever beams moved in and out of the cubic structure. Hence, the change in capacitance

was only due to the change in the overlap area of the cubic structure and the cantilever beams.

The mechanical stop MS1 and MS2 were used to avoid the contact between the proofmass and the stationary cantilever beams. In addition, the mechanical stops MS3 and MS4 were used to restrict the movement of the device beyond 15  $\mu\text{m}$  in the negative  $x$  direction with respect to the rest position of the proof mass, so that the alignment, of the cantilever beams and their respective hollow cubes, is ensured. In order to obtain a displacement of 15  $\mu\text{m}$ , the springs were designed as discussed in Section 3.3.2.2.

### 3.3.2.2. Spring design

The springs were designed to obtain a displacement of 15  $\mu\text{m}$ , for which the maximum change in capacitance was estimated, as shown in Table 3.3. The relation between the spring constant and the proofmass is given by [4, 37]:

$$\omega = \sqrt{\frac{k}{m}} \quad (3.3)$$

$$k = \frac{m \times a}{x} \quad (3.4)$$

where,  $\omega$  is the resonant frequency of the device,  $k$  is the spring constant of the flexures,  $m$  is the mass and  $a$  is the source acceleration. For a nickel proofmass of the volume of  $(2000 \times 500 \times 50) \mu\text{m}^3$  and the acceleration of  $9.8 \text{ m/s}^2$ , the estimated spring constants for the different displacements are shown in Table 3.3. In addition, the Table 3.3 also gives an estimated change in capacitance of a device with fifty modules of the hollow cubes and the cantilever beams. The capacitance of each module is calculated using Eq. (3.2), where  $n$  is 50 and area  $A$  is varied as shown in Table 3.3.

Table 3.3. Estimated spring constants for different displacements and the relative change in capacitance of a device

$x$ ( $\mu\text{m}$ )	$k$ (N/m)	Effective area $A$ ( $\mu\text{m}$ ) <sup>2</sup> of capacitance of each module when the device is at rest	Rest capacitance $C_{\text{max}}$ (fF)	Capacitance after the displacement of $x$ ( $\mu\text{m}$ ), $C_{\text{min}}$ (fF)	Change in capacitance $\Delta C$ (fF)
5	0.045	$(7 \times 10)$	24.791	7.0832	17.707

Table 3.3 - Continued

8	0.0281	(10 × 10)	35.416	7.0832	28.332
10	0.0225	(12 × 10)	42.499	7.0832	35.415
12	0.0187	(14 × 10)	49.582	7.0832	42.498
15	0.0150	(17 × 10)	60.207	7.0832	53.1238

From Table 3.3, it is observed that for a desired displacement of 15 μm, the spring constant as low as 0.015 N/m is required. To obtain such a low spring constant, series connection of U-shaped springs was used. Eqs. (3.5) and (3.6) [4] give the equivalent spring constant of the springs connected in the parallel and the series combination, respectively:



Fig. 3.7. The spring combinations (a) parallel spring combination (b) series spring combination.

$$k_{eq} = k_1 + k_2 \quad (3.5)$$

$$\frac{1}{k_{eq}} = \frac{1}{k_1} + \frac{1}{k_2} \quad (3.6)$$

where,  $k_1$  and  $k_2$  are the spring constants of the two springs respectively, while  $k_{eq}$  is the equivalent spring constant. From the above equations it is clear that the spring constant of the overall structure decreases if the springs are connected in series. Hence, the U-shaped springs were connected in series to form a serpentine spring structure, as shown in Fig. 3.8. (b). A basic unit of the U-shaped spring is shown in Fig. 3.8 (a).

On the other hand, the lateral and vertical spring constants of a u-shaped spring are given by [4]:

$$k_l = \frac{Yhw^3}{2l^3} \quad (3.7)$$

$$k_v = \frac{Ywh^3}{2l^3} \quad (3.8)$$

respectively, where,  $Y$  is the Young's modulus of the material,  $h$  is the thickness of the spring,  $w$  is the width, while  $l$  is the length of the spring [4]. The springs were designed so that the spring constant in the lateral direction was lower than that of the vertical spring constant. Hence, the ratio of lateral to vertical spring constant, given by Eq. (3.9), was considered for the spring design.

$$\frac{k_l}{k_v} = \left(\frac{w}{h}\right)^2 \quad (3.9)$$

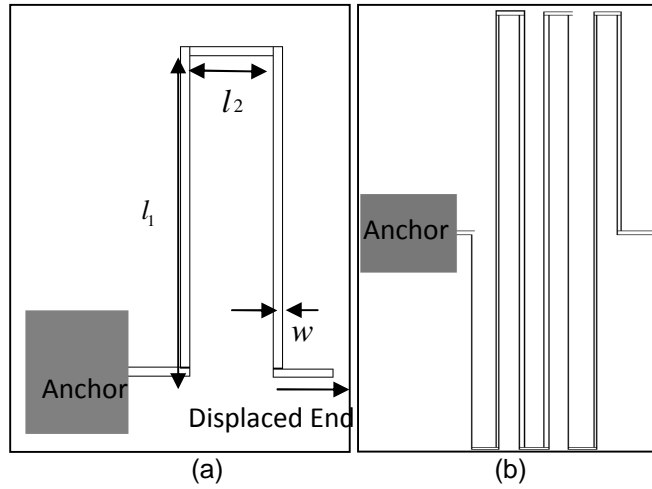
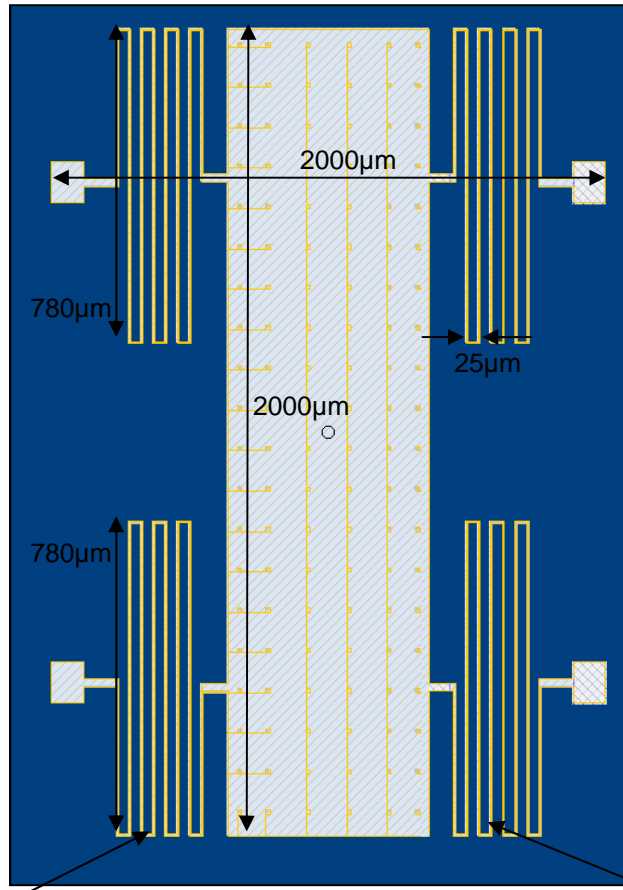


Fig. 3.8. Spring design (a) A unit-cell of a U-shaped spring (b) A series connection of 7 U-shaped springs, forming one serpentine spring.

A total of two serpentine springs, shown in Fig. 3.8 (b) each, were required to be connected in parallel, on each side of the proofmass, as shown in Fig. 3.9. It was important to place the springs symmetrically along the proofmass to avoid the wobble. Hence, the length of each U-shaped spring was chosen such that the serpentine springs are placed within the constrained area of  $(2000 \times 2000) \mu\text{m}^2$ . At the same time, it was important to obtain a maximum length of the springs, in order to decrease the lateral spring constant, as per Eq. (3.7). Hence, initially the length  $l_1$  was chosen as  $400 \mu\text{m}$ , such that the total length of one meander is  $800 \mu\text{m}$  and two serpentine springs could be placed symmetrically along the proofmass. However, from Table 3.4, it is clear that the springs with  $l_1$  of  $400 \mu\text{m}$  showed comparatively lower lateral as well as vertical spring constants. Hence, the length  $l_1$  was reduced to  $390 \mu\text{m}$ . The length  $l_2$  was set to  $25 \mu\text{m}$  in order to adjust seven such meanders of the springs (discussed in detail in Chapter 4).



Two serpentine springs connected in parallel, on each side of the proof mass.

Fig. 3.9. A layout of an energy harvester device, showing the dimensions of the proofmass and the serpentine springs.

The spring constant of a single U-shaped spring was calculated for different combinations of the length  $l_1$ , thickness  $h$  and width  $w$ , as shown in Table 3.4. In addition, Table 3.4 shows the displacement of the proofmass in the lateral as well as vertical direction. These displacements were calculated using the Eq. (3.4) such that the displacement in the vertical direction is calculated using the vertical spring constant  $k_v$  and the displacement in the lateral direction is calculated using the lateral spring constant  $k_l$ , at an acceleration of  $9.8 \text{ m/s}^2$ .

Table 3.4. The estimated spring constants for different spring thickness, width and the spring lengths

$h$ ( $\mu\text{m}$ )	$l_1$ ( $\mu\text{m}$ )	$l_2$ ( $\mu\text{m}$ )	$w$ ( $\mu\text{m}$ )	Young's modulus for electroplated Nickel, $E$ (GPa) [42]	$k_l$ (N/m)	$k_v$ (N/m)	Displacement in the lateral direction ( $\mu\text{m}$ )	Displacement in the z-direction ( $\mu\text{m}$ )
35	400	25	8	100	14.00	267.996	0.0160	$0.849 \times 10^{-3}$
	400	25	5	100	3.417	167.480	0.0658	$1.343 \times 10^{-3}$
35	390	25	8	100	15.104	289.113	0.0141	$0.778 \times 10^{-3}$
	390	25	5	100	3.687	180.694	0.0610	$1.245 \times 10^{-3}$
25	390	25	8	100	10.789	105.362	0.0208	$2.135 \times 10^{-3}$
	390	25	5	100	2.6340	65.8515	0.0854	$3.416 \times 10^{-3}$

Table 3.4 showed that the springs with higher aspect ratio have higher vertical spring constants, which is desirable to restrict the out-of-plane movement of the proofmass. However, the fabrication of the high aspect ratio springs, using the MEMS fabrication techniques, can be challenging. Hence, a series combination of seven U-shaped springs, each of the width 5  $\mu\text{m}$ , length  $l_1$  of 390  $\mu\text{m}$ , length  $l_2$  of 25  $\mu\text{m}$  and thickness of 25  $\mu\text{m}$ , was adjusted within the area constrained to  $(2000 \times 2000) \mu\text{m}^2$ . For such a series combination of seven U-shaped springs, equivalent spring constant of 0.3762 N/m was calculated. Since, the calculated spring constant was more than the desired spring constant, more source acceleration was required, in order to achieve the displacement of 15  $\mu\text{m}$ . Hence, while performing the FEA simulations, an acceleration of  $15\text{m/s}^2$  was applied instead of  $9.8 \text{m/s}^2$ .

The spring module of CoventorWare™ was used to determine the simulated spring constant. While performing the spring simulations, one end of the spring was anchored while the other end was displaced by 15  $\mu\text{m}$ . The spring constant was calculated by dividing the reaction force, obtained from the simulation results, by the displacement of the spring. The simulation results are discussed in Chapter 4.

### 3.3.3. Energy harvester device models

Three different energy harvester models were designed by varying the dimensions of the cantilever beams and the dimensions of the cubic enclosure. The nomenclature used for each model shows the model number, the width of the cubic enclosure and the length of the cantilever beams, for example Model1\_500CL35 refers to the first energy harvester model, having a cubic enclosure of the width 500  $\mu\text{m}$  and the cantilever beams of length 35  $\mu\text{m}$ . Each of the device models are discussed in detail here.

#### 3.3.3.1. Energy harvester Model1\_500CL35

The first model, Model1\_500CL35 of the energy harvesters had the cantilever beams of the dimensions of  $(35 \times 10 \times 10) \mu\text{m}^3$ . A total of 46 such cantilever beams were adjusted along the length of the proofmass. The array of the hollow cubic structure was attached to a proofmass of the dimensions of  $(500 \times 2000 \times 10) \mu\text{m}^3$ . Each hollow cube had the inner dimensions of  $(500 \times 20 \times 20) \mu\text{m}^3$  and the outer dimensions of  $(500 \times 30 \times 25) \mu\text{m}^3$ , with the sidewall of the thickness of 20  $\mu\text{m}$ . At the rest position, every cantilever beam contributed a capacitance, which was due to the overlap area of  $(17 \times 10) \mu\text{m}^2$  between the cubic structure and the cantilever beam. Fig. 3.10 illustrates the device model with the different 3D views.

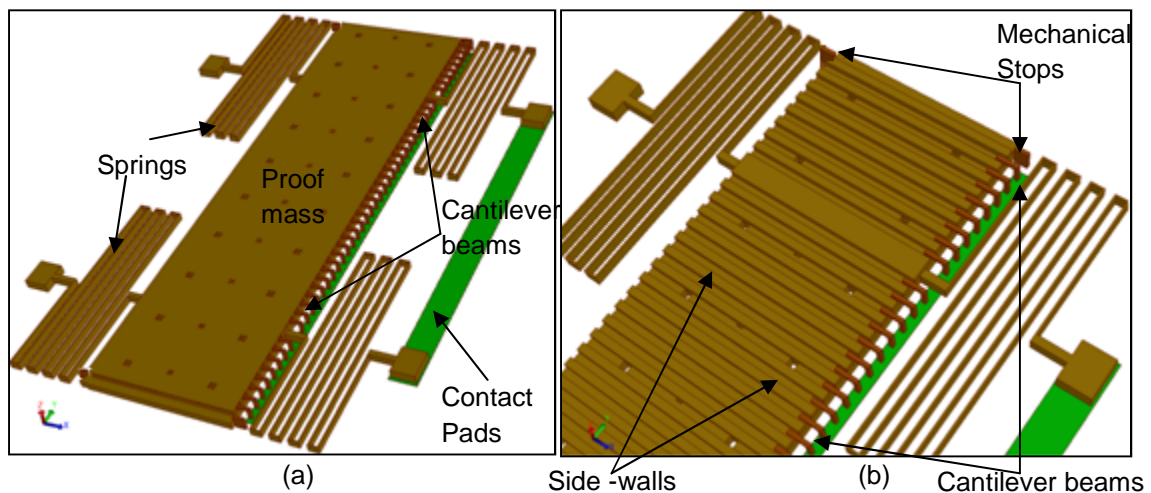


Fig. 3.10. Model1\_500CL35 (a) 3D view of the model in CoventorWare™, (b) A 3D view of the model showing the cantilever beams. The top plate of the cubic enclosure is not shown.

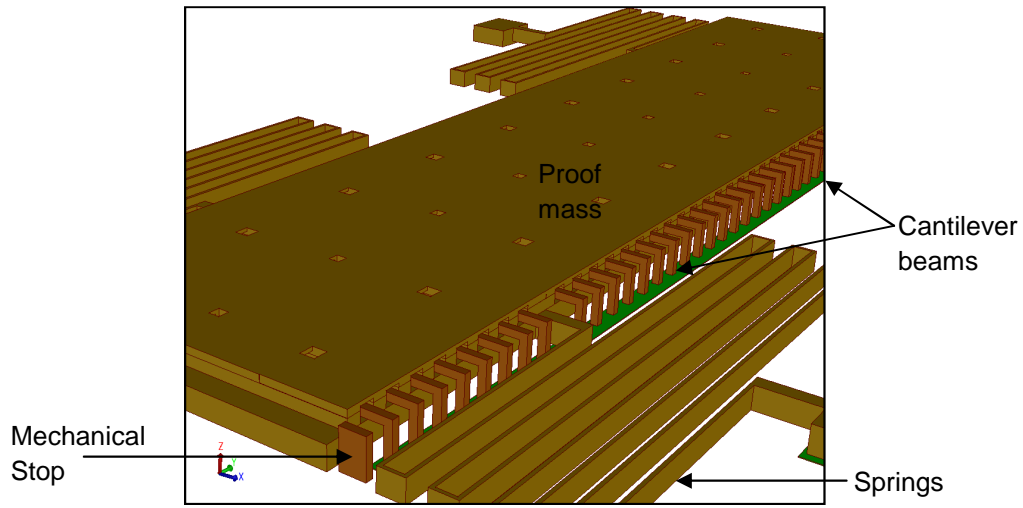


Fig. 3.11. Another view of the 3D model showing the cantilever beams and the mechanical stop of Model1\_500CL35.

### 3.3.3.2. Energy harvester Model2\_24CL287

Fig. 3.12 shows the Model2\_24CL287. In this model, the width of the cubic structure was reduced to  $24\mu\text{m}$ . The cubic structure was placed along the center of the base electrode of the dimensions of  $(500 \times 2000 \times 10) \mu\text{m}^3$ , such that, the weight of proofmass is balanced along its line of symmetry. The train of 28 hollow cubic structures had each cube with the inner dimensions of  $(24 \times 64 \times 20) \mu\text{m}^3$  and the outer dimensions of  $(30 \times 69 \times 25) \mu\text{m}^3$ , with a sidewall of the thickness of  $5 \mu\text{m}$  each. The cantilevers had the dimensions of  $(287 \times 54 \times 10) \mu\text{m}^3$ . The overlap area of each cantilever beam and the proofmass was increased to  $(257 \times 54) \mu\text{m}^2$ . This increase in the overlap area increased the rest capacitance of the structure.



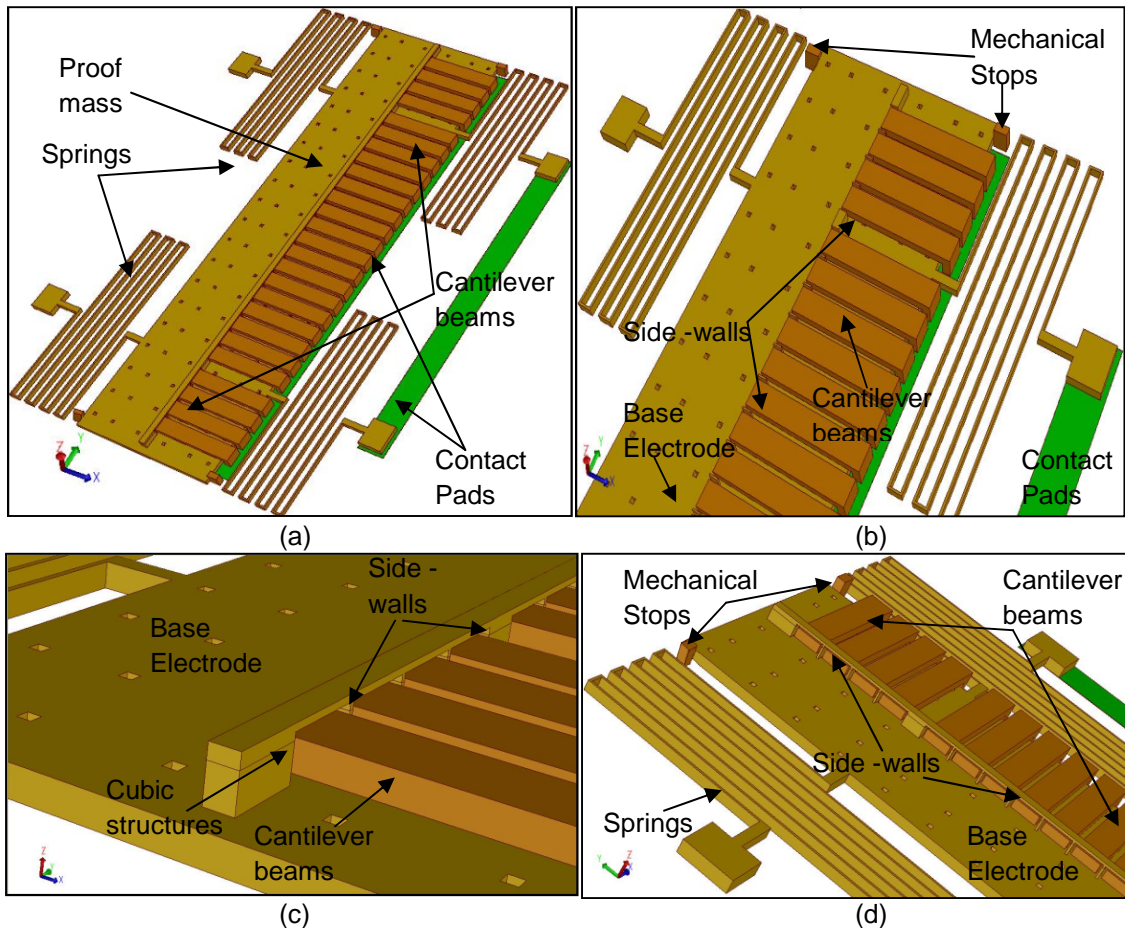


Fig. 3.12. Model2\_24CL287 (a) 3D view of the model in CoventorWare™, (b) A 3D view of the model showing the cantilever beams. The top plate of the cubic enclosure is not shown. (c) and (d) Another view of the 3D model showing the cantilever beams and the mechanical stop.

### 3.3.3.3. Energy harvester Model3\_200CL203

In case of Model2\_24CL287, the cubic structure was too small to contribute to the total mass of the proofmass. Hence, the device showed small displacements as compared to Model1\_500CL35. However, in Model3\_200CL203, the width of the cubic structure was increased to increase the volume of cubic structure. The inner dimensions of each cube were  $(200 \times 15 \times 20) \mu\text{m}^3$  and outer dimensions of  $(200 \times 20 \times 25) \mu\text{m}^3$ , with each sidewall of the thickness of  $5 \mu\text{m}$ . A total of 120 such hollow cubes were adjusted along the length of the proofmass.

From the Eq. (3.2), the capacitance of the structure increases with increasing number of cantilever beams. However, in order to increase the number of beams, the width of the cantilevers has to be reduced to  $5\ \mu\text{m}$  to keep the overall dimensions the same. This resulted in long, thin and fragile cantilever beams. Hence, the cantilever beams were attached to the cantilever-plates, as shown in Fig. 3.13. The dimensions of each cantilever beam were  $(22 \times 5 \times 10)\ \mu\text{m}^3$ . The dimension of two of the smaller cantilever plates named Cantilever-Plates\_305, as shown in Fig. 3.13. (a), were  $(181 \times 305)\ \mu\text{m}^2$ . The larger plate named Cantilever-Plate\_1205, had the dimensions of  $(181 \times 1205)\ \mu\text{m}^2$ . The cantilever-plates were used mainly to provide support to the cantilever beams. In addition, the plates increased the rest capacitance of the structure, which in turn contributed to the overall energy of the device.

The simulation results obtained for Model3\_200CL203 showed an increase in the amount of displacement and in the change in capacitance.

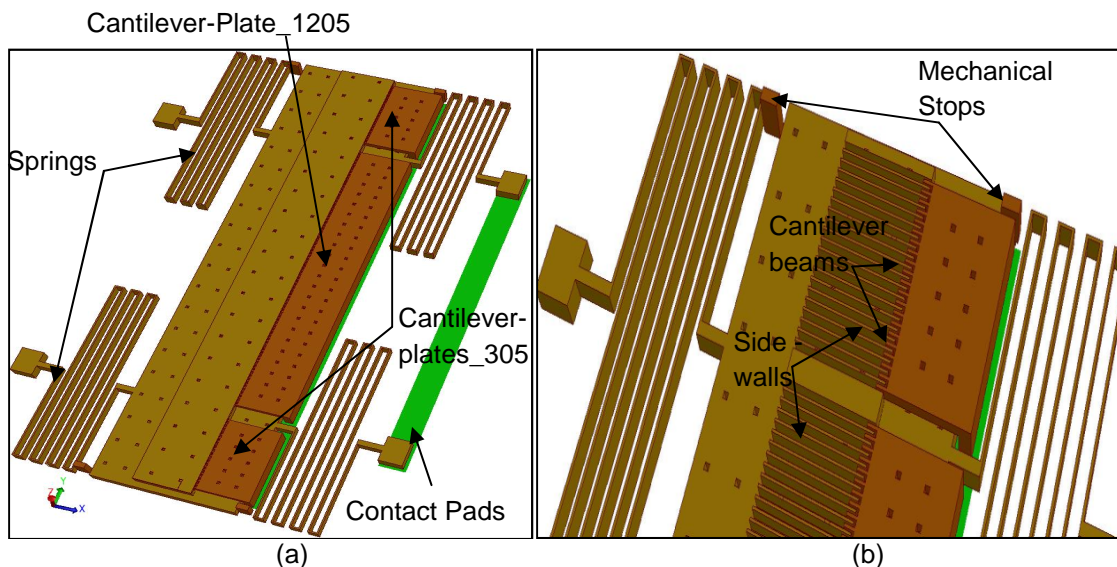


Fig. 3.13. Model3\_200CL203 (a) 3D view of the model in CoventorWare™ (b) A 3D view of the model showing the cantilever beams. The top plate of the cubic enclosure is not shown.

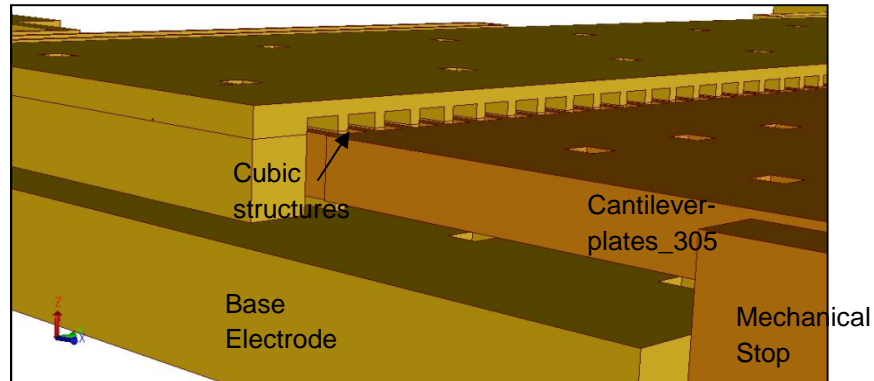


Fig. 3.14. Another view of the Model3\_200CL203 showing the cantilever beams and the mechanical stop.

All the energy harvester devices were designed such that the silicon real estate is utilized optimally. Fig. 3.15 shows all the rest capacitance present in the device.

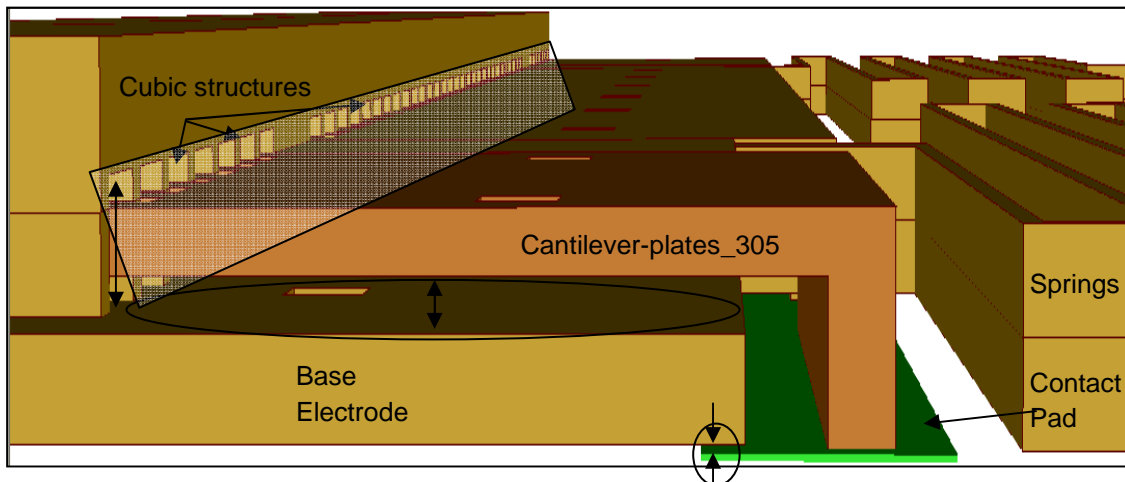


Fig. 3.15. Illustration of various rest capacitances in case of Model3\_200CL203. The double-sided arrows indicate the sites of the capacitance (the mechanical stop is not shown in the figure).

From the Fig. 3.15, the observed capacitances were:

1. between the cubic enclosure and the cantilever beams
2. between the base electrode of the proofmass and the cantilever beams, and
3. between the base electrode and the contact pads of the cantilever beams. The overlap between the contact pads and the base electrode of the proofmass was set to  $10\mu\text{m}$  for all the device models.

When the proof mass was displaced, all the capacitances changed simultaneously and provided a considerable change in the total capacitance of the device.

A comparative account of the dimensions of all the models of the new energy harvester devices is given in Table 3.5. The proposed fabrication process and the related challenges are discussed in the following sections.

#### 3.3.4. Fabrication Challenges

All the energy harvester devices had a major challenge of fabricating the cantilever beams that are inserted in the hollow cubic structures. The device fabrication was proposed to be carried out on two wafers, such that the contact pads, the base electrode, cantilever beams and the side walls of the hollow cubes are fabricated on Wafer1, using the UV-LIGA [43, 44] process. However, the top covering-plate, which covered the side-walls to form the hollow cubes, was proposed to be fabricated on another wafer, Wafer2. A eutectic bonding technique [45, 46] was then proposed to be used for bonding the top layer (on Wafer2) to the side-walls fabricated on the base electrode (on Wafer1). These processes are discussed in detail in Section 3.3.6. However, prior to determining the final fabrication process-flow, the limitations of the fabrication process were taken into consideration. The fabrication was found to be challenging because of the following reasons:

1. Patterning of thick photoresist mold for the proofmass with the base electrode of the desired thickness of 35  $\mu\text{m}$ , with desired aspect ratio of 7:1.
2. The width of side walls should be insufficient to achieve a reliable bond between the top and the base plates of the proofmass.

It is possible to achieve the patterning of a photoresist of the thickness as high as 100-500  $\mu\text{m}$  with aspect ratios of 20-50, as in case of a negative photoresist such as SU-8 [44, 47]. However, it is not possible to achieve a good pattern unless the photolithography process is supported by the deep x-ray lithography. However, some facilities, for example, Metal-MUMPS™ can be used to realize the high aspect ratio electroplating of nickel. Metal-MUMPS was introduced by MEMSCAP in 2003. The maximum thickness of electroplated nickel reported by

MEMSCAP™ was 20 - 22  $\mu\text{m}$  [48]. In case of bonding of the top covering-plate to the sidewalls on the base electrode, it would be challenging to achieve precise alignment of the sidewalls of the width as small as 5  $\mu\text{m}$  [45, 46]. Hence, a few modifications to the designed models were proposed in the Section 3.3.6.

### 3.3.5. Modifications to the design models due to the fabrication constraints

To avoid the above discussed fabrication challenges, the device designs were modified. As discussed previously, the thickness of the base electrode was taken as 25  $\mu\text{m}$  and that of the top covering-plate was 5  $\mu\text{m}$ . Hence, as per the design, the total thickness of the proof mass was 50  $\mu\text{m}$  (25  $\mu\text{m}$  thick base electrode + 20  $\mu\text{m}$  thick sidewalls + 5  $\mu\text{m}$  thick top covering-plate). To avoid the patterning of a thick photoresist mold for the electroplating of 25  $\mu\text{m}$  thick base electrode, the thickness of the base electrode was reduced to 15  $\mu\text{m}$ , while the thickness of the top cover of the cubic enclosure was increased to 15  $\mu\text{m}$ . Thus, the proofmass of a total thickness of 50  $\mu\text{m}$  (15  $\mu\text{m}$  thick base electrode + 20  $\mu\text{m}$  thick sidewalls + 15  $\mu\text{m}$  thick top covering-plate) could be achieved. However, by decreasing the thickness of the base electrode, the thickness of the attached spring also decreased to 15  $\mu\text{m}$ , which would decrease the vertical spring constant. Hence, to achieve a minimum thickness of 25  $\mu\text{m}$ , the spring deposition was proposed to be done in two steps: first with the deposition of the base electrode and second, with the deposition of the sidewalls of the cubic enclosure.

For the Model1\_500CL35, the modifications were required only in terms of the thickness of the device. However, in case of Model2\_24CL287 and Model3\_200CL203, the width of the side walls was increased to 10  $\mu\text{m}$ , along with the change in the thickness of the base electrode and the top cover of the cubic enclosure. In addition to this, in case of the Model3\_200CL203, the cantilever width was modified to 10  $\mu\text{m}$ , in order to study the effect of change of finger widths on the capacitance of the structure. The modified model of Model2\_24CL287 is referred as Model2\_24CL287.a, while the modified models of Model3\_200CL203 are referred as Model3\_200CL203.a and Model200CL203.b where, Model3\_200CL203.a refers to the design

with the cantilever beam width of 5  $\mu\text{m}$  and Model3\_200CL203.b refers to the design with the cantilever beam width of 10  $\mu\text{m}$ . The modifications are shown in the Figs. 3.16 - 3.18.

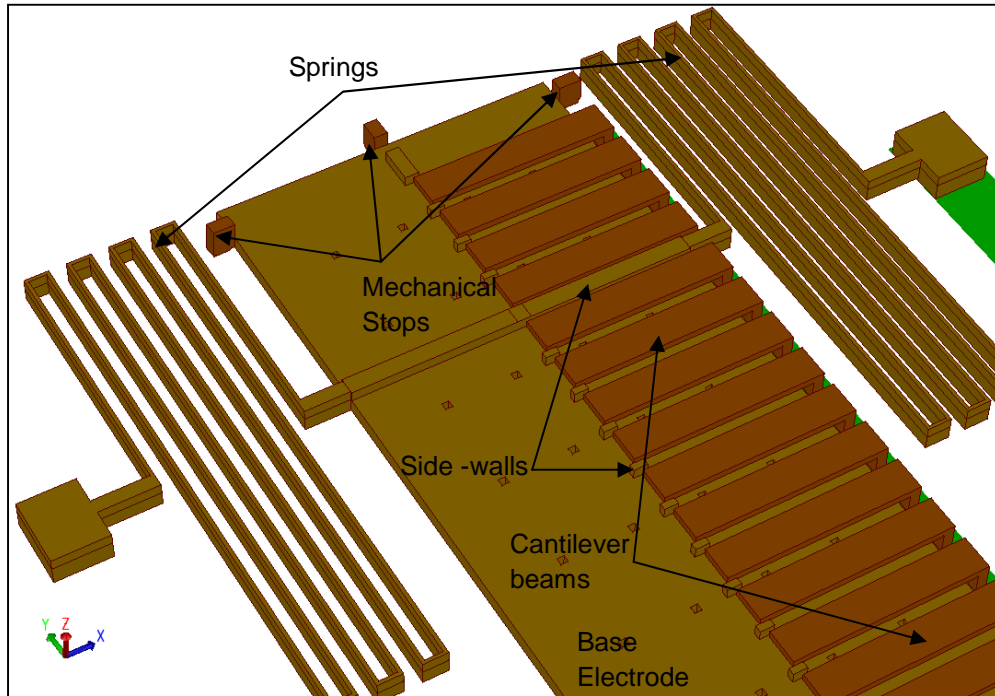


Fig. 3.16. Model2\_24CL287.a: The modifications made to the Model2\_24CL287, where the cantilever beam width is 50  $\mu\text{m}$  and the width of the side-walls is 10  $\mu\text{m}$ .

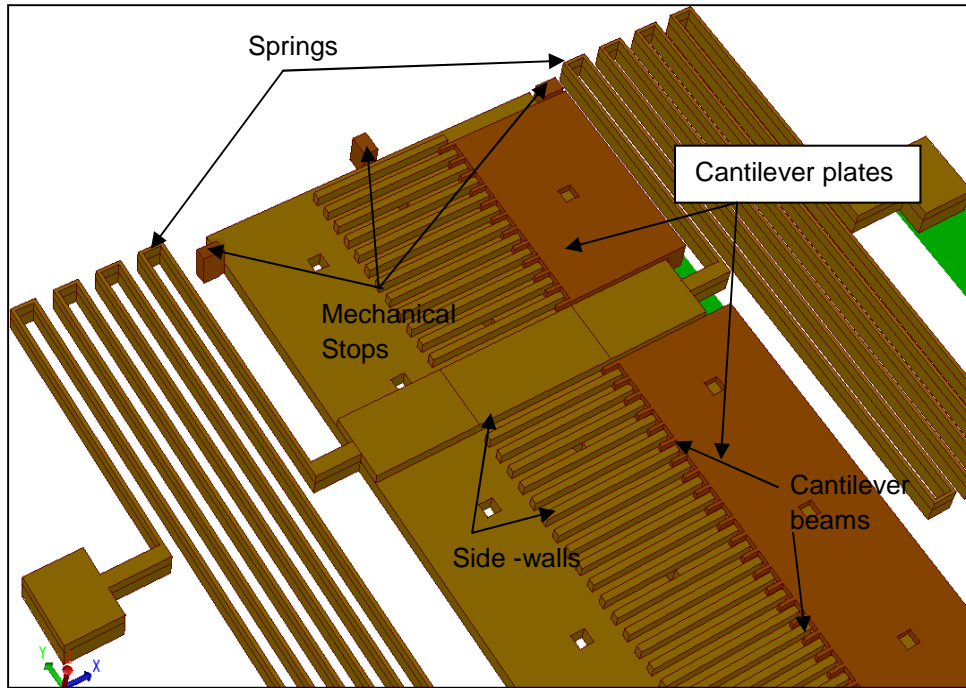


Fig. 3.17. Model3\_200CL203.a: The modifications made to the Model3\_200CL203, where the cantilever beam width is maintained at 5  $\mu\text{m}$ .

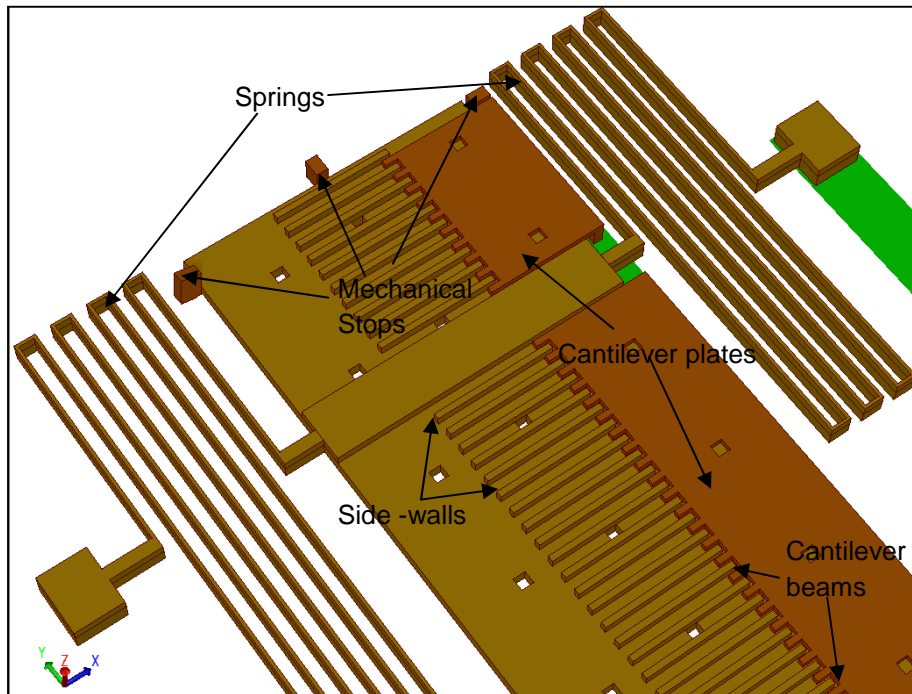


Fig. 3.18. Model3\_200CL203.b: The modifications made to Model3\_200CL203, where cantilever beam width is changed to 10  $\mu\text{m}$ .

Table 3.5 gives a comparative account of the dimensions of all the models of the new energy harvester devices along with the modified models.

Table 3.5. The dimensions of all the energy harvester models along with the dimensions of their modified models.

Device	Dimensions of the base electrode ( $\mu\text{m}^3$ )	Dimensions of the top plate ( $\mu\text{m}^3$ )	Dimensions of the cantilever beams ( $\mu\text{m}^3$ )	Dimensions of each side-wall ( $\mu\text{m}^3$ )
Model1_500CL35 (unmodified)	(500 × 2000 × 25)	(500 × 2000 × 5)	(35 × 10 × 10)	(10 × 20 × 10)
Model1_500CL35.a (modified model)	(500 × 2000 × 15)	(500 × 2000 × 15)	(35 × 10 × 10)	(10 × 20 × 10)
Model2_24CL287 (unmodified)	(500 × 2000 × 25)	(30 × 2000 × 5)	(287 × 54 × 10)	(10 × 5 × 10)
Model2_24CL287.a (modified model)	(500 × 2000 × 15)	(30 × 2000 × 15)	(287 × 54 × 10)	(10 × 10 × 10)
Model3_200CL203 (unmodified)	(500 × 2000 × 25)	(200 × 2000 × 5)	(22 × 5 × 10)	(10 × 5 × 10)
Model3_200CL203.a (modified model)	(500 × 2000 × 15)	(200 × 2000 × 15)	(22 × 5 × 10)	(10 × 10 × 10)
Model3_200CL203.b (modified model)	(500 × 2000 × 15)	(200 × 2000 × 15)	(22 × 10 × 10)	(10 × 10 × 10)

### 3.3.6. Proposed process flow

A generalized process flow for the energy harvester devices is proposed in the Table 3.6. The modified device Model3\_200CL203.a is taken into consideration. All the images shown below are taken from the 3D model built in the CoventorWare™ and are exaggerated by 5 times in the z-direction in order to view the thicknesses of the layers.



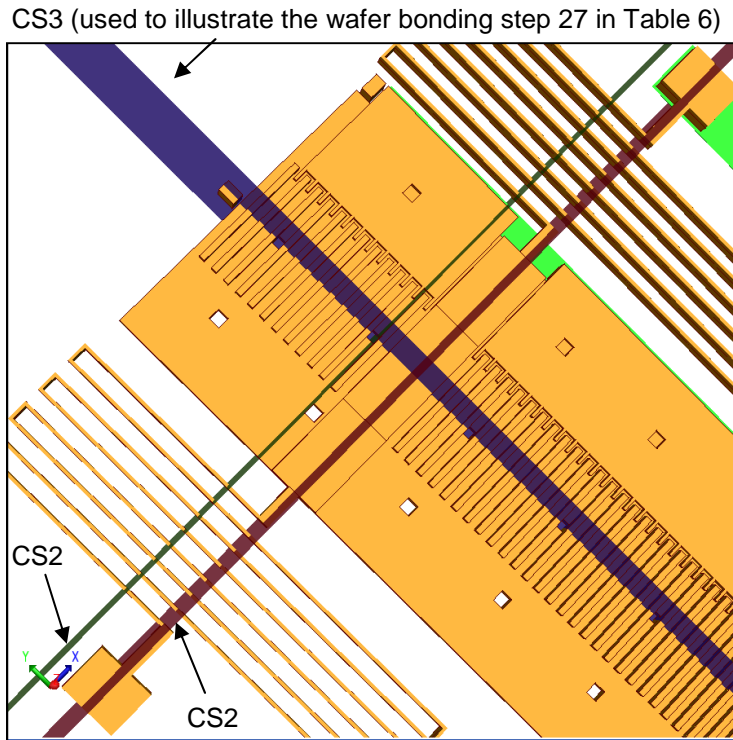


Fig. 3.19. The modified Model3\_200CL203.a, with sidewall width 10  $\mu\text{m}$  and cantilever beams width 5  $\mu\text{m}$ . (The top layer of the cubic enclosure is not seen in the figure).

In the above Fig. 3.19, the planes CS1, CS2 and CS3 are the cross-section planes for the cross-section1, cross-section2 and cross-section3, respectively.

Table 3.6. Proposed fabrication process flow

	Step	Cross-section1 (CS1)	Cross-section2 (CS2)
1	Layer Name: Nitride Passivation layer. Process Step: Sputter deposit and pattern. Thickness : 1 $\mu\text{m}$ Material : Nitride Comments : Steps 1-18 are carried out on Wafer1	<p>View1</p>	
2	Layer Name: Contact Pads Process Step: Sputter deposit and pattern. Thickness : 1 $\mu\text{m}$ Material : Aluminum	<p>View 1</p> <p>View2</p>	<p>View1</p> <p>View2</p>

Table 3.6 - Continued


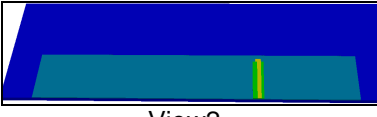






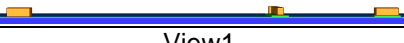


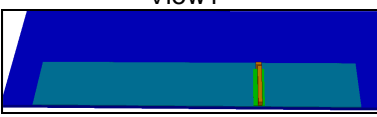


3	<p>Layer Name: Seed layer for anchors          Process Step: Sputter deposit and pattern.          Thickness : 0.1 <math>\mu\text{m}</math>          Material : Gold</p>	 <p style="text-align: center;">View2</p>	 <p style="text-align: center;">View2</p>
4	<p>Layer Name: Mold layer for anchors          Process Step: Spin Coat and pattern.          Thickness : 7 <math>\mu\text{m}</math>          Material : Polyimide</p>	 <p style="text-align: center;">View1</p>	 <p style="text-align: center;">View1</p>
5	<p>Layer Name: Electroplate#1 anchors          Process Step: Electroplate.          Thickness : 5 <math>\mu\text{m}</math>          Material :Nickel</p>	 <p style="text-align: center;">View1</p>  <p style="text-align: center;">View2</p>	 <p style="text-align: center;">View1</p>  <p style="text-align: center;">View2</p>
6	<p>Layer Name: Remove the mold layer          Process Step: Etching.          Material : Polyimide          Comments: Mold layer is removed since the thickness of mold layer is 7 <math>\mu\text{m}</math>, which is 2 <math>\mu\text{m}</math> more than the required sacrificial layer (deposited in next step) between the proofmass and the wafer</p>	 <p style="text-align: center;">View1</p>  <p style="text-align: center;">View2</p>	 <p style="text-align: center;">View1</p>  <p style="text-align: center;">View2</p>
7.	<p>Layer Name: Seed layer2 for Anchors          Process Steps: Sputter deposit and pattern.          Thickness: 0.1 <math>\mu\text{m}</math>          Material : Gold</p>	 <p style="text-align: center;">View2</p>	 <p style="text-align: center;">View2</p>

Table 3.6 - Continued

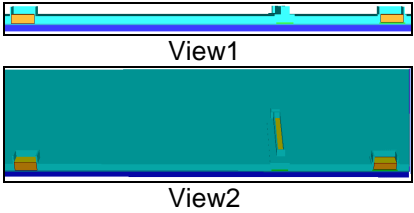
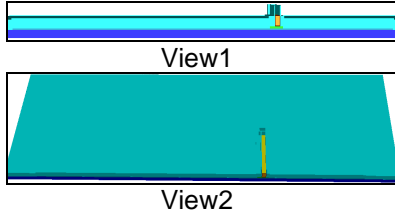
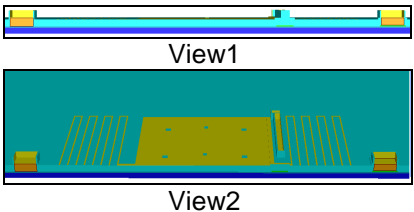
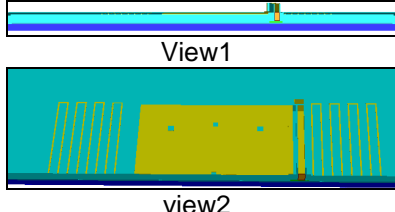
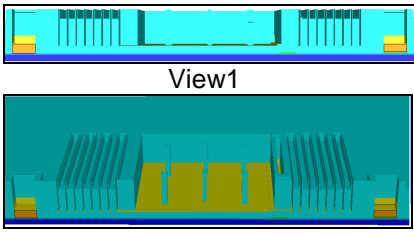
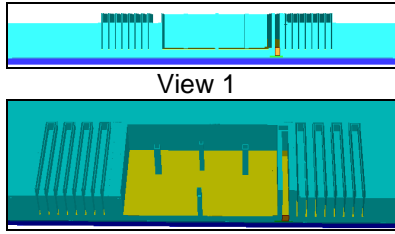
<p>8.</p>	<p>Layer Name: Sacrificial layer between base electrode (proofmass) and wafer          Process Step: Spin coat and pattern.          Thickness : 5 <math>\mu\text{m}</math>          Material : Polyimide</p>	 <p>View1</p> <p>View2</p>	 <p>View1</p> <p>View2</p>
<p>9.</p>	<p>Layer Name: Gold Seed layer for base electrode (proofmass)          Process Step: Sputter deposit and pattern.          Thickness : 0.1 <math>\mu\text{m}</math></p>	 <p>View1</p> <p>View2</p>	 <p>View1</p> <p>view2</p>
<p>10.</p>	<p>Layer Name: Mold layer for base electrode (proofmass)          Process Step: Spin coat and pattern.          Thickness : 17 <math>\mu\text{m}</math>          Material : Polyimide          Comments: The smallest feature size is of 5 <math>\mu\text{m}</math> (width of springs), such that the aspect ratio is 3.4:1.</p>	 <p>View1</p> <p>View2</p>	 <p>View 1</p> <p>View2</p>

Table 3.6 - Continued

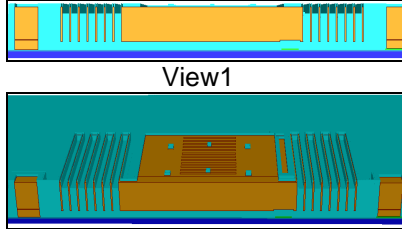
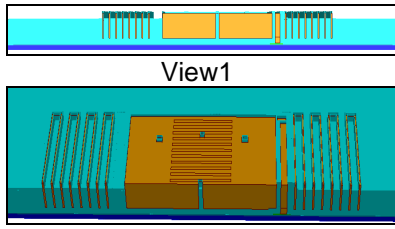
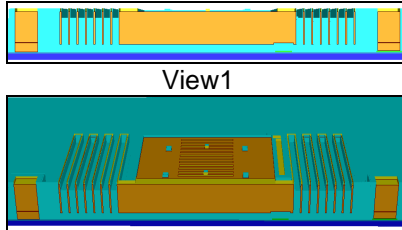
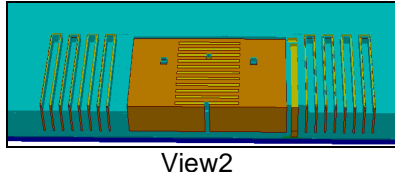
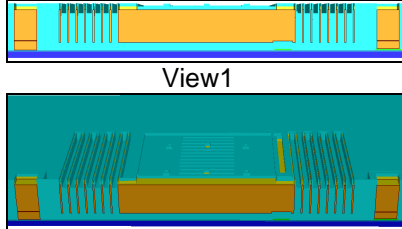
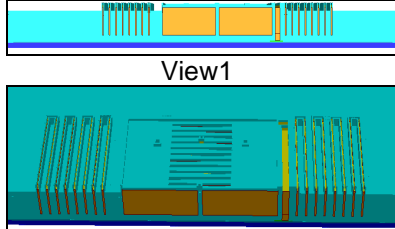
<p>11</p>	<p>Layer Name: Electroplate#2 base electrode Process Step: Electroplate. Thickness : 15<math>\mu</math>m Material : Nickel Comments: In the actual electroplating process, the thickness of electroplated metal is usually less than the thickness of the mold, unless an over-electroplating is intended [49]. Hence, because of these process limitations a residual mold of 2 <math>\mu</math>m resist is assumed to be present around the electroplated area in all the given electroplating process steps.</p>	 <p>View1</p> <p>View2</p>	 <p>View1</p> <p>View2</p>
<p>12</p>	<p>Layer Name: Seed layer for anchors of cantilevers, Springs and sidewalls. Process Step: Sputter deposit and pattern. Thickness : 0.1 <math>\mu</math>m Material : Gold</p>	 <p>View1</p> <p>View2</p>	 <p>View2</p>
<p>13</p>	<p>Layer Name: Sacrificial layer between the base electrode and the cantilever beams Process Step: Spin coat and pattern. Thickness : 3 <math>\mu</math>m Material : Polyimide</p>	 <p>View1</p> <p>View2</p>	 <p>View1</p> <p>View2</p>

Table 3.6 - Continued

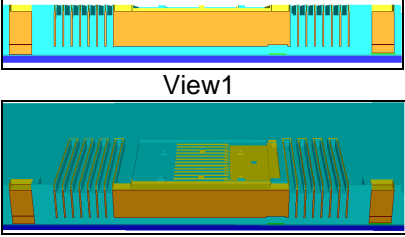
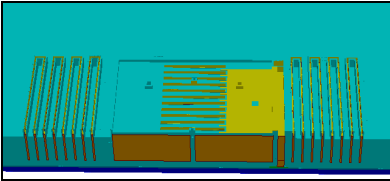
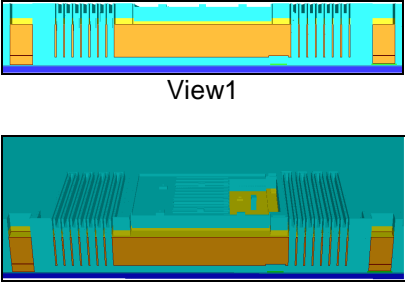
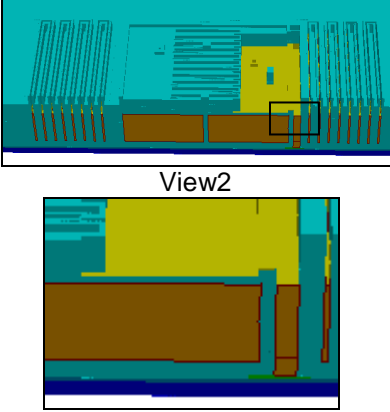
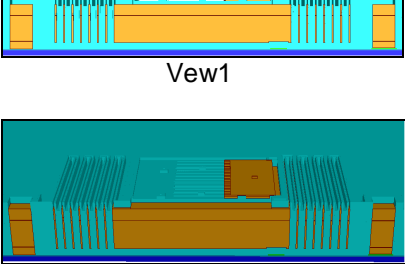
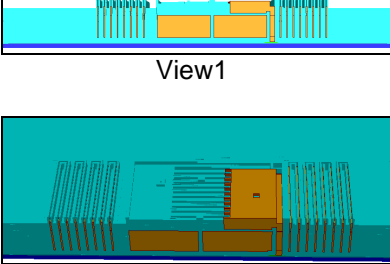
<p>14</p>	<p>Layer Name: Seed layer for side walls of cubes          Process Step: Sputter deposit and pattern.          Thickness : 0.1 <math>\mu\text{m}</math>          Material : Gold          Comments: Note the difference in the levels in the cantilever beam region.</p>	 <p>View1</p> <p>View2</p>	 <p>View2</p>
<p>15</p>	<p>Layer Name: Mold layer for cantilever, springs and side wall electroplating          Process Step: Spin coating and pattern.          Thickness : 10 <math>\mu\text{m}</math>          Material : Polyimide          Comments: 10 <math>\mu\text{m}</math> is spin coated on top of the 3 <math>\mu\text{m}</math> sacrificial polyimide layer spin coated in step 13, such that the total thickness is 13 <math>\mu\text{m}</math></p>	 <p>View1</p> <p>View2</p>	 <p>View2</p> <p>INSET for View2</p>
<p>16</p>	<p>Layer Name: Electroplate#3 side walls, cantilevers and springs          Process Step: Electroplate          Thickness : 10 <math>\mu\text{m}</math>          Material : Nickel</p>	 <p>View1</p> <p>View2</p>	 <p>View1</p> <p>View2</p>

Table 3.6 - Continued

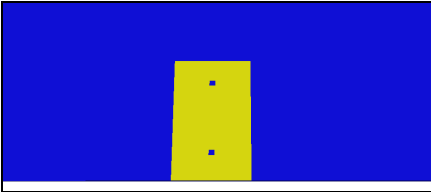
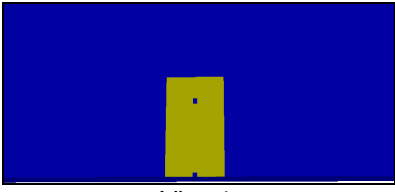

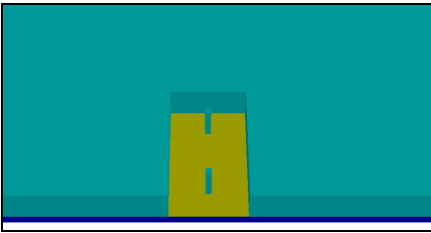

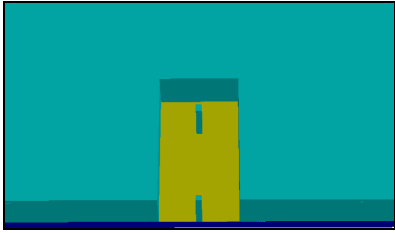

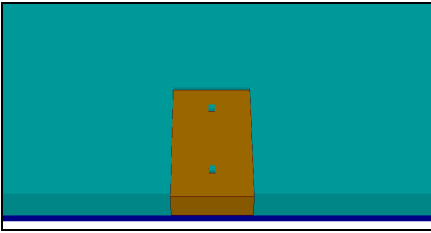

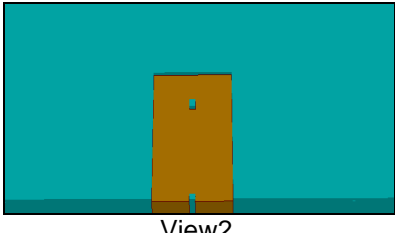
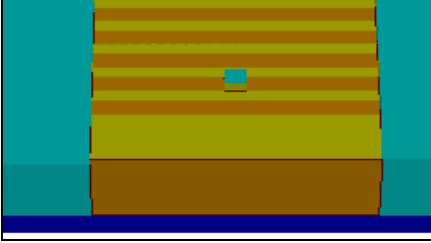
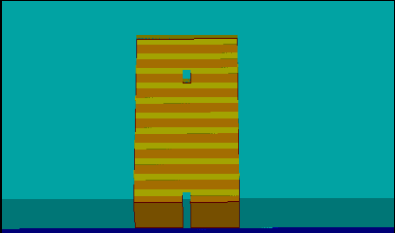
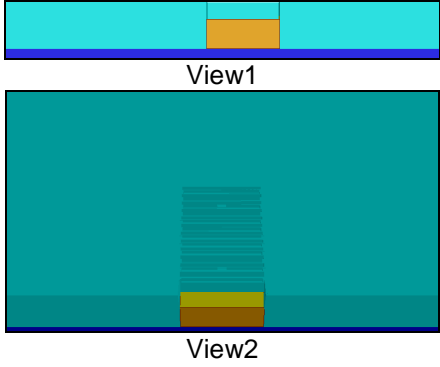
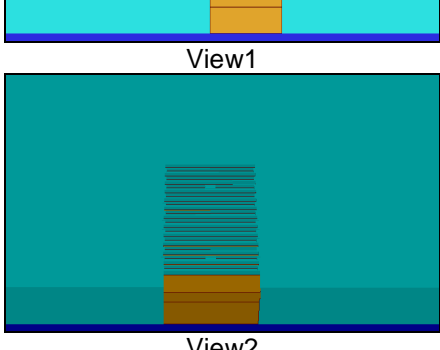
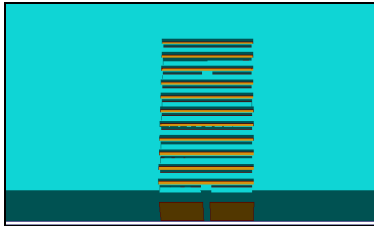
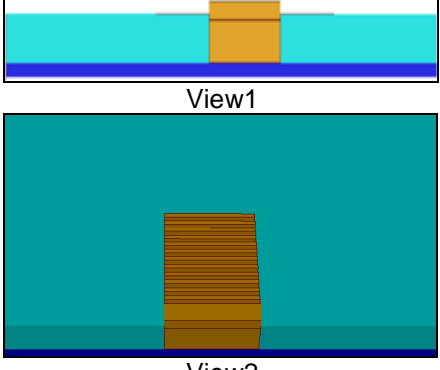
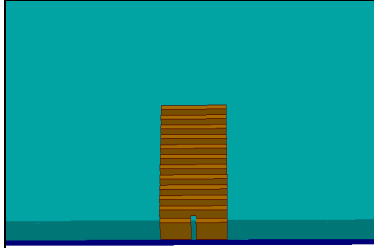
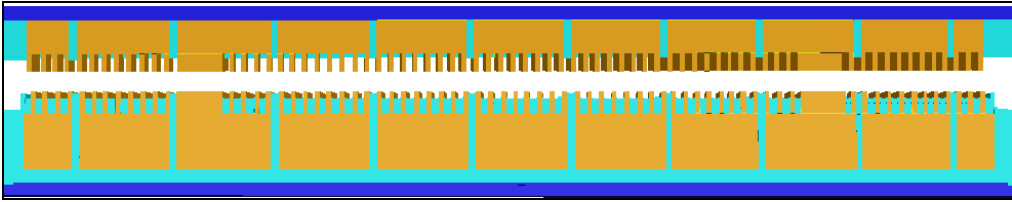
19	<p>The top layer of the cubic structure is proposed to be fabricated on Wafer2 and bonded to the side-walls , which are fabricated on the base electrode on Wafer1.</p>	
<p>20                  Layer Name:                  Seed layer for top layer of cubic structure                  Process Step:                  Sputter deposition and pattern                  Thickness : 0.1 <math>\mu\text{m}</math>                  Material : Gold                  Comments :                  Steps 20-26 are proposed on Wafer2</p>	 <p style="text-align: center;">View1</p>	 <p style="text-align: center;">View1</p>
<p>21                  Layer Name:                  Mold layer for the top layer                  Process Step:                  Spin coating and pattern                  Thickness : 17 <math>\mu\text{m}</math>                  Material :                  Polyimide</p>	 <p style="text-align: center;">View1</p>  <p style="text-align: center;">View2</p>	 <p style="text-align: center;">View1</p>  <p style="text-align: center;">View2</p>
<p>22                  Layer Name:                  Electroplate#5                  Top layer                  Process Step:                  Electroplate.                  Thickness :                  15<math>\mu\text{m}</math>                  Material :                  Nickel</p>	 <p style="text-align: center;">View1</p>  <p style="text-align: center;">View2</p>	 <p style="text-align: center;">View1</p>  <p style="text-align: center;">View2</p>
<p>23                  Layer Name:                  Seed Layer for sidewalls                  Process Step:                  Sputter coat and pattern.                  Thickness : 0.1 <math>\mu\text{m}</math></p>		

Table 3.6 - Continued

<p>24</p>	<p>Layer Name: Mold for sidewalls of the cubes. Process Step: Spin coat and pattern Thickness : 7 <math>\mu\text{m}</math> Material : Polyimide Comments: Sidewalls of the cubic structure are the primary bonding sites.</p>	 <p>View1</p> <p>View2</p>	
<p>25</p>	<p>Layer Name: Electroplate#6 Sidewalls of the cubes Process Step: Electroplate. Thickness : 5 <math>\mu\text{m}</math> Material : Nickel</p>	 <p>View1</p> <p>View2</p>	 <p>View2</p>
<p>26</p>	<p>Process Step: Etch and remove the mold layer to expose the bonding site i.e. side-walls</p>	 <p>View1</p> <p>View2</p>	 <p>View2</p>
<p>27</p>	<p>Face-to-face bonding of wafer1 and wafer2.</p>  <p>Wafer2</p> <p>Wafer1</p> <p>Figure shows the Wafer1 and Wafer2 along the cross-section CS3.</p>		

### 3.4. Summary

In this chapter, the motivation of designing a novel energy harvester is discussed. The short comings of exploiting the electrostatic accelerometers as the energy harvesters are elaborated on. The design of a novel energy harvester is presented along with the three variations made to the device design.

In addition, a fabrication process flow was proposed along with its possible limitations. However, a few modifications were also suggested in order to avoid those limitations.



## CHAPTER 4

### SIMULATIONS AND RESULTS

#### 4.1. Introduction

A finite element analysis (FEA) was performed to validate the calculated results, discussed in Chapter 3. In this Chapter, the simulations and the results are discussed in detail.

Each device was simulated to obtain displacement, capacitance and the resonant frequency. The MemMechMM, CoSolveMM and MemElectroMM modules of the CoventorWare™ software were used for these simulations. In addition, the SpringMM module was used to determine the spring constant of the designed springs, used for the new energy harvesters.

The simulation results were further utilized to calculate the energy and the power that can be harvested with the devices. A comparative account of the estimated output power is also given with respect to few electrostatic energy harvesters that have been reported by the various research groups.

#### 4.2. Mechanical analysis

Since the fabrication of a MEMS device is an expensive process, it is essential to validate its designs, before sending them to the fabrication. The finite element analysis (FEA) is a powerful tool used in the mechanical industry for structural, thermal and fluidic analyses of a device at the design level. In the present work, the CoventorWare™ simulation software was used to perform the FEA.

In FEA, a structure is broken down into small elements, with the help of a complex system of nodes and points, which form a mesh. Each of these small elements maintains a set of material properties, which are defined as per the material used for the structure. Depending upon

the boundary conditions and the direction of the applied load, the meshed structure responds to the load, resulting in a deformed mesh. This deformed mesh can also be utilized as the initial condition for the MemElectroMM solver. The response of each of the small elements is predicted on the basis of a set of equations, derived from the structural behavior. Integration of the behavior of all the elements, defines the response of the complete structure.

In this section, the simulations are outlined on the basis of the material properties, applied boundary conditions, meshing of the devices and the analysis setups.

#### 4.2.1. Accelerometers

The accelerometers designed by I.Gonenli et al. [4], were first analyzed for their possible application as the energy harvesting devices.

##### 4.2.1.1. Materials and Properties

The accelerometers designed by I.Gonenli et al. consisted mainly of the aluminum contact pads to which the metal electrodes made of nickel were attached. For the mechanical analysis of the devices, the elastic modulus and the Poisson's ratio were the properties that were required to be set. As per the CoventorWare™ material data-base, the elastic modulus of nickel was 220 GPa while the Poisson's ratio was 0.3.

##### 4.2.1.2. Boundary conditions

For the simulations of all the accelerometers, a virtual acceleration of 1g was applied in the negative z direction to the whole device, to replicate the weight of the proofmass due to gravitational force, while the bottom surface of the stationary electrode and the anchors was constrained in all directions. An additional acceleration of 1g was applied in the direction of sensing. Fig. 4.1 shows the boundary conditions applied to an accelerometer. The boundary condition settings are elaborated in Appendix A.

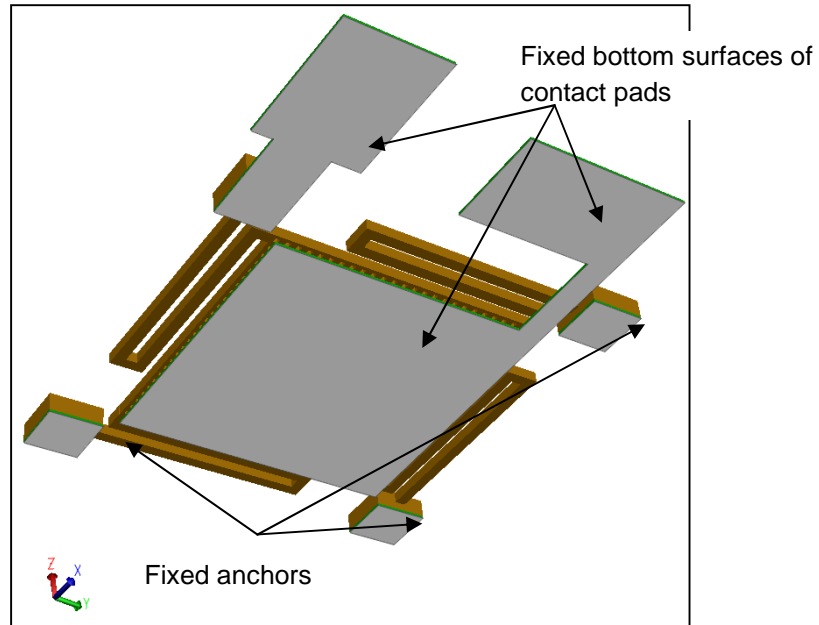


Fig. 4.1. An illustration of the boundary conditions applied to the accelerometer z\_accelerometer650 [4].

#### 4.2.1.3. Meshing

In case of a FEA, the meshing of a structure is one of the most important factors to obtain reliable simulation results. The two major aspects determining the mesh size are first, the quality of mesh and second, the simulation time required for simulating a fine mesh. Hence, the mesh size was selected such that the simulated results converge up to the two decimal places within a reasonable simulation time of 25 minutes.

For all the accelerometers, Manhattan-brick type of mesh was used. In the case of x-y sensing accelerometers, the mesh size was set at 5  $\mu\text{m}$  in all the directions, as shown in Fig. 4.2.

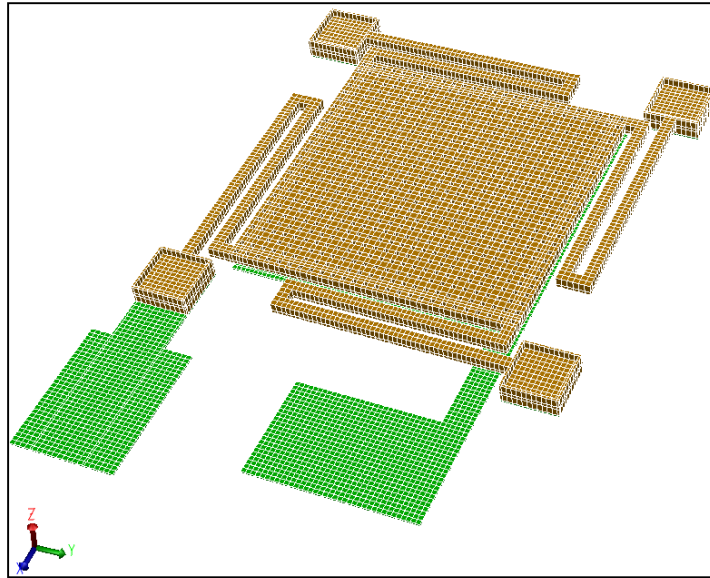


Fig. 4.2. Meshed models of z\_accelerometer650 [4].

#### 4.2.1.4. Displacement analysis

In the case of x-y sensing accelerometers, the displacement of the devices was determined using the MemMechMM module of CoventorWare™ for the boundary conditions discussed in Section 4.2.1.2. Table 4.1 shows the results obtained for the displacements of the devices.

Table 4.1. MEMMech simulation results for x-y sensing accelerometers.

Accelerometer device [4]	Displacement ( $\mu\text{m}$ )
x-y_accelerometer_1605	0.012
x-y_accelerometer_1900	0.025
x-y_accelerometer_1500	0.079

In case of the z\_accelerometer650, the simulations were carried out by varying the initial gap between the electrodes from  $2\ \mu\text{m}$  to  $1.0\ \mu\text{m}$ , as explained in Section 3.2.2. Table 4.2 shows the simulation results for the displacement of the z\_accelerometer650 [4] device.

Table 4.2. MEMMech simulation results for z\_accelerometer650 [4] device for varied initial gaps between the electrodes.

Gap between the electrodes ( $\mu\text{m}$ )	Displacement of flexures ( $\mu\text{m}$ )
2	0.0655
1.8	0.0923
1.5	0.102
1.2	0.180
1.0	No result

As per above results it was observed that the displacement of the flexures increased with decreasing the gap between the electrodes. This increase in the displacement can be attributed to the electrostatic force of attraction between the two electrodes, which increases with a decrease in the gap, as per Eq. (2.5). It was hypothesized that the electrostatic force of attraction would be very high for the gap of 1.0  $\mu\text{m}$ , causing the two plates to snap because of the pull-in, discussed in Section 4.2.1.5. When the plates snap each other, their surfaces try to penetrate, causing the simulations to fail.

Considering the gap of 1.2  $\mu\text{m}$  between the electrodes, which was able to provide the simulation results, further simulations, for the capacitance and pull-in analysis, were carried out for the z\_accelerometer650 [4]. All the other boundary conditions were the same as stated previously.

#### 4.2.1.5. Capacitance analysis

The CoSolveMM of the CoventorWare™ software was used for the analysis of the accelerometer rest capacitance. The boundary conditions applied to the devices were the same as those discussed in Section 4.2.1.2. However, in addition to this, a bias voltage of 1 V was applied across the device plates by setting the stationary electrode and the proofmass voltages to zero and one volts, respectively.

In the case of x-y sensing accelerometers, the change in capacitance was calculated using Eqs. (2.21) and (2.22) for the combs connected in parallel and differential form,

respectively. Table 4.3 shows the capacitance values obtained for the x-y sensing accelerometers. In Table 4.3,  $C_{\max}$  is the maximum capacitance obtained when the distance between the combs is minimum, while  $C_{\min}$  is the minimum capacitance obtained at the maximum distance between the combs, with respect to the rest position of the proofmass.  $C_1$  and  $C_2$  are the capacitances between the combs, as shown in Fig. 2.5.

Table 4.3. The capacitance values for x-y sensing accelerometers.

	x-y_accelerometer_1605 [4]			x-y_accelerometer_1900 [4]			x-y_accelerometer_1500 [4]		
		Paralle l	Differential		Paralle l	Differential		Paralle l	Differential
Rest capacitance $C$ (pF)	$C_1$ 0.385	0.615	0.156	$C_1$ 0.557	0.873	0.238	$C_1$ 0.447	0.722	0.171
	0.23			$C_2$ 0.318			$C_2$ 0.276		
$C_{\max}$ (pF)	$C_1$ 0.388	0.616	0.16	$C_1$ 0.56	0.875	0.245	$C_1$ 0.448	0.723	0.173
	$C_2$ 0.228			$C_2$ 0.315			$C_2$ 0.275		
$C_{\min}$ (pF)	$C_1$ 0.384	0.616	0.152	$C_1$ 0.554	0.875	0.234	$C_1$ 0.446	0.723	0.169
	$C_2$ 0.232			$C_2$ 0.321			$C_2$ 0.277		
$\Delta C$ (fF)		0	8		0	11		0	4

From Table 4.3, it was observed that x-y\_accelerometer\_1900 exhibited a relatively large change in capacitance when connected in differential form compared to other two devices.

In the case of z-sensing accelerometer, the rest capacitance was obtained from the CoSolve simulations. To determine the maximum capacitance of the device, the deformed mesh obtained from the MemMechMM simulations was fed to the MemElectroMM module as the initial condition for the solver. The change in capacitance was calculated by subtracting the rest capacitance obtained from the result of the MEMElectro module, with the increased acceleration values. Table 4.4 shows the simulated capacitance values for the z\_accelerometer650 [4] device for the initial gap of 2.0  $\mu\text{m}$  and 1.2  $\mu\text{m}$ .

Table 4.4. The capacitance values for z\_accelerometer650.

	For initial gap of 2.0 $\mu\text{m}$	For initial gap of 1.2 $\mu\text{m}$
$C$ (pF)	1.894	3.368
$C_{\text{max}}$ (pF)	1.912	3.667
$\Delta C$ (pF)	0.018	0.299

From Table 4.4, it was observed that the change in capacitance was more in case of the reduced initial gap of 1.2  $\mu\text{m}$ , in accordance with the assumption, made previously. Hence, higher electrostatic energy was expected from the device with the initial gap of 1.2  $\mu\text{m}$  (discussed in detail in Section 4.3).

In addition to the capacitance analysis, the pull-in analysis was also performed for the z\_accelerometer650 [4] device.

The pull-in voltage is defined as the voltage when the electrostatic force becomes dominant over the linearly increasing mechanical force and the top electrode snaps the bottom electrode, causing a short circuit of the capacitive plates [50]. The pull-in voltage is given by [50]:

$$V_{pi} = \sqrt{\left(\frac{8}{27} \frac{kd^3}{\epsilon_0 A}\right)} \quad (4.1)$$

where,  $V_{pi}$  is the pull-in voltage,  $d$  ( $\mu\text{m}$ ) is the initial gap between the electrodes,  $k$  is the spring constant of the springs reported as 10.118 N/m by I.Gonenli et al [4], while  $A$  is the area of the electrodes ( $650 \times 650$ ) ( $\mu\text{m}^2$ ) [4].

Table 4.5 shows the calculated and the simulated values of the pull-in voltages obtained for z\_accelerometer650, for the initial gap of 2.0  $\mu\text{m}$  and 1.2  $\mu\text{m}$ .

Table 4.5. Pull-in voltages for z\_accelerometer650.

Initial gap between electrodes ( $\mu\text{m}$ )	Theoretical value of Pull-in voltage (V)	Simulated result of Pull-in analysis (V)
1.2	1.18	1.25
2.0	2.53	2.5

As per the results, the pull-in voltage of the device with the initial gap of 1.2  $\mu\text{m}$  is very close to the bias voltage of 1 V. Hence, the device would not work in the safe range of voltage. On the other hand, the pull-in voltage for the initial gap of 2.0  $\mu\text{m}$  was comparatively in the safer range since it was 1.5 V above the applied bias voltage. However, the amount of change in capacitance was comparatively less, resulting in the smaller output energy.

#### 4.2.2. Energy harvesters

The energy harvesters were simulated similarly as the accelerometers. The simulations of these devices are discussed in detail in this section.

##### 4.2.2.1. Materials and Properties

As described in Chapter 3, the energy harvesters consisted mainly of the aluminum contact pads, to which a moving nickel proof mass and the stationary nickel cantilever beams were connected. Since a heavy proofmass was the design requirement, a relatively heavy metal was required for realizing the proofmass of the device while being mindful of the manufacturability. Hence, nickel was chosen because of its high density and strength [4, 51]. The elastic modulus of 100 GPa [42] and the Poisson's ratio of 0.3 was used for all the simulations carried out for energy harvesters.

##### 4.2.2.2. Spring simulations

The SpringMM module of the CoventorWare™ software was utilized to determine the spring constant of the designed u-shaped springs. The anchors of the springs were constrained from the movement in all the directions, while the free end was displaced by 15  $\mu\text{m}$ .

The simulations gave the reaction force experienced by the spring for the given displacement. The spring constant was calculated by dividing the reaction force by the displacement. As discussed in Chapter 3, each spring had the length 390  $\mu\text{m}$ , width 5  $\mu\text{m}$  and thickness of 25  $\mu\text{m}$ . The simulation results are tabulated in Table 4.6.



Table 4.6. The results for the spring simulations

Number of u-shaped springs in series	Young's modulus for electroplated Nickel, $E$ (GPa) [42]	Displacement in the lateral direction ( $\mu\text{m}$ )	Reaction force ( $\mu\text{N}$ )	Spring constant $k$ (N/m)
1	100	15	4.2234	0.281
5	100	15	2.3964	0.159
7	100	15	2.3611	0.157
15	100	15	0.3026	0.020

The area constrains limited the number of springs in series to seven. Their spring simulation showed that the simulated spring constant was 10 times higher than the desired spring constant calculated in Chapter 3. Hence, the applied acceleration was increased from 1g to 1.5g for further simulations. However, if a total of fifteen springs are connected in series, the obtained spring constant would be close to the desired spring constant of 0.015 N/m.

#### 4.2.2.3. Boundary conditions for the device simulations

For all the energy harvesters, an acceleration of 1g was applied in the negative z-direction to represent the weight of the proofmass acting towards the gravity. In addition to this, an acceleration of 1.5g was applied in the x-direction. The bottom surfaces of the contact pads and all the anchors were constrained in all the directions. Fig. 4.3 illustrates the boundary conditions applied to Model3\_200CL203.

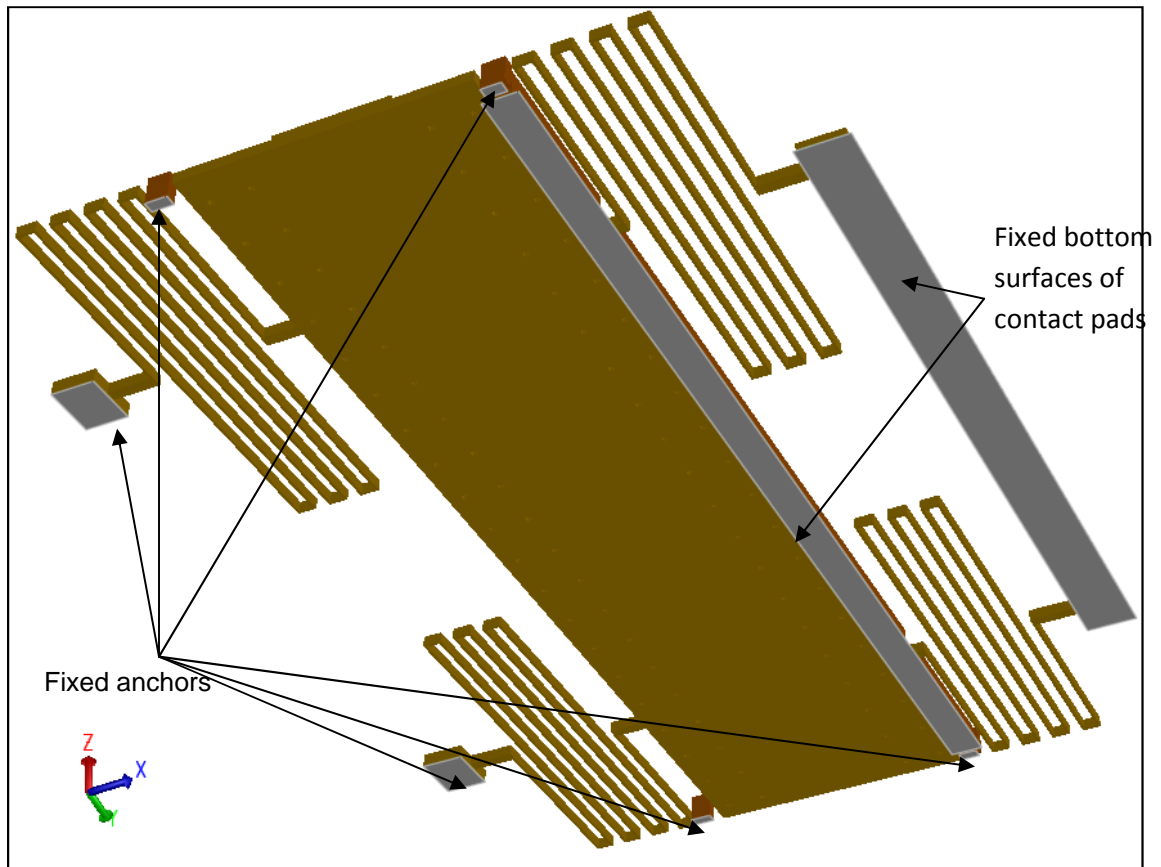


Fig. 4.3. An illustration showing the boundary conditions applied to Model3\_200CL203.

#### 4.2.2.4. Meshing

As discussed previously in Section 4.2.1.3, it is important to optimize the mesh to obtain convergence of the results in a reasonable simulation time. Hence, an optimized mesh of  $5\ \mu\text{m}$  in  $x$  and  $y$  directions and  $10\ \mu\text{m}$  in  $z$ -direction, was used for all the simulations. The convergence up to second decimal point was obtained with the given mesh size. Since all the energy harvesters had an orthogonal geometry, Manhattan-brick type of mesh was used in meshing the devices. Fig. 4.4 shows the meshed model of Model3\_200CL203.

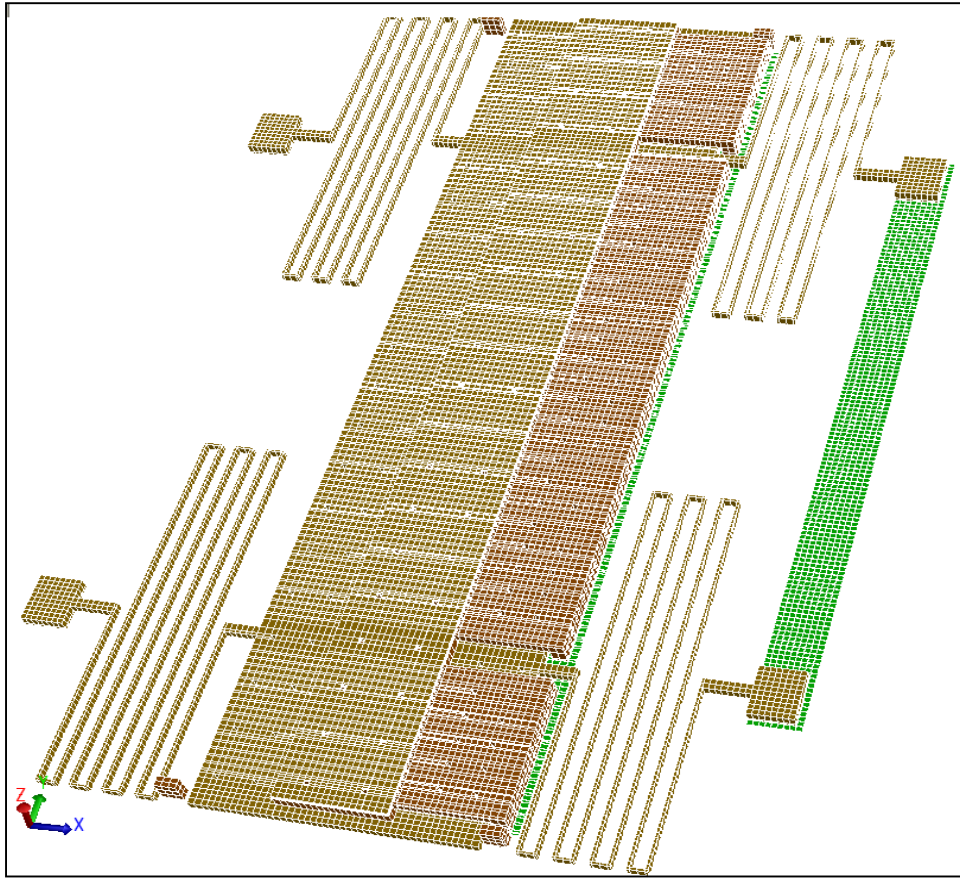


Fig. 4.4. An illustration showing the meshed 3D model of Model3\_200CL203.

#### 4.2.2.5. Displacement analysis

The displacement analysis of the devices was carried out in two phases. First, the MemMechMM module was used to determine the sagging of the proofmass of the device due to its weight. In this case, a virtual acceleration of 1g was applied to the devices in the negative z-direction. Table 4.7 shows the results obtained for the sagging of the devices.

Table 4.7. Simulation results for the sagging of the proofmass of the energy harvesters.

Device	Displacement in negative z-direction ( $\mu\text{m}$ )
Model1_500CL34	1.316
Model2_24CL287	0.827
Model3_200CL203	0.901

The sagging of the device could be a major concern if the acceleration in the z direction is increased beyond 1g, because in that case the device would sag even further and may cause unstable movement of the proofmass. According to the simulation results, it was observed that the proofmass of Model1\_500CL34 was the heaviest.

After the determination of sagging of the proofmass, MemMechMM module was again used to simulate the device for the displacement in the lateral direction. For these simulations, the boundary conditions discussed in Section 4.2.2.3 were applied. The simulation results are tabulated in Table 4.8. In addition, Fig. 4.6 illustrates the displacement of the proofmass for Model3\_200CL203.

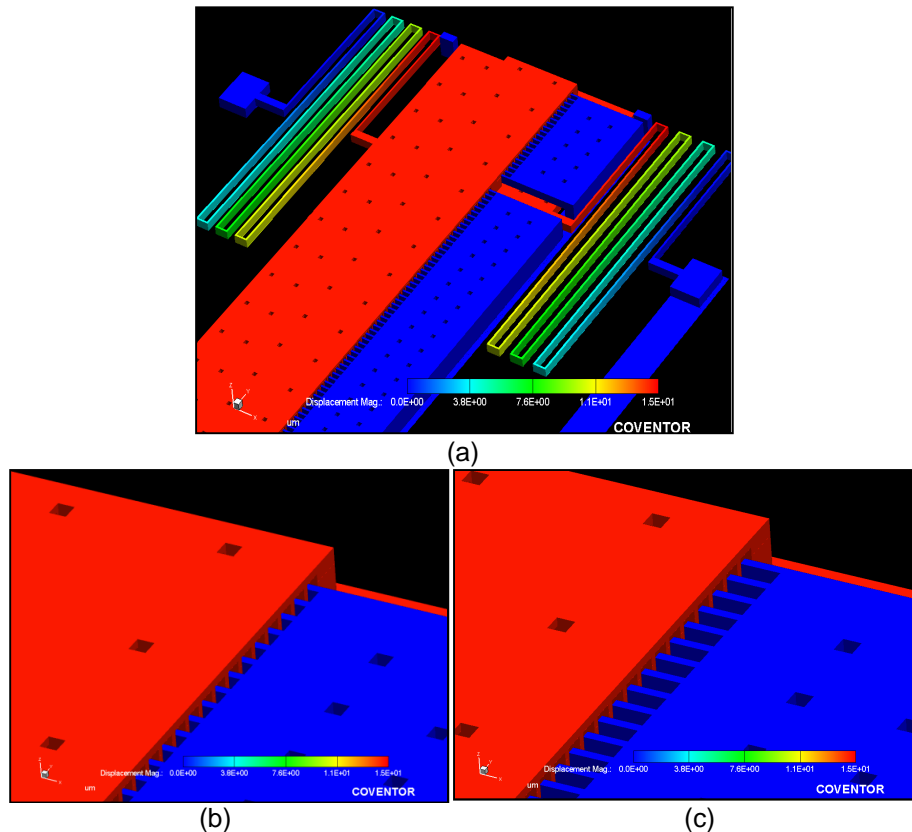


Fig. 4.5. Simulation results for Model3\_200CL203 (a) the displacement of the proofmass at an acceleration of 1.5g (b) Cantilever beams inserted within the hollow cubes, before the displacement (c) Cantilever beams coming out of the hollow cubes, after displacement.

Table 4.8. Simulation results for the lateral displacement of the proofmass for the energy harvesters.

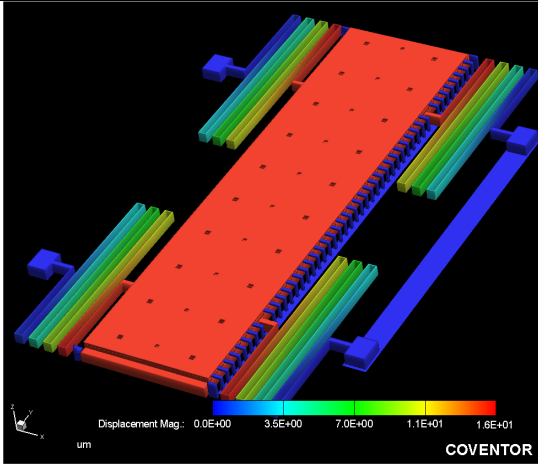
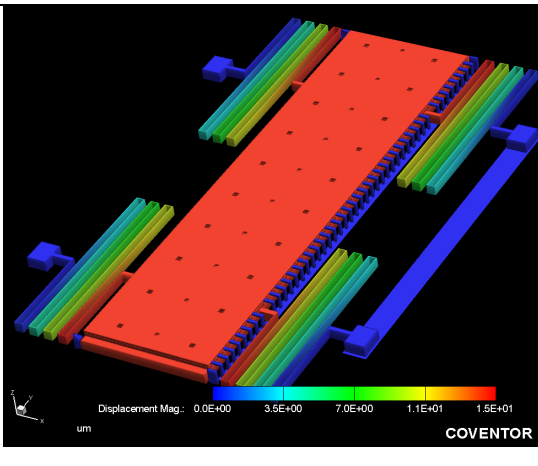
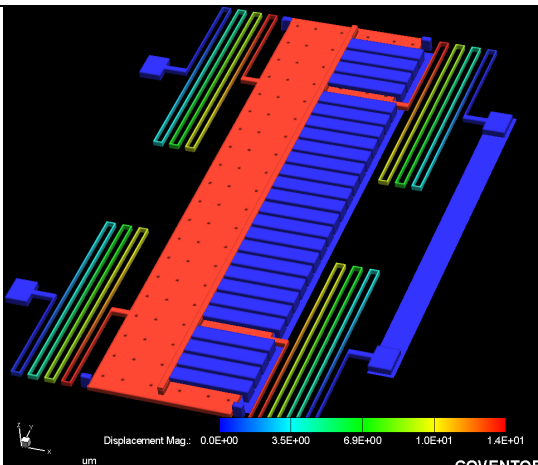
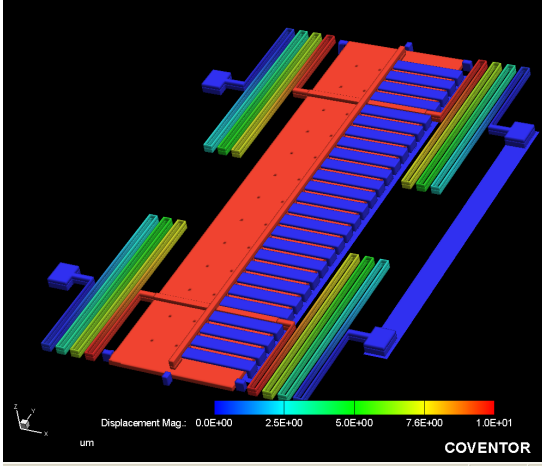
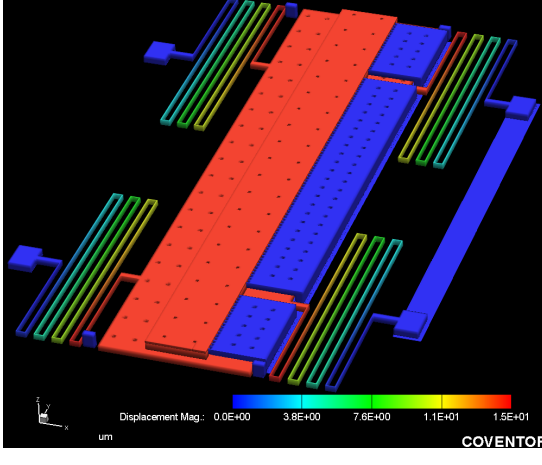
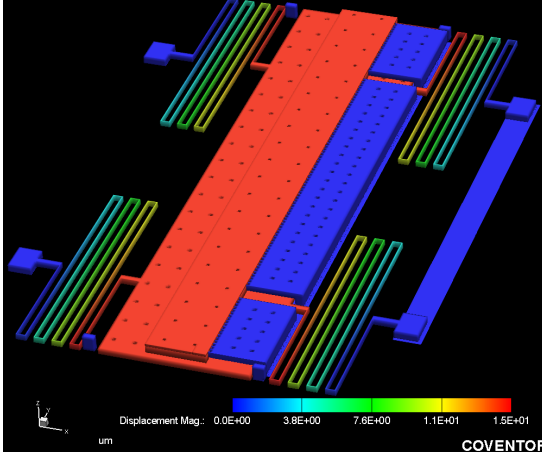
Devices	Displacement ( $\mu\text{m}$ )	3D model of the result
Model1_500CL34	16.16	 <p>Displacement Mag.: 0.0E+00 3.5E+00 7.0E+00 1.1E+01 1.6E+01 um COVENTOR</p>
Model1_500CL34	14.89 (at an acceleration of 1.3g)	 <p>Displacement Mag.: 0.0E+00 3.5E+00 7.0E+00 1.1E+01 1.5E+01 um COVENTOR</p>
Model2_24CL287	13.84	 <p>Displacement Mag.: 0.0E+00 3.5E+00 6.9E+00 1.0E+01 1.4E+01 um COVENTOR</p>

Table 4.8 - Continued

<p>Model2_24CL287.a</p>	<p>10.46</p>	
<p>Model3_200CL203</p>	<p>15.14</p>	
<p>Model3_200CL203. a</p>	<p>14.65</p>	

From the simulations, it was observed that the Model1\_500CL34 showed higher displacement of 16  $\mu\text{m}$  at an acceleration of 1.5g. Hence, in case of Model1\_500CL34, the required acceleration was reduced to 1.35g, in order to obtain the desired displacement 15  $\mu\text{m}$ . For all the other simulations, an acceleration of 1.35g was used for simulating the Model1\_500CL34. On the other hand, Model2\_24CL287 showed a displacement of only 13  $\mu\text{m}$ , which was less than the desired displacement of 15  $\mu\text{m}$ , at an acceleration of 1.5g. Furthermore, the displacement of the modified Model2\_24CL287.a was even less and of the order of 10  $\mu\text{m}$ . This was mainly because the thickness of the proofmass was reduced to 15  $\mu\text{m}$ , as per the fabrication constraints discussed in Chapter 3. Therefore, the total weight of the proofmass was decreased. Hence, the modified model showed even less displacement. However, at an acceleration of 1.5g, the Model3\_200CL203 showed the displacement of 15.14  $\mu\text{m}$  which was according to the design considerations. In addition, the modified models, Model3\_200CL203.a and Model3\_200CL203.b, showed the displacements, which were lower than the unmodified model. However, the displacements were close to 15  $\mu\text{m}$ .

#### 4.2.2.6. Capacitance analysis

The MemElectroMM was observed to be faster than the CoSolveMM module. Hence, to avoid the long simulation time, the MemElectroMM module of CoventorWare™ was used for analyzing the capacitance of the devices.

For analyzing the rest capacitance of the devices, the boundary conditions described in Section 4.2.2.3, were applied to the devices and a virtual bias voltage of 1 V was applied between the proofmass and the cantilever beams by setting the proofmass and the cantilevers beams at one and zero volts, respectively. The deformed mesh obtained from the MemMechMM simulations for determining the sagging, was fed to the MemElectroMM module as the initial condition for the solver. The analysis set-up is elaborated in Appendix A.

Change in capacitance was determined by applying the similar bias voltage and boundary conditions, as described above. However, in this case, the deformed mesh obtained from the MemMechMM simulation for the determination of the lateral displacement of the proofmass, was fed to the MemElectroMM module as the initial condition. Table 4.9 shows the CoSolve simulation results.

Table 4.9. Simulation results for the capacitance analysis using MemElectroMM.

Device Model	acceleration (m/s <sup>2</sup> )	Rest Capacitance $C_{max}$ (pF)	Displacement ( $\mu$ m)	Capacitance after displacement $C_{min}$ (pF)	Change in capacitance $\Delta C$ (pF)	Number of combs
Model1_500CL34	12.74	0.119	14.89	0.090	0.029	46
Model1_500CL34.a	12.74	0.119	14.89	0.090	0.029	46
Model2_24CL287	14.7	1.067	13.84	0.961	0.106	28
Model2_24CL287.a with cantilever beam width 50 $\mu$ m	14.7	0.9806	10.46	0.8997	0.0809	28
Model3_200CL203	14.7	1.1141	15.14	0.967	0.181	120
Model3_200CL203.a with cantilever width 5 $\mu$ m	14.7	0.8111	14.65	0.6844	0.136	84
Model3_200CL203.b with cantilever width 10 $\mu$ m	14.7	0.8023	14.65	0.6864	0.116	58

As discussed in the Chapter 3, the devices have the maximum capacitance when at rest. The capacitance changes to minimum when the proofmass moves away from the cantilever beams. From the simulation results it was observed that, all the capacitances obtained for the Model1\_500CL34 were the lowest. This was mainly because the overlap area of the cantilever beams and the hollow cubes was less than that in the other two models, as explained in Section 3.3.3. On the other hand, in case of the Model2\_24CL287 the rest capacitance was approximately nine times more than that of Model1\_500CL34, since the model was designed such that the overlap area of the cantilever beams and the base electrode of the proofmass was increased (refer Section 3.3.3.2). Hence, it contributed to the increase in the device capacitance.

However, the increase in the change in capacitance was only 3.655 times the change in



capacitance for the Model1\_500CL34. This was mainly because the proofmass of Model2\_24CL287 showed less displacement compared to Model1\_500CL34. The modified Model2\_24CL287.a showed even lower change in capacitance, since it had lowest displacements because of the lightest proofmass (explained in Section 4.2.2.5). The rest capacitance of the modified Model2\_24CL287.a was observed to be less than that of the unmodified model by 86.4 fF because the width of each cantilever beam was reduced from 54  $\mu\text{m}$  to 50  $\mu\text{m}$ . On the other hand, the Model3\_200CL203 showed the highest values of capacitance because this model was designed with highest number of combs and in addition, had the cantilever plates, which contributed to the device capacitance, as explained in Section 3.3.3.3. Moreover, the displacement of the proofmass was also as per the design consideration. Hence, the model showed the highest change in capacitance. The modified models of Model3\_200CL203 showed lower capacitance values because of the lesser number of combs compared to the unmodified model.

#### 4.2.2.7. Modal analysis

It is important to find the resonant frequency in order to determine the maximum response of the devices for an intended input vibration. Hence, the modal analysis was used to determine the resonant frequency of the structure at the equilibrium.

The MemMechMM module was used, in which the settings were made to perform an additional modal analysis. All the boundary conditions, discussed in Section 4.2.2.3., were applied to the devices. The analysis gave the modal frequencies of the device along with its generalized mass at the corresponding resonant frequency. The set-up of the analysis is discussed in detail in Appendix A, while the results are tabulated in the Table 4.10.

Table 4.10. Simulation results for modal analysis.

Devices	Resonant frequency (Hz)	Mass (kg)
Model1_500CL34	$1.461 \times 10^2$	$3.852 \times 10^{-7}$
Model2_24CL287	$1.617 \times 10^2$	$3.129 \times 10^{-7}$
Model3_200CL203	$1.512 \times 10^2$	$3.597 \times 10^{-7}$

From the results of the modal analysis, the resonant frequency of the devices was in the range of 145-160 Hz. However, the source frequency, which is the frequency of vibration of an aircraft, is in the range of 100-110 Hz. The mismatch between the source frequency and the resonant frequency of the device may cause a loss in the generated electrostatic energy [13]. However, the reduction in the resonant frequency of the devices is possible if the mass of the devices is increased, as per Eq. (3.3).

The mechanical analysis performed on the accelerometers and the energy harvesters, verified that the accelerometers were best designed as sensors. Moreover, the amount of change in the capacitance of the accelerometers was much less than the energy harvesters. Hence, their energy output was expected to be very low as compared to the energy harvesters. The energy and the power calculations were performed for the energy harvesters and only the y\_accelerometer\_1500 [4] and z\_accelerometer650 [4] with the initial gap of 1.2  $\mu\text{m}$ , for the comparison.

#### 4.3. Energy and power estimations

##### 4.3.1. Calculations for the electrostatic energy

The electrostatic energy was calculated for the charge-constrained and the voltage-constrained conversion cycles, as discussed in Chapter 2.

#### 4.3.1.1. Charge-constrained conversion

In case of the charge-constrained conversion cycle, the charge on the variable capacitive device is held constant while the voltage changes as per the change in the capacitance of the variable capacitor. Eq. (2.13) was used to calculate the electrostatic energy rewritten as:

$$E = \frac{V_{in}^2}{2} \Delta C_v \left[ \frac{C_{vmax}}{C_{vmin}} \right] \text{ (J)} \quad (4.1)$$

In case of the energy calculations for the energy harvesters,  $V_{in}$  was 10 V. However, in case of the energy calculation for the accelerometers  $V_{in}$  was limited to 1 V, due to the pull-in constraints. Table 4.11 shows the calculated results. The Model1\_500CL34 was modified only for the thickness of the base electrode and the top-covering plate, as discussed in Chapter 3. Hence, the modified model showed the same results for the displacement and the capacitance, as that of the unmodified model. Hence, the energy calculations for only the unmodified model are tabulated in Table 4.11 along with the rest of the devices.

Table 4.11. The calculated electrostatic energy for charge-constrained conversion cycle.

Device	Input voltage $V_{in}$ (V)	Calculated electrostatic energy $E$ (pJ) for charge-constrained conversion cycle
x-y_accelerometer_1500 [4]	1	0.00204
z_accelerometer650 [4]	1	0.1627
Model1_500CL34	10	1.917
Model2_24CL287	10	5.884
Model2_24CL287.a	10	4.408
Model3_200CL203	10	10.823
Model3_200CL203.a	10	8.200
Model3_200CL203.b	10	6.779

Since the electrostatic energy is directly proportional to the change in capacitance and to the ratio of maximum and minimum capacitance, the calculations validated that the design of Model3\_200CL203 and its derivatives, would generate more electrostatic energy compared to the other models because of the relatively higher capacitance values.

#### 4.3.1.2. Voltage-constrained conversion

In the case of the voltage-constrained conversion cycle, the voltage on the variable capacitor is held constant while the charge is varied as per the capacitance of the variable capacitor device. Even though it is not desirable to connect a continuous voltage source for an energy harvester, an electret material can be used to provide a constant potential across the variable capacitor [34, 52-54]. An electret is a polarized dielectric material, which can produce a potential ranging from 100-200 V [55]. An electret can hold the charge densities for over an estimated period of hundred years [53]. Materials such as Teflon [52] and SiO<sub>2</sub>/Si<sub>3</sub>N<sub>4</sub> double layer [55] can be used as electret materials.

Since the energy harvesters were designed such that they can sustain high input voltages without pull-in, an electret material which can create a potential of 100 V could be effectively used for a voltage-constrained conversion mechanism. The main advantage of such an electret-based conversion is that, it will not require a switching circuit, which is inevitable in the case of a charge-constrained conversion. Moreover, a higher voltage source will result in higher energy out puts, as shown in Table 4.12.

Eq. (2.17) was used to calculate the energy generated, rewritten here as:

$$E = \frac{1}{2} V_{in}^2 \Delta C_v \text{ (J)} \quad (4.2)$$

Table 4.12. The calculated electrostatic energy for the voltage-constrained conversion cycle.

Devices	Calculated energy $E$ (pJ)
x-y_accelerometer_1500 [4]	0.002
z_accelerometer650 [38]	0.114
Model1_500CL34	145
Model2_24CL287	530
Model2_24CL287.a	404.5
Model3_200CL203	905
Model3_200CL203.a	683.5
Model3_200CL203.b	580

From Eq. (4.2), the electrostatic energy is directly proportional to the change in capacitance and to the square of the input bias voltage. Thus, the calculated energies were expected to reflect the trends similar to that of the capacitance. Hence, the Model3\_200CL203 showed that it would generate the highest electrostatic energy than the rest of the devices. The electrostatic energy obtained for the voltage-constrained conversion cycle was more than the energy obtained for the charge-constrained conversion cycle.

#### 4.3.2. Calculations for the generated power

Power is the energy per unit time. Hence, the total amount of power generated by an energy harvester which operates at the source frequency of 100 Hz is given by:

$$P = E \times \omega \quad (4.3)$$

where,  $P$  is the estimated generated power,  $E$  is the calculated electrostatic energy and  $\omega$  is the source frequency given by  $2\pi f$ , where  $f$  is considered 100 Hz for calculations [40, 41]. Table 4.13 gives the estimated power that can be generated from the energy harvester as well as accelerometers.

Table 4.13. The estimated power output for the accelerometer and energy harvesters.

Devices	The estimated power $P$ ( $\mu\text{W}$ )	
	Charge-constrained conversion cycle	Voltage-constrained conversion cycle
x-y_accelerometer_1500 [4]	$0.204 \times 10^{-6}$	$0.2 \times 10^{-6}$
z_accelerometer650 [4]	$0.162 \times 10^{-6}$	$11.4 \times 10^{-6}$
Model1_500CL34	$0.1917 \times 10^{-3}$	0.0145
Model2_24CL287	$0.5884 \times 10^{-3}$	0.0530
Model2_24CL287.a	$0.4408 \times 10^{-3}$	0.0404
Model3_200CL203	$1.0823 \times 10^{-3}$	0.0905
Model3_200CL203.a	$0.8200 \times 10^{-3}$	0.0683
Model3_200CL203.b	$0.6779 \times 10^{-3}$	0.0580

From Table 4.13, it is clear that the voltage-constrained conversion mechanism would allow the harvesters to generate more power, if an electret material, generating high potential was

used. However, since the volumes of the accelerometer and the energy harvesters were not the same, the calculated power was normalized with respect to the device volume, in order to make a fair comparison. The Table 4.14 shows the comparison of the volumetric power for all devices, where  $P_c$  the volumetric power for the charge-constrained conversion is cycle and  $P_v$  is the volumetric power for the voltage-constrained conversion cycle.

Table 4.14. The volumetric power output for accelerometer and energy harvesters.

Devices	Volume (cm) <sup>3</sup>	The volumetric power	
		For Charge-constrained conversion cycle, $P_c$ ( $\mu\text{W}/\text{cm}^3$ )	For Voltage-constrained conversion cycle, $P_v$ ( $\mu\text{W}/\text{cm}^3$ )
x-y_accelerometer_1500 [4]	$4.74 \times 10^{-6}$	0.043	0.042
z_accelerometer650 [38]	$2.11 \times 10^{-6}$	0.076	5.402
Model1_500CL34	$5 \times 10^{-5}$	3.834	290
Model2_24CL287	$5 \times 10^{-5}$	11.768	1060
Model2_24CL287.a	$5 \times 10^{-5}$	8.816	808
Model3_200CL203	$5 \times 10^{-5}$	21.646	1810
Model3_200CL203.a	$5 \times 10^{-5}$	16.4	1216
Model3_200CL203.b	$5 \times 10^{-5}$	13.558	1160

The calculated power was normalized with respect to the volume in terms of (cm)<sup>3</sup>, assuming an array of the devices connected in series within the volume of (cm)<sup>3</sup>. From Table 4.14, it was observed that very promising volumetric power outputs could be obtained from an array of energy harvesters, operated under the voltage-constrained conversion mechanism. The devices would need a few modifications to incorporate the electret material in the design, in order to implement the voltage-constrained conversion mechanism. These modifications would be the major focus of the future work for the energy harvesters discussed here.

#### 4.3.3. Comparisons

A number of electrostatic energy harvesters has been reported by various research groups, as discussed in Chapter 1. However, the operating conditions, such as the source acceleration, operating frequency and the input voltage are different for each of the reported

devices. As explained by Y. Jeon et. al [3], the power generated by an energy harvester at a vibration frequency of  $\omega$  , is given by:

$$P = \alpha \omega^3 Y^2 \quad (4.5)$$

where,  $Y$  is the amplitude of the source acceleration and  $\alpha$  is the transduction factor given by [3]:

$$\alpha = \frac{m \zeta_e}{4 \zeta_T^2} \quad (4.6)$$

where,  $m$  is the mass,  $\zeta_T$  is the total damping ratio, and  $\zeta_e$  is the electrical damping ratio, which depends upon the design of the device. For an acceleration  $a$  given by:

$$(a = Y \omega^2) \quad (4.6)$$

Eq. (4.5) can be rewritten as:

$$P = \frac{\alpha(a)^2}{\omega} \quad (4.7)$$

Hence, the mechanical power transferred to the energy harvesters is proportional to the square of the source acceleration. Since a varied range of source acceleration was reported, the volumetric power was normalized with respect to the square of the source acceleration, so that the devices can be compared to each other.

Table 4.15 shows the comparative account of the designed energy harvesters with a few reference devices. In the Table,  $V_{in}$  refers to the input bias voltage,  $P_c$  and  $P_v$  are the volumetric powers calculated for the designed energy harvesters, for the charge-constrained and the voltage-constrained conversion cycles, respectively. The generalized volumetric power reported in the references is given by  $P$  .

Table 4.15. The comparison of normalized volumetric power

Devices	Volume (cm <sup>3</sup> )	Number of combs	$a$ (m/s <sup>2</sup> )	$f$ (Hz)	The normalized volumetric power $P/a^2$ ( $\mu\text{W}\cdot\text{s}^4/\text{cm}^3\text{m}^2$ )	
1. Ref [54]	0.0016	N/A	160	911	1.210 (with $V_{in}=150$ V)	
2. Ref [13]	0.013	N/A	1500	4100	0.000002 ( $V_{in}$ not reported)	
3. Ref [56]	1	N/A	31.58	20	0.0316 ( $V_{in}$ not reported)	
4. Ref [52]	0.1	N/A	125	800	0.0032 (with $V_{in} = 73$ V)	
					$P_c/a^2$ ( $\mu\text{W}\cdot\text{s}^4/\text{cm}^3\text{m}^2$ ) (with $V_{in}=10$ V)	$P_v/a^2$ ( $\mu\text{W}\cdot\text{s}^4/\text{cm}^3\text{m}^2$ ) (with $V_{in}=100$ V)
x-y_accelerometer_1500 [38]	$4.74 \times 10^{-6}$	100	9.8	100	$0.44 \times 10^{-3}$ (with $V_{in}=1$ V)	$0.437 \times 10^{-3}$ (with $V_{in}=1$ V)
z_accelerometer650 [4]	$2.11 \times 10^{-6}$	N/A	9.8	100	$0.79 \times 10^{-3}$ (with $V_{in}=1$ V)	0.056 (with $V_{in}=1$ V)
Model1_500CL34	$5 \times 10^{-5}$	46	12.74	100	0.022	1.715
Model2_24CL287	$5 \times 10^{-5}$	28	14.7	100	0.052	4.711
Model2_24CL287.a	$5 \times 10^{-5}$	28	14.7	100	0.039	3.59
Model3_200CL203	$5 \times 10^{-5}$	120	14.7	100	0.096	8.044
Model3_200CL203.a	$5 \times 10^{-5}$	84	14.7	100	0.072	5.404
Model3_200CL203.b	$5 \times 10^{-5}$	58	14.7	100	0.060	5.155

From the Table 4.15, it was observed that the energy harvesters designed here showed better results as compared to most of the referred devices, except the one designed by F.Peano et.al [54]. However, the applied bias voltage  $V_{in}$  was reported to be 150 V [54], which is more than the maximum bias voltage considered in this work. In addition to this, all the devices reported in [13, 52, 54, 56] were operated at unrealistically high accelerations. As it was expected, the energy harvester Model3\_200CL203 showed the best volumetric powers normalized with respect to the acceleration, since the device was designed to operate at a relatively low acceleration.



#### 4.4. Summary

In this Chapter, the accelerometers designed by I.Gonenli et al. [4] and the new energy harvesters were analyzed using the CoventorWare™ software, which is a FEA simulation tool. After determining the maximum and minimum capacitances of the devices, the change in capacitance was calculated. These capacitance values were then used to calculate the electrostatic energy, which can be generated from the devices, when they are operated in a charged-constrained or the voltage-constrained conversion mechanism. In addition to this, the power outputs were estimated and compared to the devices reported by various other research groups. From the comparisons, it was observed that the energy harvester devices presented in this work would obtain considerable power outputs, even though they are operated at much lower source accelerations.

## CHAPTER 5

### CONCLUSION

New electrostatic energy harvesters were designed and simulated using CoventorWare™ simulation software. The main challenge in designing an energy harvester was to achieve a large displacement of a small proofmass, in order to achieve a large change in the capacitance of the device. Hence, a novel concept of a wrap-around capacitor was introduced, which would provide four times more capacitance compared to a typical inter-digitated comb structure. Different device designs were proposed. The designs differed in the dimensions of the hollow cubic structures and the dimensions of the cantilever beams. A generalized fabrication process was also proposed for the designed energy harvesters. In addition, a few design modifications were proposed taking into consideration the fabrication process limitations. The designs were simulated to determine the spring constant, displacement of nickel proofmass and the capacitance of the structure. The displacement analysis was performed for the source acceleration in the range of 1.35-1.5g (where,  $1g = 9.8 \text{ m/s}^2$ ) in the lateral direction and 1g acceleration acting in the negative z-direction of the device. The capacitance analysis was done by applying a potential difference of 1 V across the device such that a virtual voltage of 1 V and 0 V was applied to the proofmass and the stationary cantilever beams. The capacitance values obtained from the simulations were then utilized for the calculation of the electrostatic energy that would be generated by each device. The energy estimates were found for both charge-constrained and voltage-constrained conversion cycles. Power generated by each device over the frequency of 100 Hz was then calculated by multiplying the energy with the frequency. The device designs were compared with each other based on the normalized volumetric power. In addition, the energy harvesters and the accelerometers were compared to few other devices reported by different research groups on the basis of the volumetric power normalized with respect to the square of the applied acceleration. It was observed that the energy harvesters designed in this work would provide better volumetric

power at relatively low acceleration of the range of 1.35-1.5g, compared to the other devices which were reported to work at unrealistically high accelerations. From the comparisons, it was observed that the devices would generate more power when operated under voltage-constrained conversion mechanism, compared to the charge-constrained conversion. Use of an electret material was proposed for realizing the voltage-constrained conversion, such that continuous high bias in the range of 100 V can be provided. In future work, a modified the device fabrication process needs to be proposed for incorporating the electret material in addition to fabrication and characterization of the devices.

APPENDIX A  
ENERGY HARVESTER DESIGNS AND SIMULATIONS

### A.1 Introduction

Three energy harvester designs were proposed in this work. The devices mainly consisted of:

1. A proofmass with a train of hollow cubes on a base electrode
2. Stationary cantilever beams, which were inserted in the hollow cubes when at rest
3. Two contact pads, one for the cantilever beams and the proofmass each
4. Four mechanical stops, two on each side of the proofmass
5. Four springs, two on each side of the proofmass.

The designs varied in the dimensions of the hollow cubic enclosures and the cantilever beams. In this section the designs of the energy harvesters are shown along with the illustrations of procedures of the simulations.

### A.2 Illustration of design layout and 3D model in CoventorWare™

Fig. A.1 shows the design layout of Model3\_200CL203. The layout file is used to define the masks for the different layers of the device. The layout consisted of eight masks mainly:

1. Substrate
2. Contact\_Pads
3. Sacrificial\_Layer1: for the sacrificial layer between the substrate and the proofmass.
4. Base\_Of\_Cubic\_Capacitors: Base electrode
5. Sacrificial\_Layer2\_B4\_Cantilevers: for the sacrificial layer between the base electrode and the cantilever beams.
6. Cantilever\_Beams: for the sidewalls of the hollow cubes and the cantilever beams.
7. Sacrificial\_Layer2\_After\_Cantilevers: for the sacrificial layer between the cantilever beams and the top plate.
8. Top\_Layer\_of\_Cubic\_Train

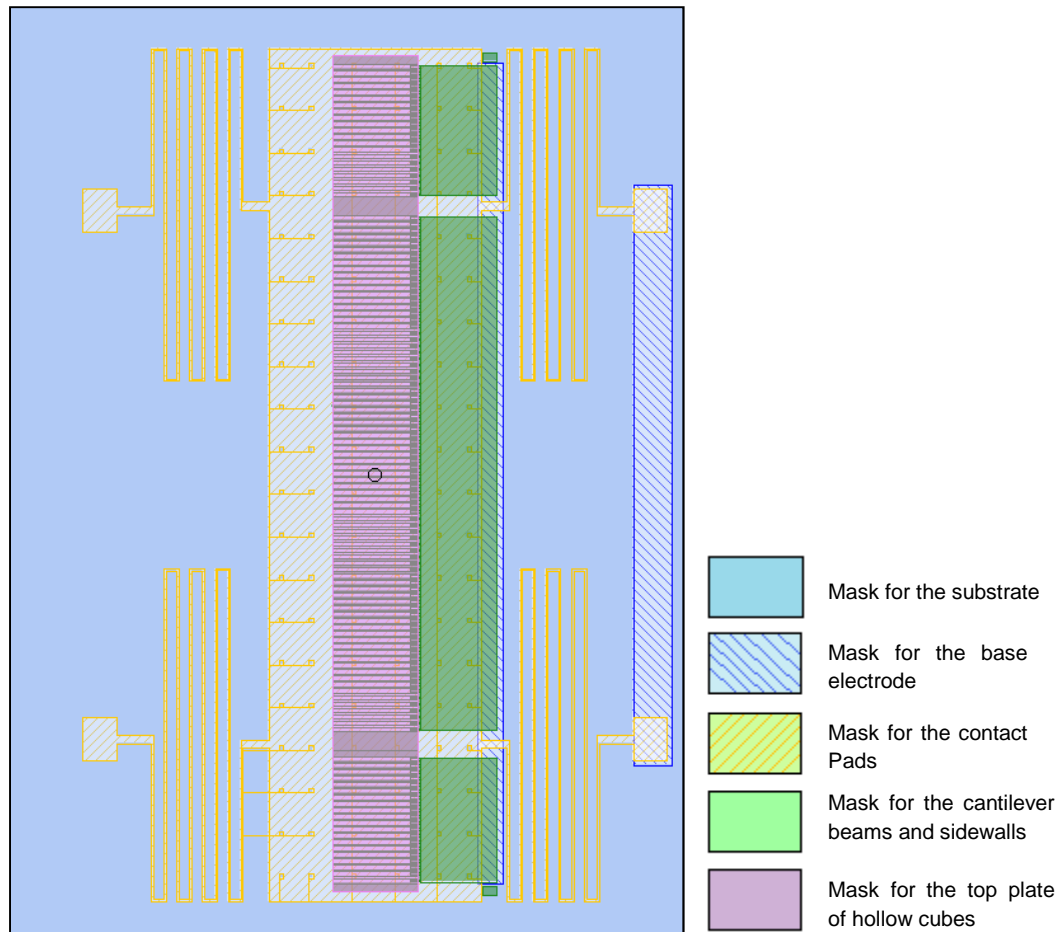


Fig. A.1. Layout of Model3\_200CL203 illustrating the different layers used to build the 3D model of the device. The sacrificial layers are not seen in the figure.

These masks are then utilized in the process editor file (.proc) of CoventorWare™ to build the 3D model of the device. In the process editor, each layer is defined based on the type of layer, material and thickness of the layer, the mask and the polarity of the mask. Fig.A.2 illustrates the process editor file used to create the 3D model of Model3\_200CL203 shown in Fig.A.3.

Number	Step Name	Layer Name	Material Name	Thickness	Mask Name	Photoresist
0	Substrate	Substrate	SILICON	40	SubstrateMask	
1	Sputtering Contact Pad for Cantilever	Contact Pad for Cantilever	ALUMINUM	1		
2	Pattern contact pad				Contact_Pads	+
3	Sputtering Sacrificial Layer 1	Sacrificial Layer 1	POLYIMIDE	5		
4	Pattern Sacrificial Layer 1				Sacrificial_Layer_1	+
5	Sputtering Base of Cubic Capacitors	Base_of_Cubic_Capacitors	NICKEL	25		
6	Patterning Base of Cubic Capacitors				Base_Of_Cubic_Capacitors	+
7	Deposit Sacrificial Layer B4 Cantilever layer	Sacrificial Layer B4 Cantilever layer	POLYIMIDE	5		
8	Pattern Sacrificial Layer B4 Cantilever layer				Sacrificial_Layer2_B4_Cantilevers	+
9	Sputter Cantilever Beams	Cantilever Beams	NICKEL	10		
10	Pattern Cantilever Beams				Cantilever_Beams	+
11	Deposit Sacrificial Layer After Cantilevers	Sacrificial Layer after Cantilever	POLYIMIDE	5		
12	Pattern Sacrificial Layer After Cantilevers				Sacrificial_Layer2_After_Cantilevers	-
13	Sputter Top Plate	Top Plate	NICKEL	5		
14	Pattern Top Plate				Top_Layer_of_Cubic_Train	+
15	Remove Sacrificial layer	Sacrificial Layer 1				
16	Remove Sacrificial Layer B4 Cantilever Beams	Sacrificial Layer B4 Cantilever layer				
17	Remove Sacrificial Layer After Cantilever Beams	Sacrificial Layer after Cantilever				

Fig. A.2. The process file for the energy harvesters for building the solid 3D model from the layout file.

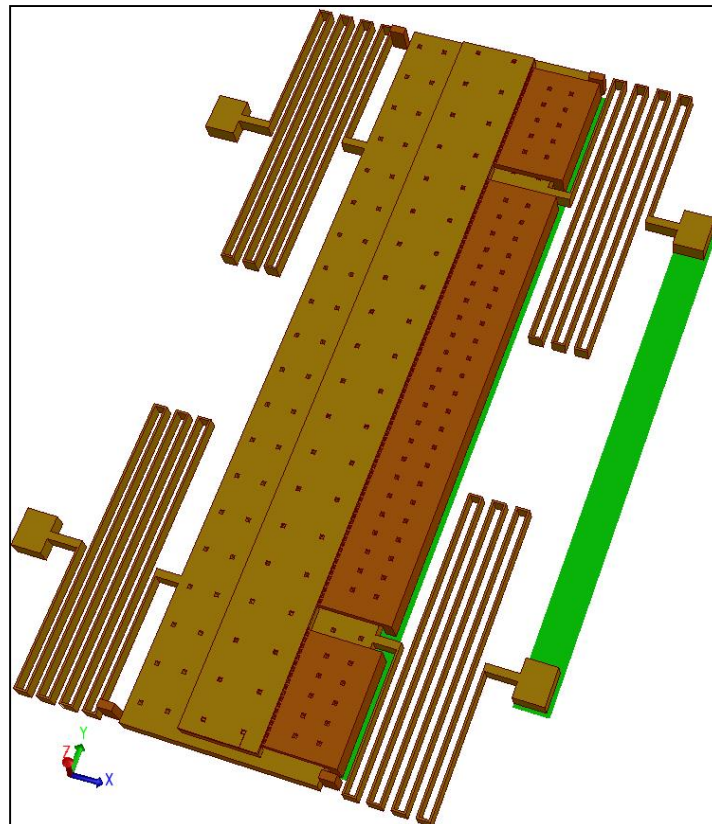


Fig. A.3. The 3D model of Model3\_200CL203, built by using the layout file shown in Fig. A.1 and the process file shown in Fig. A.2.

After creating the 3D model, it is important to mesh the model in order to perform the Finite Element Analysis (FEA). The mesher settings are shown in Fig. A.4. The meshed model is

shown in Fig. 4.4. In the mesher settings tab, the type of mesh, meshing algorithm, order of element and the size of the mesh are defined. The meshed model is then subjected to boundary conditions, explained in Section. 4.2.2.3.

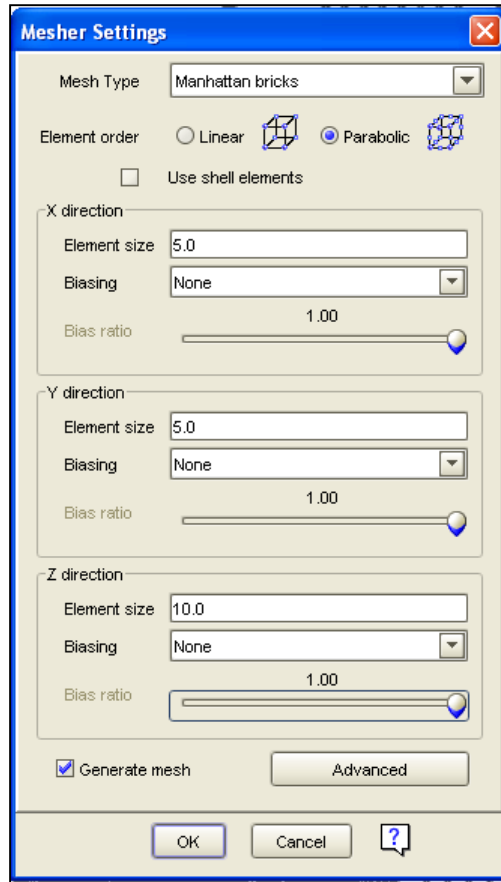


Fig. A.4. Mesher settings for the energy harvesters.

For the displacement analysis, the MemMechMM of the CoventorWare™ software was used. The module was set to perform a linear and steady state mechanical analysis with no additional analysis, as shown in Fig. A.5.



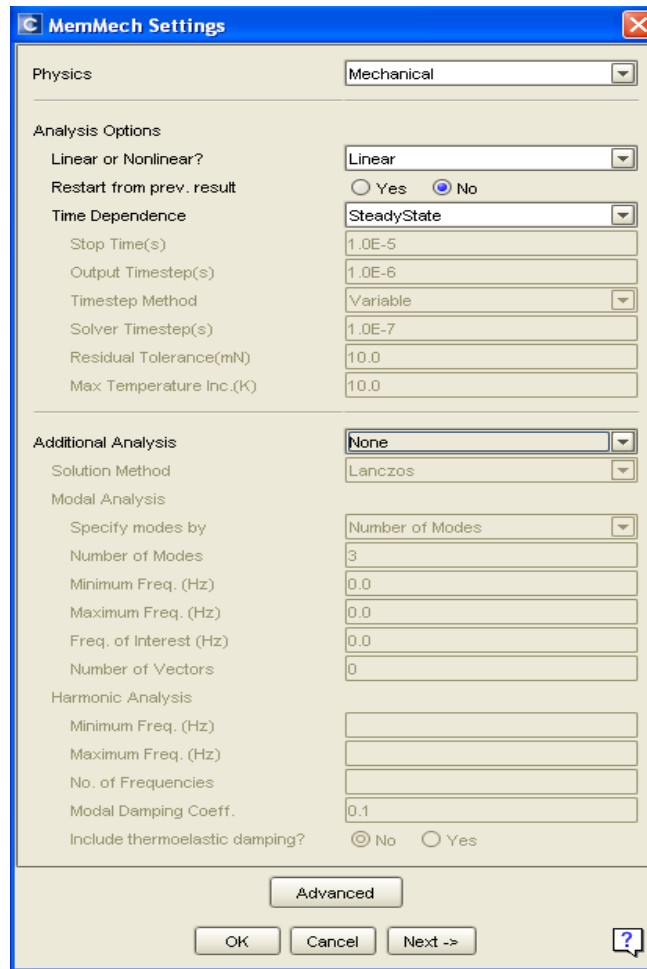


Fig. A.5. MemMechMM settings

Once the initial analysis conditions are specified, the SurfaceBCs tab, shown in Fig. A.6, is used to define the fixed patches on the device. The load is then applied to the device, by setting the volume boundary conditions using VolumeBC. In this tab, a virtual acceleration of 1.5g was applied in the lateral direction (negative-x direction with respect to the device) and additional 1g acceleration was applied in the negative-z direction, as illustrated in Fig. A.7.

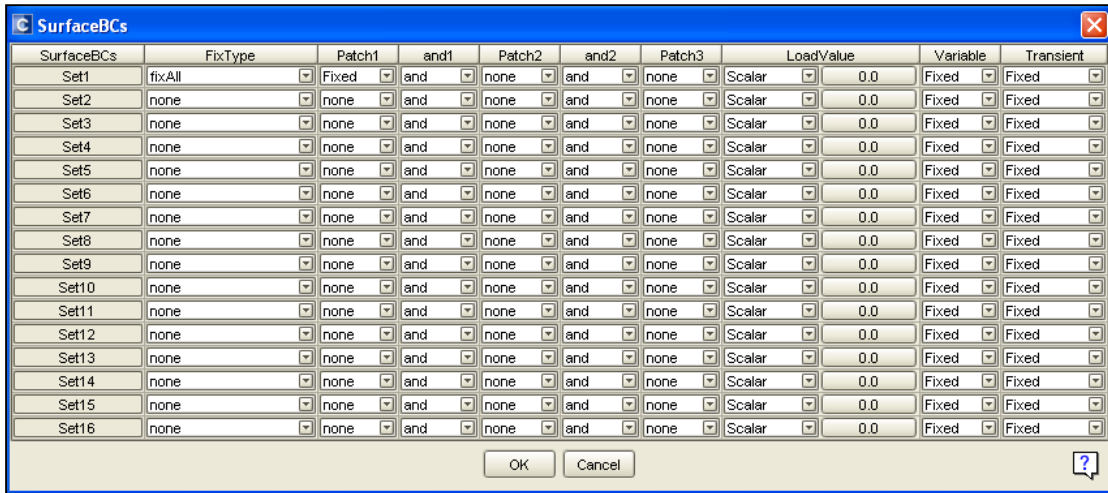


Fig. A.6. SurfaceBCs of the MemMechMM module, used to define the fixed patches on the device model.

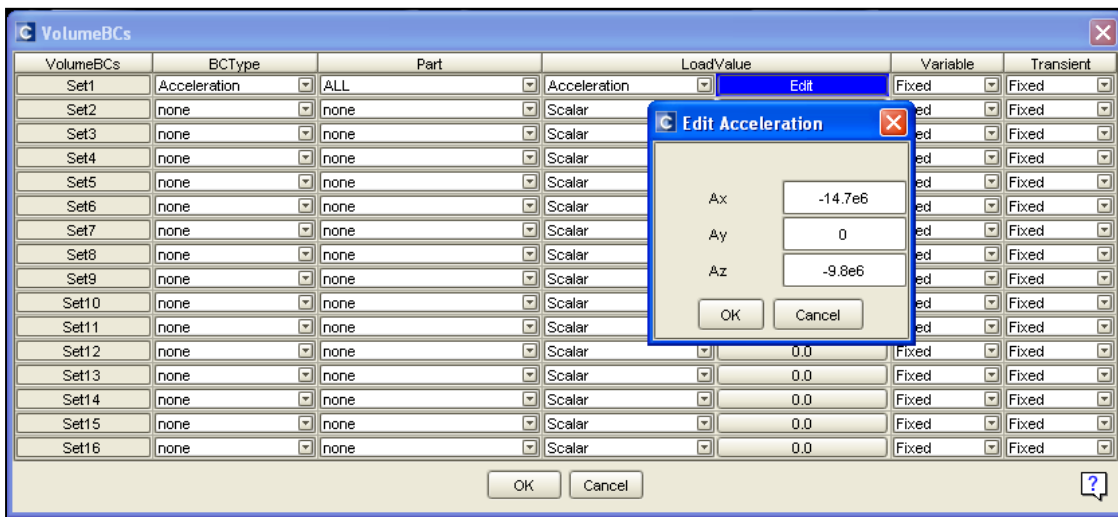


Fig. A.7. VolumeBCs of the MemMechMM module for specifying the load on the device.

The MemMech analysis provided a deformed mesh, upon completion of the simulations. This deformed mesh was then fed as an initial solver condition to the MemElectroMM for the capacitance analysis. The initial solver settings for the MemElectroMM are shown in Fig. A.8. Fig. A.9 shows the settings for the application of voltage load on the device. A bias of 1 V was applied such that 1 V is applied to the conductor\_0, which represents the proofmass and 0 V is applied to conductor\_1, which represents the cantilever beams.

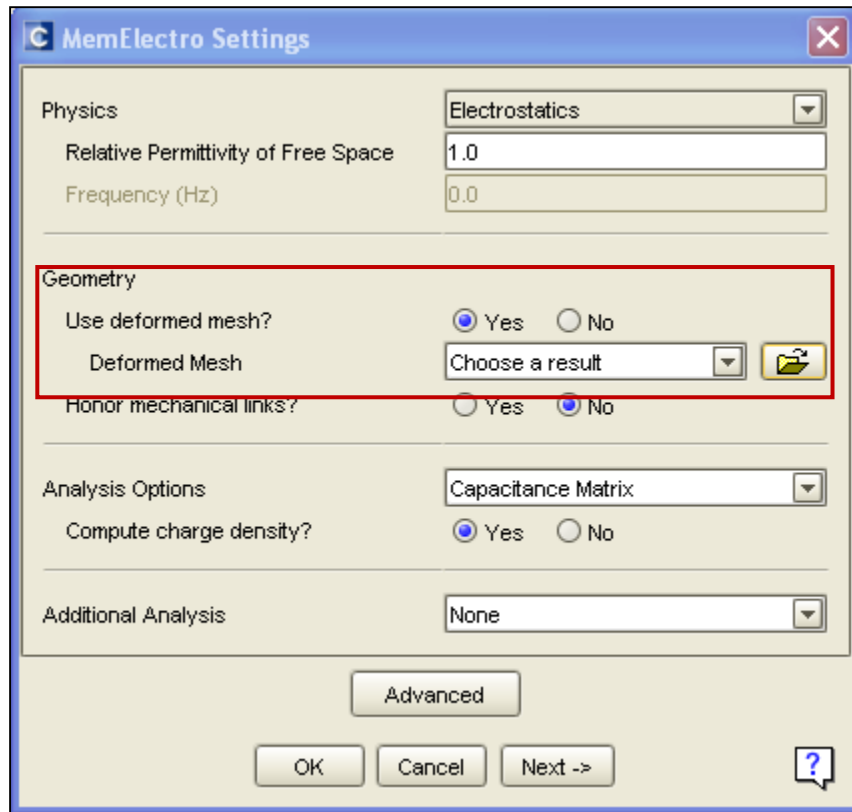


Fig. A.8. The settings for the MemElectroMM module. The deformed mesh, which is obtained from the MemMechMM, is specified in the Geometry tab, highlighted in the red rectangle.

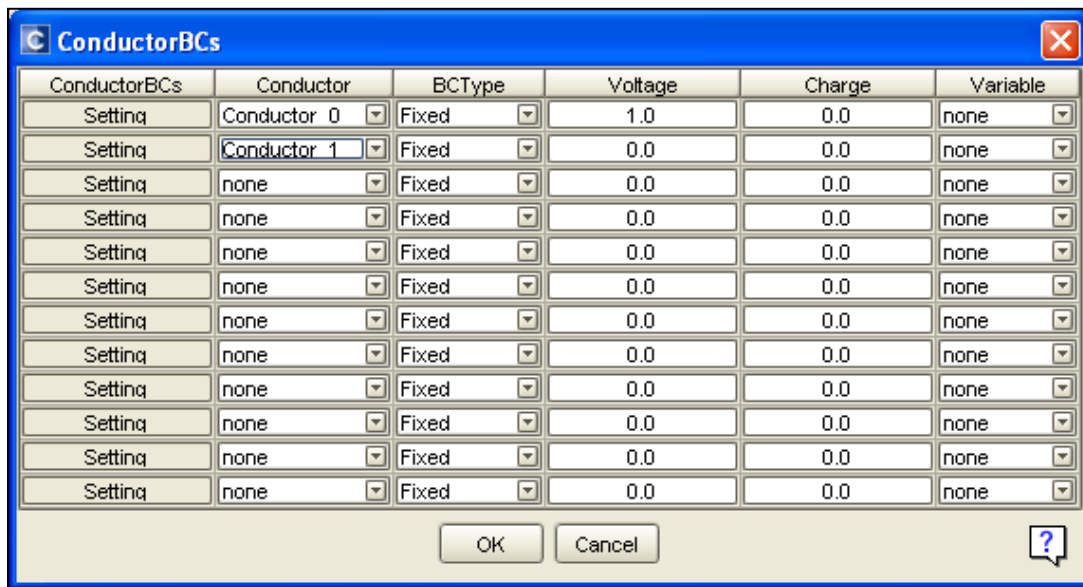


Fig. A.9. The settings for defining the voltage on the device.

In addition to the displacement and the capacitance analysis, a modal analysis was also performed to determine the resonant frequencies of the models. For performing the modal analysis, the MemMechMM was used. The settings of the analysis module were the same as those for the displacement analysis. However, a Modal analysis was specified in the tab of Additional analysis, as shown in Fig. A.10.

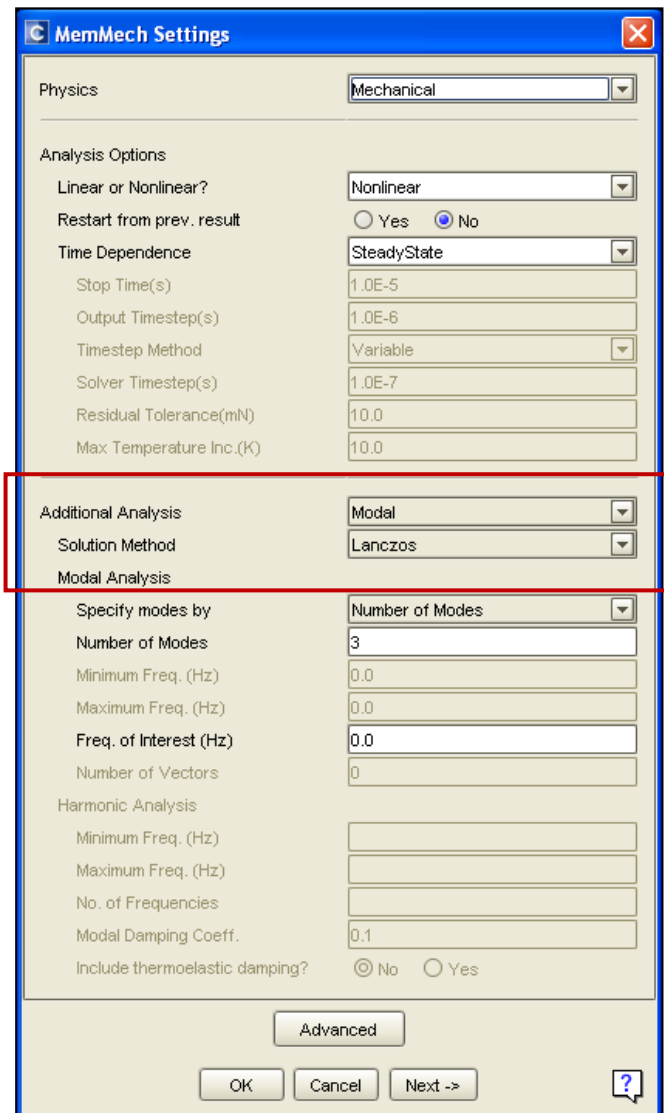


Fig. A.10. Settings of the MemMechMM for the Modal analysis, highlighted with red rectangle.

All the analyses discussed above were performed on each of the completed device models. However, a separate analysis was performed to determine the spring constant of the springs. The SpringMM module of CoventorWare™ was used for this analysis.

To perform the spring simulations, a 3D model of the springs was created. After meshing the 3D model, non-linear single ended type of mechanical spring was considered for the simulations and a full-factored analysis was performed. Fig. A.11 shows the initial analysis setting for SpringMM.

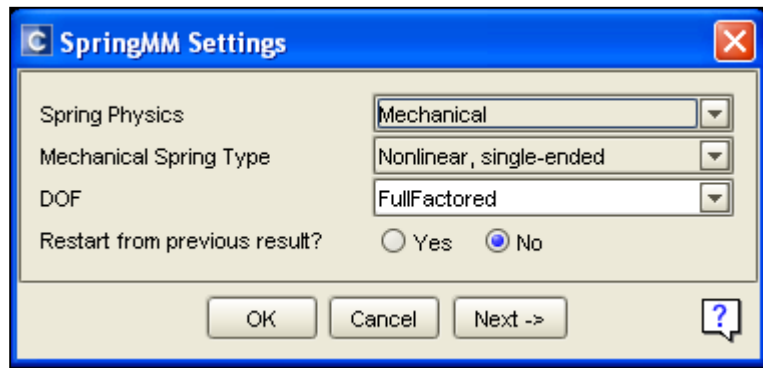
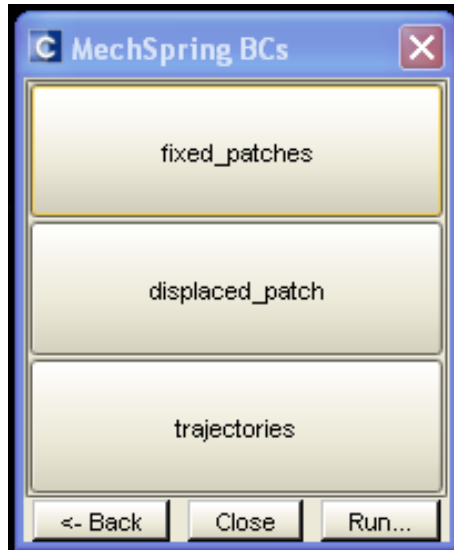


Fig. A.11. SpringMM settings for the analysis of spring constant

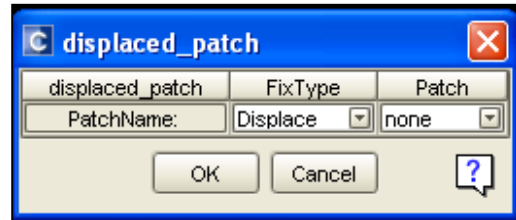
The loads and the boundary conditions are applied using the MEchSpringBCs tab of the SpringMM. While applying the boundary conditions, the anchors of the springs were fixed, while the free end was displaced between  $\pm 15\mu\text{m}$  in 5 steps, as shown in Fig. A.12.



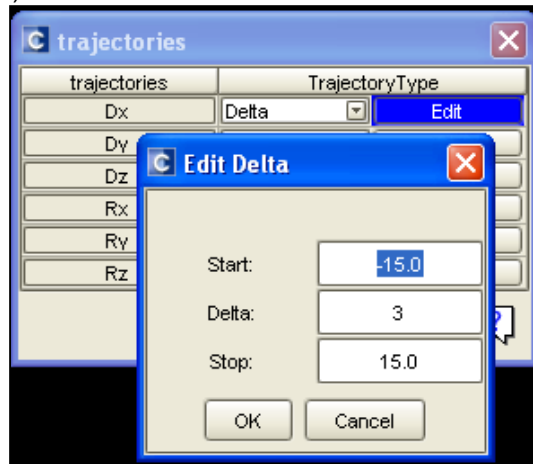
(a)



(b)



(c)



(d)

Fig. A.12. Setting for the SpringMM using MechSpringBCs (a) The MechSpringBCs tab used for defining the boundary conditions for SpringMM (b) fixed-patches tab for defining the fixed areas (c) displaced\_patch tab for defining the the displaced end of the spring (d) trajectories tab for defining the amount of displacement and the number of steps.

## REFERENCES

- [1] S. Beeby, M. Tudor, E. Koukharenko, N. White, T. O'donnell, C. Saha, S. Kulkarni, and S. Roy, "Micromachined silicon generator for harvesting power from vibrations," in *The 4th International Workshop on Micro and Nanotechnology for Power Generation and Energy Conversion Applications (PowerMEMS 2004)*, Kyoto, Japan, pp. 104-107, 2004.
- [2] M. El-Hami, P. Glynne-Jones, N. White, M. Hill, S. Beeby, E. James, A. Brown, and J. Ross, "Design and fabrication of a new vibration-based electromechanical power generator," *Sensors and Actuators A: Physical*, vol. 92, pp. 335-342, 2001.
- [3] Y. Jeon, R. Sood, J. Jeong, and S. Kim, "MEMS power generator with transverse mode thin film PZT," *Sensors and Actuators A: Physical*, vol. 122, pp. 16-22, 2005.
- [4] I. Gonenli, "Failure assessment in aerospace systems via integrated multi-functional sensors," The University of Texas at Arlington, 2011.
- [5] J. Paradiso and T. Starner, "Energy scavenging for mobile and wireless electronics," *Pervasive Computing, IEEE*, vol. 4, pp. 18-27, 2005.
- [6] E. Yeatman, "Advances in power sources for wireless sensor nodes," in *Proceedings of 1st International Workshop on Body Sensor Networks*, London, pp. 20–21, 2004.
- [7] S. Dayeh, D. Butler, and Z. Çelik-Butler, "Micromachined infrared bolometers on flexible polyimide substrates," *Sensors and Actuators A: Physical*, vol. 118, pp. 49-56, 2005.
- [8] J. Bisquert, D. Cahen, G. Hodes, S. Ruehle, and A. Zaban, "Physical chemical principles of photovoltaic conversion with nanoparticulate, mesoporous dye-sensitized solar cells," *J. Phys. Chem. B*, vol. 108, pp. 8106-8118, 2004.

- [9] A. Shah, P. Torres, R. Tscharnner, N. Wyrsh, and H. Keppner, "Photovoltaic technology: the case for thin-film solar cells," *Science*, vol. 285, pp. 692-698, 1999.
- [10] M. Strasser, R. Aigner, M. Franosch, and G. Wachutka, "Miniaturized thermoelectric generators based on poly-Si and poly-SiGe surface micromachining," *Sensors and Actuators A: Physical*, vol. 97, pp. 535-542, 2002.
- [11] M. Kishi, "Micro-Thermoelectric Modules and Their Application to Wrist-watches as an Energy Source, ," in *IEEE 18th Int. Conference on Thermoelectrics*, pp. 301-307, 1999.
- [12] Z. Peng-Xiang, L. Guo-Zhen, Z. Yan, W. Xiao-Ming, and H. Habermeier, "Room temperature light-thermo-detector made of high-Tc superconductor," *Acta Physica Sinica (Overseas Edition)*, vol. 7, pp. 810-816, 1998.
- [13] N. Hudak and G. Amatucci, "Small-scale energy harvesting through thermoelectric, vibration, and radiofrequency power conversion," *Journal of Applied Physics*, vol. 103, pp. 101301-1 - 101301-24, 2009.
- [14] P. Singh, S. Kaneria, V. Anugonda, H. Chen, X. Wang, D. Reisner, and R. Lafollette, "Prototype silicon micropower supply for sensors," *Sensors Journal, IEEE*, vol. 6, pp. 211-222, 2006.
- [15] J. Kiely, D. Morgan, D. Rowe, and J. Humphrey, "Low cost miniature thermoelectric generator," *Electronics Letters*, vol. 27, pp. 2332-2334, 2008.
- [16] M. Strasser, R. Aigner, C. Lauterbach, T. Sturm, M. Franosch, and G. Wachutka, "Micromachined CMOS thermoelectric generators as on-chip power supply," *Sensors and Actuators A: Physical*, vol. 114, pp. 362-370, 2004.
- [17] [Http://Www.Micropelt.Com/](http://www.Micropelt.Com/). (02/08/2011). *Micropelt*.
- [18] D. Rowe, D. Morgan, and J. Kiely, "Miniature low-power/high-voltage thermoelectric generator," *Electronics Letters*, vol. 25, pp. 166-168, 2008.
- [19] J. Hagerty, F. Helmbrecht, W. Mccalpin, R. Zane, and Z. Popovic, "Recycling ambient microwave energy with broad-band rectenna arrays," *Microwave Theory and Techniques, IEEE Transactions on*, vol. 52, pp. 1014-1024, 2004.



- [20] J. Hagerty, N. Lopez, B. Popovic, and Z. Popovic, "Broadband rectenna arrays for randomly polarized incident waves," in *Microwave Conference, 2000. 30th European Paris, France*, pp. 1-4, 2007.
- [21] S. Roundy, "On the effectiveness of vibration-based energy harvesting," *Journal of Intelligent Material Systems and Structures*, vol. 16, p. 809, 2005.
- [22] S. Roundy, P. Wright, and J. Rabaey, "A study of low level vibrations as a power source for wireless sensor nodes," *Computer Communications*, vol. 26, pp. 1131-1144, 2003.
- [23] H. Sodano, D. Inman, and G. Park, "A review of power harvesting from vibration using piezoelectric materials," *Shock and Vibration Digest*, vol. 36, pp. 197-206, 2004.
- [24] S. Beeby, M. Tudor, R. Torah, S. Roberts, T. O'donnell, and S. Roy, "Experimental comparison of macro and micro scale electromagnetic vibration powered generators," *Microsystem Technologies*, vol. 13, pp. 1647-1653, 2007.
- [25] S. Roundy, P. Wright, and K. Pister, "Micro-electrostatic vibration-to-electricity converters," in *Proceedings of IMECE'02 ASME International Mechanical Engineering Congress & Exposition*, Louisiana, p. 22, 2002.
- [26] P. Mitcheson, P. Miao, B. Stark, E. Yeatman, A. Holmes, and T. Green, "MEMS electrostatic micropower generator for low frequency operation," *Sensors and Actuators A: Physical*, vol. 115, pp. 523-529, 2004.
- [27] C. Williams and R. Yates, "Analysis of a micro-electric generator for microsystems," *Sensors and Actuators A: Physical*, vol. 52, pp. 8-11, 1996.
- [28] C. Williams, C. Shearwood, M. Harradine, P. Mellor, T. Birch, and R. Yates, "Development of an electromagnetic micro-generator," presented at the IEE Proceedings - Circuits, Devices and Systems, 2001.
- [29] R. Amirtharajah and A. Chandrakasan, "Self-powered signal processing using vibration-based power generation," *Solid-State Circuits, IEEE Journal of*, vol. 33, pp. 687-695, 2002.

- [30] T. Wacharasindhu and J. Kwon, "A micromachined energy harvester from a keyboard using combined electromagnetic and piezoelectric conversion," *Journal of Micromechanics and Microengineering*, vol. 18, pp. 104016-104024, 2008.
- [31] N. Shenck and J. Paradiso, "Energy scavenging with shoe-mounted piezoelectrics," *IEEE Micro*, vol. 21, pp. 30-42, 2001.
- [32] S. Beeby, M. Tudor, and N. White, "Energy harvesting vibration sources for microsystems applications," *Measurement science and technology*, vol. 17, pp. R175-R195, 2006.
- [33] H. Fang, J. Liu, Z. Xu, L. Dong, L. Wang, D. Chen, B. Cai, and Y. Liu, "Fabrication and performance of MEMS-based piezoelectric power generator for vibration energy harvesting," *Microelectronics Journal*, vol. 37, pp. 1280-1284, 2006.
- [34] M. Mahmoud, E. El-Saadany, and R. Mansour, "Planar electret based electrostatic micro-generator," *Proc. PowerMEMS (Berkeley, CA, 2006)*, pp. 223–226, 2006.
- [35] S. Roundy, P. Wright, and J. Rabaey, *Energy scavenging for wireless sensor networks: with special focus on vibrations*: Springer Netherlands, 1402076630 2004.
- [36] S. Cheng, N. Wang, and D. Arnold, "Modeling of magnetic vibrational energy harvesters using equivalent circuit representations," *Journal of Micromechanics and Microengineering*, vol. 17, p. 2328, 2007.
- [37] P. Mitcheson, T. Green, E. Yeatman, and A. Holmes, "Architectures for vibration-driven micropower generators," *Microelectromechanical Systems, Journal of*, vol. 13, pp. 429-440, 2004.
- [38] S. Meninger, J. Mur-Miranda, R. Amirtharajah, A. Chandrakasan, and J. Lang, "Vibration-to-electric energy conversion," *Very Large Scale Integration (VLSI) Systems, IEEE Transactions on*, vol. 9, pp. 64-76, 2002.
- [39] M. Bakri-Kassem and R. R. Mansour, "A high-tuning-range MEMS variable capacitor using carrier beams," *Electrical and Computer Engineering, Canadian Journal of*, vol. 31, pp. 89-95, 2006.

- [40] J. Smith and S. Smith, "Multi-Axis Vibration Mitigation Properties of Seat Cushions During Military Propeller Aircraft Operational Exposures," presented at the Proceedings of the Forty Third Annual SAFE Association Symposium Salt Lake City, Utah, 2005.
- [41] S. D. Smith, "Dynamic characteristics and human perception of vibration aboard a military propeller aircraft," *International Journal of Industrial Ergonomics*, vol. 38, pp. 868-879, 2008.
- [42] J. Luo, A. Flewitt, S. Spearing, N. Fleck, and W. Milne, "Young's modulus of electroplated Ni thin film for MEMS applications," *Materials Letters*, vol. 58, pp. 2306-2309, 2004.
- [43] J. W. Gardner, V. K. Varadan, and O. O. Awadelkarim, *Microsensors, MEMS, and smart devices*: John Wiley & Sons, ISBN-047186109X 2001,.
- [44] H. K. Chang and Y. K. Kim, "UV-LIGA process for high aspect ratio structure using stress barrier and C-shaped etch hole," *Sensors and Actuators A: Physical*, vol. 84, pp. 342-350, 2000.
- [45] H. Hübner, O. Ehrmann, M. Eigner, W. Gruber, A. Klumpp, R. Merkel, P. Ramm, M. Roth, J. Weber, and R. Wieland, "Face-to-face chip integration with full metal interface," in *Proceedings of Advanced Metallization Conference (AMC 02)*, *Material Research Society*, pp. 53-58, 2002.
- [46] P. Benkart, A. Kaiser, A. Munding, M. Bschorr, H. J. Pfeleiderer, E. Kohn, A. Heitmann, H. Huebner, and U. Ramacher, "3D chip stack technology using through-chip interconnects," *Design & Test of Computers, IEEE*, vol. 22, pp. 512-518, 2005.
- [47] A. Bogdanov and S. Peredkov, "Use of SU-8 photoresist for very high aspect ratio x-ray lithography," *Microelectronic Engineering*, vol. 53, pp. 493-496, 2000.
- [48] [Http://Www.Memscap.Com/En\\_Mumps.Html](http://www.memscap.com/en_mumps.html). (04/14/2011). MEMSCAP.
- [49] B. Coventorware, "2847, Coventor, Inc," ed, 2008.
- [50] S. Pamidighantam, R. Puers, K. Baert, and H. a. C. Tilmans, "Pull-in voltage analysis of electrostatically actuated beam structures with fixed–fixed and fixed–free end conditions," *Journal of Micromechanics and Microengineering*, vol. 12, p. 458, 2002.
- [51] F. Wall, M. Martinez, and J. Vandenvayle, "Corrosion behavior of a structural nickel electrodeposit," *Microsystem Technologies*, vol. 11, pp. 319-330, 2005.

- [52] T. Sterken, P. Fiorini, K. Baert, R. Puers, and G. Borghs, "An electret-based electrostatic -generator," in *12th International Conference on Transducers, Solid-State Sensors, Actuators and Microsystems*, Boston, pp. 1291-1294, 2003.
- [53] J. Boland, Y. H. Chao, Y. Suzuki, and Y. Tai, "Micro electret power generator," in *IEEE The Sixteenth Annual International Conference on Micro Electro Mechanical Systems MEMS-03* Kyoto, Japan, pp. 538-541, 2003.
- [54] F. Peano and T. Tambosso, "Design and optimization of a MEMS electret-based capacitive energy scavenger," *Microelectromechanical Systems, Journal of*, vol. 14, pp. 429-435, 2005.
- [55] H. Amjadi, "Charge storage in double layers of thermally grown silicon dioxide and APCVD silicon nitride," *Dielectrics and Electrical Insulation, IEEE Transactions on*, vol. 6, pp. 852-857, 2002.
- [56] T. Tsutsumino, Y. Suzuki, N. Kasagi, and Y. Sakane, "Seismic power generator using high-performance polymer electret," in *19th IEEE International Conference on Micro Electro Mechanical Systems MEMS 2006* Istanbul, Turkey, pp. 98-101, 2006.

## BIOGRAPHICAL INFORMATION

Madhumita Ambokar was born in Nagpur, India. She received her degree of Bachelor of Engineering from Yashwantrao Chavhan College of Engineering, Nagpur. She completed her M.S from University of Texas at Arlington in 2011.

Her focus of research is the design of MEMS based energy harvesters. She is interested in pursuing her work in the field of designing of MEMS sensors for mechanical as well as biological applications.